3-2024

Finite Element Analysis of Thermal-Mechanical Instabilities in Nonmetallic Friction Composite Material

Joseph-shaahu Shaahu

Finite Element Analysis of Thermal-Mechanical Instabilities in Nonmetallic Friction Composite Material

Abstract

Thermal-mechanical instability (TMI) has been a research topic of interest as it focuses a lot on transportation systems. Thermal-mechanical instability was first noticed in railway and experimentally studied with a pin-to-pin or pin-to-surface setup of sliding contact. The topic has been extended into brakes and clutches which are two of the most common sliding systems most susceptible to thermal buckling and thermoelastic instability (TEI), where thermal buckling and thermoelastic instability are two sub-categories of thermal-mechanical instability. Thermal-mechanical instability is an ongoing research to better understand the phenomenon and the limits at which such instability occurs. This work delved into the thermal-mechanical instability in automotive systems (brakes and clutches), studying the point of occurrence of this instability.

Coupling analysis such as vibration coupled with thermal buckling and thermal buckling coupled with thermoelastic instability was performed. The idea behind the coupling studies was to find out if the temperature gradient alone can induce instability in brakes or clutches, or the occurrence of one TMI can cancel out or induce the occurrence of another TMI to reduce or increase the chance of failure.

It was found that vibration during braking can induce uneven temperature gradient and internal stress in brakes to increase the chance of thermal buckling to occur but the increase in gradient temperature does not induce vibration. Also, thermal buckling modes tend to induce vibration in brakes. Thermal buckling and thermoelastic instability induce the occurrence of one another. In instances of TEI which creates hotspots due to uneven contact surface area during sliding, which increases the thermally induced stress in the brake or clutch to cause thermal buckling.

Alternate non-metallic friction material and the effect of anisotropy in friction materials was also investigated to determine the limits of brakes and clutches at which thermal-mechanical instability can occur. Carbon-carbon silicon carbide as a replacement for metallic friction material proved to minimize the occurrence of thermal-mechanical instability in brakes and clutches. The arrangement of reinforced fiber in the composite material also affects the limit of thermal buckling and thermoelastic instability. A composite with randomly distributed reinforced fiber evenly distributes the internal stress better than uniformly aligned reinforced fibers and hence the randomly distributed composite used in brake and clutch production significantly increases the point of thermal buckling or thermoelastic instability to occur. The ideal composition for a carbon-carbon silicon carbide composite material with fiber aspect ratio of 1 to produce a clutch to withstand high temperatures without TMI occurring is 35% carbon fiber volume and 20% silicon carbide volume.

Document Type

Dissertation

Degree Name

Ph.D.

First Advisor

Yun-Bo Yi

Keywords

Thermal-mechanical instability (TMI), Sliding systems, Brakes, Friction

Finite Element Analysis of Thermal-mechanical Instabilities in Nonmetallic Friction Composite Material

A Dissertation

Presented to

the Faculty of the Daniel Felix Ritchie School of Engineering and Computer Science

University of Denver

In Partial Fulfillment

of the Requirements for the Degree

Doctor of Philosophy

by

Joseph-shaahu Shaahu

March 2024

Advisor: Dr. Yun-Bo Yi

Author: Joseph-shaahu Shaahu
Title: Finite Element Analysis of Thermal-mechanical Instabilities in Nonmetallic Friction Composite Material
Advisor: Dr. Yun-Bo Yi
Degree Date: March 2024

ABSTRACT

Thermal-mechanical instability (TMI) has been a research topic of interest as it focuses a lot on transportation systems. Thermal-mechanical instability was first noticed in railway and experimentally studied with a pin-to-pin or pin-to-surface setup of sliding contact. The topic has been extended into brakes and clutches which are two of the most common sliding systems most susceptible to thermal buckling and thermoelastic instability (TEI), where thermal buckling and thermoelastic instability are two sub-categories of thermal-mechanical instability. Thermal-mechanical instability is an ongoing research to better understand the phenomenon and the limits at which such instability occurs. This work delved into the thermal-mechanical instability in automotive systems (brakes and clutches), studying the point of occurrence of this instability.

Coupling analysis such as vibration coupled with thermal buckling and thermal buckling coupled with thermoelastic instability was performed. The idea behind the coupling studies was to find out if the temperature gradient alone can induce instability in brakes or clutches, or the occurrence of one TMI can cancel out or induce the occurrence of another TMI to reduce or increase the chance of failure.

It was found that vibration during braking can induce uneven temperature gradient and internal stress in brakes to increase the chance of thermal buckling to occur but the increase in gradient temperature does not induce vibration. Also, thermal buckling modes tend to induce vibration in brakes. Thermal buckling and thermoelastic instability induce the occurrence of one another. In instances of TEI which creates hotspots due to uneven contact surface area during sliding, which increases the thermally induced stress in the brake or clutch to cause thermal buckling.

Alternate non-metallic friction material and the effect of anisotropy in friction materials was also investigated to determine the limits of brakes and clutches at which thermal-mechanical instability can occur. Carbon-carbon silicon carbide as a replacement for metallic friction material proved to minimize the occurrence of thermal-mechanical instability in brakes and clutches. The arrangement of reinforced fiber in the composite material also affects the limit of thermal buckling and thermoelastic instability. A composite with randomly distributed reinforced fiber evenly distributes the internal stress better than uniformly aligned reinforced fibers and hence the randomly distributed composite used in brake and clutch production significantly increases the point of thermal buckling or thermoelastic instability to occur. The ideal composition for a carbon-carbon silicon carbide composite material with fiber aspect ratio of 1 to produce a clutch to withstand high temperatures without TMI occurring is 35% carbon fiber volume and 20% silicon carbide volume.

ACKNOWLEDGMENTS

I would like to express my gratitude to all who assisted, guided, encouraged, and supported me throughout the process of my Philosophy of Doctorate degree. First, I would like to thank God for leading and seeing me through this path.

Second, I would like to thank my advisor Dr. Yun-Bo Yi, for his guidance, support, challenge, and faith in me, which motivated me to being the best version of myself as a PhD student and without his help this dissertation would not have been possible.

Third, I would like to thank my friends and colleagues (Kingsford Koranteng, Dr. Jide Williams, Chatura Semasinghe, Yizhan Zhang, and Sumaiya Sultana Tanu) who supported me emotionally, and whose presence and individual drive sparked friendly competition and motivated me to do better.

Last, I would like to thank my family for their unwavering love, support, and encouragement throughout my entire educational journey. Their encouragement has been a driving force for me, and I am grateful to them.

Thanks to all who made this journey worthwhile.

TABLE OF CONTENTS

LIST OF TABLES

LIST OF FIGURES

CHAPTER I

INTRODUCTION

1.1 OVERVIEW

Contact systems are widely seen and used in the world. Contact can be used as a transfer mechanism, can be used to transfer power, motion, or energy in the form of heat. Such examples of contact are gears to transfer motion, clutches to transfer power, and brakes to change kinetic energy to heat while slowing a moving body. The biggest phenomenon in contact is friction. Friction helps keep bodies in contact. In some cases, friction can be useful and in other instances friction should be minimized for stability in contacting bodies. One of the widely known contact sliding mechanisms is the brake. Simply described, a brake consists of a stationary body and a rotating body. Brakes are used in different areas in the field of engineering. It's one use is to slow or stop a moving body, during which the motion of the car is converted to thermal energy during braking, where the heat generated is known as frictional heat. Brakes can be seen in industrial settings in machinery such as horizontal lathes and mostly seen as well in the transportation industries such as automobiles, airplanes, and trains. Although technologies have improved since the first use of brakes in a system, the idea, and physics behind it never changes and it stays the same across different uses. In most circles of car or motorcycle enthusiasts the brake is the most important safety feature of a car or motorcycle. That is the reason that any person teaching how to drive a car or ride a motorcycle tends to start with knowledge on what a brake is and how to use it effectively. There are two different types of brakes, the drum brake (Figure 1.1) and disc brake (Figure 1.2). The drum brake has the stationary body (shoes) housed in the rotating body (the drum). When the brakes are engaged, the brake shoes are pushed outward onto the inner wall of the drum, to slow the wheel's rotational speed.

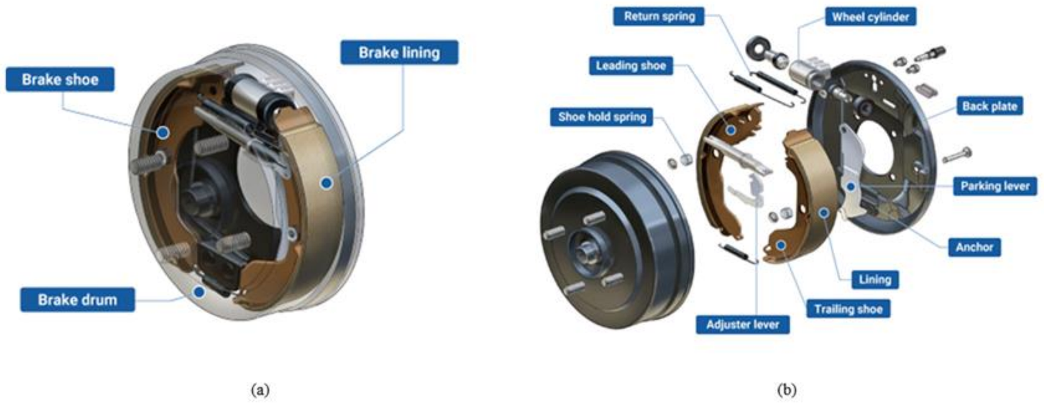

Figure 1.1: Automotive drum brake a) section cut-out view; b) exploded view. [1]

The idea stems from Newton's first law of motion which states that "a body in any state tends to remain in that state unless acted upon by an external force". The state of the body is rotational motion and the external force in this case is friction slowing the body down to a stop. In the case of a disc brake, the rotating body is the rotor, and the stationary body is the pad which are housed in the calipers. The rotor has a disc-like shape hence the name disc brake, just like the drum brake has a rotating "drum" hence the name. The disc brake was developed after the drum brake and in most cases to replace the drum brake, that is because of the major drawback of a drum brake which is poor ventilation and heat dissipation which makes it prone to high temperatures which affects the performance.

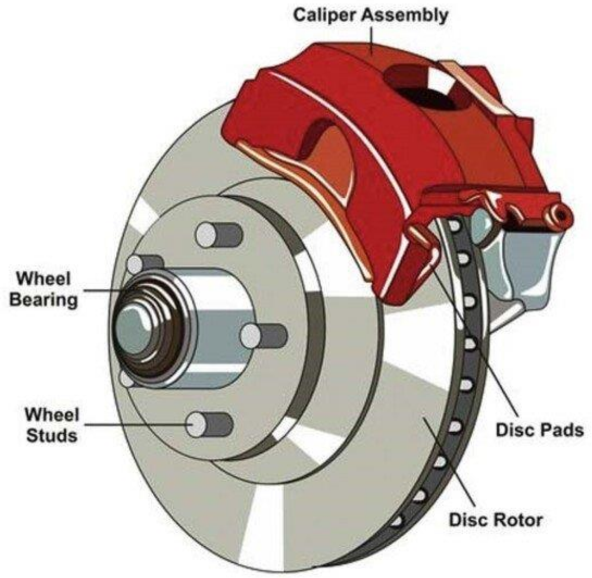

Figure 1.2: Common automotive disc brake [2]

The other instance of a contact system is the clutch system, example shown in Figure 1.3. The clutch is used to transfer power and motion between bodies in other words transmits power, hence the presence of clutches in a transmission. Sliding in brake is necessary and essential, but in a clutch system sliding is not ideal, but nonetheless is present. Sliding in a clutch happens at the instance the clutch disc contacts the engine's flywheel. The severity of sliding which occurs between the clutch plate and engine flywheel is different depending on whether it is an automatic or standard (manual) transmission, this is due to the method of clutch engagement. As the names suggest, automatic engages and disengages the clutch without human input using electrically controlled computer units and manual utilizes human intervention. Sliding is more noticeable in the manual transmission because human factor affects reaction time. The clutch when engaged connects the clutch plate to and matches the speed of the engine's flywheel and in-turn transfers power to the tires via the axel of a car, and when disengaged disconnects the contact between the plate and flywheel and cuts power to the tires. Figure 1.3 shows an example of two of the common types of clutches used in cars. The single disc clutch and the multi-disc clutch. The multi-disc clutch is also classified as a dry or wet clutch, the difference being the presence of lubricating oil. Wet clutch has lubricants helping in cooling and dry clutch does not have lubricating.

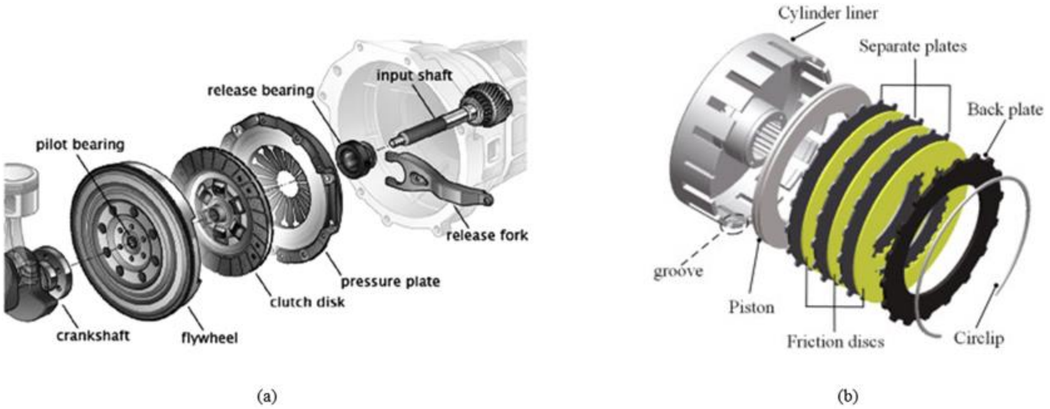

Figure 1.3: Automotive clutch schematic a) single disc clutch [3]; b) multi-disc clutch [4]

Friction is useful in motion control of a body, but the rise in temperature as a result can have adverse effects. Such adverse effects include thermal-mechanical instabilities (TMI). There is no straight forward definition of thermal-mechanical instability, but it can be inferred from the definition of mechanical instability. Mechanical instability in a system is the increase in internal stress of a body with no bounds. Therefore, thermal-mechanical instability is the system experiencing mechanical instability due to thermal conditions such as thermal loads. Some examples of thermal-mechanical instability are mostly dynamic instabilities influenced by thermal loads such as thermal buckling, thermoelastic instability, vibration, thermal shock, creep, and thermal fatigue. It should be noted that all the listed examples of thermal-mechanical instability can be experienced in friction systems such as automotive brakes and clutches, but the scope of this dissertation focuses mainly on thermal buckling and thermoelastic instability (TEI).

1.2 THERMAL-MECHANICAL OVERVIEW

Thermal buckling is an example of thermal-mechanical instability. It is a phenomenon that can occur when a body is exposed to high temperatures. When a slender beam is subjected to thermal loading, thermal stresses are developed through the beam structure. When the stresses are compressive, the structure may undergo instability. This type of instability, since it is caused by temperature loading, is known as thermal buckling or thermal instability. At the temperature which buckling occurs, the structure starts to alter the displacement direction, that is, shortening changes to lateral displacement. Therefore, this temperature is also known as the thermal bifurcation point [5]. Thermal bifurcation point is interchangeable with critical buckling temperature. Thermal buckling is also a common failure mode of brakes and clutches in automotive systems. In an emergency braking study, the stress responses of the disc due to the combined thermal and mechanical loadings were separated into thermal stress and mechanical stress, and their particular characteristics to the individual thermal or mechanical loading were identified. That is: the amplitude of the total stress in the disc was predominately determined by the thermal loading; however the high cycle fluctuations were mainly due to the mechanical loading [6].

1.2.1 THERMAL-MECHANICAL INSTABILITY METHODS

There are various methods of solving a thermal buckling problem such as analytical methods and numerical method. Analytical methods include Euler's buckling formular for columns, Johnson's parabolic function [5] and plate theories such as von Karman plate equations, Timoshenko beam theory, and Reissner-Mindlin plate theory [5,7]

1.2.1.1 ANALYTICAL METHOD

One of the most common methods in calculating the critical buckling load is Euler's method with a slender beam with pinned ends. The general equation shown below is the general Euler's equation for critical buckling load.

$$P_{cr} = \frac{\pi^2 EI}{L^2} \tag{1.1}$$

Where P_{cr} is the critical buckling load, E is the elastic modulus, L is the length of the beam, and I is the area moment of inertia. The equation can be re-written to find critical buckling temperature (equation 1.2) with the presence of non-uniform temperature.

$$\Delta T = \frac{\pi^2 I}{A^2 \alpha L^2} \tag{1.2}$$

Where ΔT, A, and α represents the change in temperature, area, and coefficient of thermal expansion. In the case of a full brake disc or clutch disc, equation 1.2 will not work, but, for a simplified axisymmetric 2D model of a disc the analytical equation will be similar to equation 1.2 but with different boundary conditions.

1.2.1.2 NUMERICAL METHOD

Numerical methods for solving thermal-mechanical problems includes;

- Finite element method: This method works by discretization of the model into smaller pieces and solved. This is then integrated into the overall model.
- Shooting method: The shooting method is a numerical technique used to solve boundary value problems (BVPs) for ordinary differential equations (ODEs). It works by transforming a BVP into an initial value problem (IVP). This method is called “shooting” because it’s similar to firing a projectile and adjusting your aim based on where it lands, until you hit your target. In this case, the “target” is the correct solution to the BVP. It’s important to note that while the shooting method can be quite effective, it’s not guaranteed to work for all BVPs, especially those with complex or non-linear behavior [5].
- Linear eigenvalue analysis: This method assumes that the structure behaves linearly and elastically under small deformations. It solves for the critical buckling load and the corresponding buckling mode by finding the eigenvalues and eigenvectors of a linearized equilibrium equation. This method is fast and simple, but it may not capture the nonlinear effects and post-buckling behavior of the structure [8].
- Nonlinear buckling analysis: This method accounts for the nonlinear effects and large deformations of the structure under thermal loads. It solves for the equilibrium path and the bifurcation point of the structure by using an iterative procedure, such as the Newton-Raphson method or the arc-length method. This

method is more accurate and realistic, but it may require more computational resources and convergence criteria [8].

- Transient analysis: This method considers the dynamic response and time-dependent behavior of the structure under thermal loads. It solves for the displacement, velocity, and acceleration of the structure by using a time integration scheme, such as the explicit or implicit method. This method is useful for studying the transient phenomena and damping effects of the structure, but it may involve more complex formulations and boundary conditions [8].
- Fourier Analysis: Fourier analysis is a mathematical technique used to decompose functions into their constituent frequencies. Named after Joseph Fourier, this method represents a function as a sum of simpler trigonometric functions.

Fourier analysis is another numerical method for solving thermal-mechanical instability problems. A reduced Fourier method was proposed by Chen Z. et. al., [9] for solving thermal buckling problems for annular rings representing brakes and clutches. The geometric nonlinearity in Green's strain theory with a predefined circumferential wave number was utilized in deriving the stiffness matrix. The method proved to be sufficient in predicting thermal buckling as well as reduction in computational time. Thermal buckling problems researched using numerical methods have assumed various thermal distribution imposed on the brake rotor or friction disc, but a research conducted by Ali Belhocine and Mostefa Bouchetara [10] which was a thermomechanical coupling on a brake rotor, using heat transfer simulation in ANSYS for heat generation during braking and the mechanical effect, where they found the Von Mises stress and the total deformations of the disc and contact pressures of the brake pads increase in a notable way when the thermal and mechanical aspects are coupled. Koranteng et. al., [11] also performed experiments on brakes of an in-wheel driven motor with varying pad geometry and location, the temperature recorded during the experiment was imposed on a FEA model to study thermal buckling and it was found that the geometry of brake pad does positively affect the temperature distribution and can lead to thermal buckling at certain braking pressure and duration of braking. Although the location and mounting of brakes and clutches are mostly universal it was shown by simulation data verified by experiment [12] that the boundary condition have effects on the thermal buckling temperature [13,14]. Figure 1.4 shows an image of a warped brake rotor [15] and clutch disc [7] due to thermal buckling.

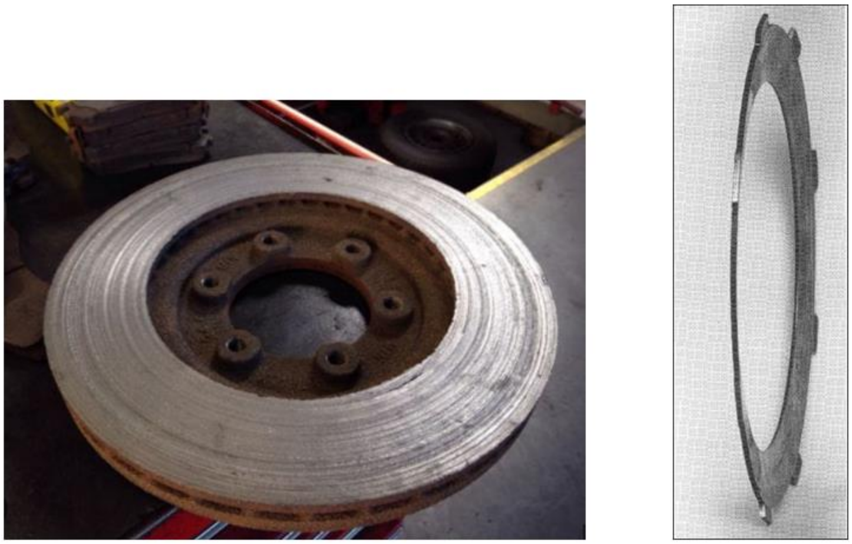

(a) (b)

Figure 1.4: Warped a) brake rotor; b) clutch disc due to thermal buckling

Thermal buckling is influenced by the temperature distribution, material property, and geometry. The increase in the temperature gradient and the thermal stresses generated by the radial temperature gradient begin to influence the buckling deformation of the friction components [11,12]. If the friction components are thinner than the critical thickness h_{cr}, the circumferential thermal stresses play a leading role in the buckling deformation [12]. Otherwise, the buckling deformation caused by the radial thermal stress will play a leading role [12–14,16]. Thermal buckling of the pressure plate is easier to occur in its cooling stage than in the heating stage. Since the critical buckling temperature far exceeds the actual possible temperature, the concave deformation of pressure plate [14] and brake rotor [16] is not induced by the thermal buckling mechanism. Hu Ling et. al., [17] explored the generation mechanism of disc buckling by studying the influence of initial topography on thermoelastic behavior of a simplified brake disc under independent thermal load experimentally and computationally. Furthermore, Cenbo X. et. al., [18] studied transient temperature field in finite thickness plate under symmetrically located moving heat sources to conclude that temperature field is sensitive to the thickness. There exists an instance after the initiation of buckling where a deformation occurs, this is post-buckling. Buckling and post-buckling analyses are concerned with the derivation of buckled solutions to plate theories in the neighborhood of a bifurcation point, using expansion methods [19]. Post-buckling can help better understand the thermal buckling phenomenon, hence Chen Z. et. al., [20] using finite element method to predict thermally induced post-buckling of clutch discs. Using displaced element from the thermal buckling result as the initial condition for the thermal buckling analysis for post-buckling.

Thermoelastic instability (TEI) is another sub-category of thermal-mechanical instability. It is a failure common in both clutch and brake systems. It was first proposed, researched, and defined by Barber [21] as the inevitable irregularities in surfaces of two sliding solids in nominal contact will cause non-uniformity in the pressure distribution and frictional heat which lends to distortion of the solid from thermal expansion. Due to the non-uniformity the distortion is also known as hotspots. Figure 1.5 shows the presence of hotspot on a brake rotor and clutch disc [22]. Such hotspots are due to thermoelastic instability caused by uneven heat distribution.

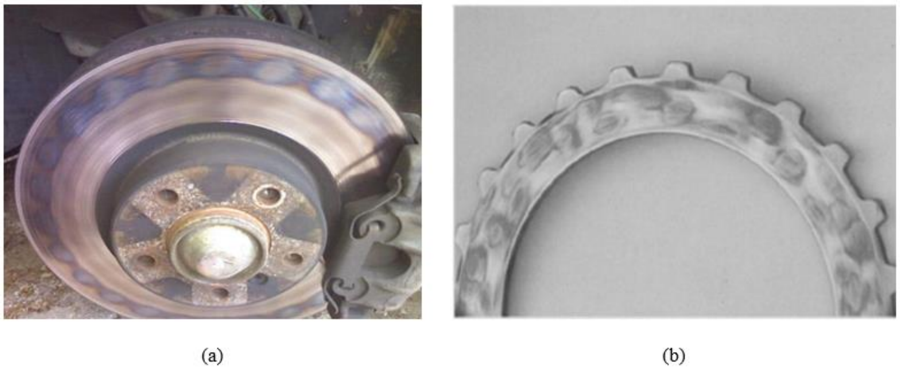

Figure 1.5: Hotspot presence due to TEI a) brake rotor; b) clutch disc

Barber [21] also stipulated a possible solution to TEI, stating the stability of the system depends on the relationship between the wear rate and thermal expansion. If the effect of wear is greater than the effect of thermal expansion, there is a chance of stability in the system and if the effect of thermal expansion is greater than the effect of wear, there is a chance of instability to occur in the system. Dow and Burton [23] supported the idea of wear having an effect on the thermal instability process, and that it does indeed serve to dampen the growth of a perturbation. However, wear is proportional to the integral of pressure over a time interval and when the wear rate is small- or the-time interval of interest is short, wear can be neglected. In lubricated contact, in particular, its role is of secondary importance. Dow and Burton [23] proposed the perturbation method using the growth rate of the perturb boundary condition to determine at what limit the system becomes unstable. Using the perturbation method developed by Dow and Burton, Barber [24] proposed on the critical sliding speed. There exists a speed above which the system becomes unstable, this speed is known as the critical sliding speed. Yi et. al., [22] expanded on the perturbation method to solve the eigenvalue problem of TEI using a reduced Fourier analysis. Jiayin and Barber [25] proposed an alternative implementation of the transient problem, based on the expression of the temperature and stress fields as modal expansions. Yi [26] implemented the proposed half plane perturbation method by Burton into thermoelastic instability in brakes and clutches in conjunction with finite element method to solve an eigenvalue equation, from which the critical value of the operating speed is determined from the stability boundaries of the leading mode.

1.3 FRICTION MATERIAL OVERVIEW

There are certain requirements for the type of materials used in any frictional system. During the first introduction of brakes, the friction material used in brake pads was asbestos. Asbestos is the name given to a group of naturally occurring minerals that are resistant to heat and corrosion. Asbestos has been used in products, such as insulation for pipes (steam lines for example), floor tiles, building materials, and in vehicle brakes and clutches [27,28]. Its characteristics of being resistant to heat was one of its benefits as a material of choice in brake pads and clutch friction disc. Asbestos was widely used and dominated as the friction material of choice up until the late 1980s where the federal government took steps to protect citizens from exposure to asbestos. First, on July 12, 1989, the United States Environmental Protection Agency (EPA) established a ban on new uses of asbestos. This ban caused a change in brake and clutch friction material to mostly contain metals (such as copper). Such metals were chosen due to their high conductivities and modulus. While materials such as carbon-fiber reinforced carbon composites (C/C) were being utilized as state of the art in aircraft brake systems and in formula one race cars [29]. Copper based friction material was used in tribological experiment conducted Zhao E. et. al., [30] and Koranteng K. et al., [31] research of the tribological characteristics of copper in multi-disc wet clutch and single disc dry clutch respectively. Copper friction material in multi-disc wet clutch results in surface temperature increase as the contact ratio reduces and friction coefficient increases dramatically, so that local friction torque and total output torque grow significantly. In addition, the vibration of the output torque becomes more severe as the contact ratio reduces [30]. Other works into other metallic based friction material was published with their findings on the effect of such materials in braking mostly. Mustafa Boz and Adem Kurt [32] studied the effect of aluminum oxide (Al_2O_3) added to bronze-based powders, creating an aluminum reinforced bronze-based brake linings, and researched the effect on a brakes friction performance. In which they concluded that an increase in Al_2O_3 content resulted in adhesive wear, and a reduction in mass loss. Also, the samples reinforced with 2% and 4% Al_2O_3 exhibited the best results. Composite material with high volume reinforcement tends to reduce wear in braking conditions. For instance, as seen in the published works of Prabhu, T. et. al., [33,34] where they studied the effect of reinforcement type, size, and volume fraction on the tribological behavior of dry sliding wear of metallic composite at high sliding speed conditions, where they found that the wear loss decreased with increasing volume fraction of silicon carbide (SiC) for all particulate sizes. At low sliding speeds the composites with large particle sizes and high volume fractions were more effective in controlling wear, and on the other hand, at higher sliding speeds the high volume fraction composites were found to be more effective in controlling wear for all particle sizes.

Over the years lightweight materials have been more attractive in manufacturing and in industries, especially in the automotive industry where weight reduction is prevalent to achieving higher speeds and superior handling. Alternative lighter materials have been researched to reduce overall weight, and the brake system among other aspects have seen such weight reduction, so replacing friction materials with lighter (low density) materials such as C/C composite. The fiber reinforcement in C/C composite enables a suitable damage tolerance and favorable mechanical strengths. Low densities (<2 g/cm3) make them very suitable for light weight applications [29,35,36]. Although copper is used in friction materials, the wear rate of such metallic based friction material is high. The level of particle emissions from copper metal matrix composites (Cu-MMCs) increased substantially with increasing sliding speed [37]. Brake emissions are strongly affected by disc hardness and the iron transferred to the pad surface. The transferred iron increased brake emissions due to the reduced cohesive strength of the plateaus on the pad surface. The grey iron microstructure also affected the ultrafine particle concentration owing to the graphite flakes [38].

Metallic materials used in friction materials to increase coefficient of friction in brakes pose environmental threats when such particles are released to the environment due to wear of the friction materials. These particles tend to contaminate the environmental ecology system and as such alternative metallic free friction materials are required and needed to prevent environmental pollution. An initiative to combat the environmental risk of such particles was proposed as the Copper-Free Brake Initiative, which is a voluntary initiative that was signed by the US Environmental Protection Agency (EPA) [39] and the automotive industry on January 21, 2015. The initiative aims to reduce the use of copper and other materials in motor vehicle brake pads. The agreement calls for reducing copper in brake pads to less than 5 percent by weight in 2021 and 0.5 percent by 2025. In addition to copper, this voluntary initiative reduces mercury, lead, cadmium, asbestiform fibers, and chromium-six salts in motor vehicle brake pads. The initiative will decrease runoff of these materials from roads into the nation’s streams, rivers, and lakes. Copper from stormwater runoff can affect fish, amphibians, invertebrates, and plants [40,41].

This need for non-metallic friction material led researchers to research alternative eco-friendly friction materials that can replace the traditional materials such as asbestos, metal, and mineral fibers. Some of these alternatives are natural fibers, such as banana peels, palm kernels, palm slag, hazelnut shell, and crab shell [42] . The major advantage of such eco-friendly natural fibers in friction materials over copper and asbestos is the absence of harmful impact to the environment, but also what makes them a suitable candidate is their mechanical and tribological characteristics, such as high strength, elasticity, friction, and wear resistance [43–45]. Natural fibers in brake pads display good tribological characteristics, but results in a shorter lifecycle compared to metallic based pads due to its high moisture absorption, poor resistance to moisture, susceptibility to damage from pests, mold, mildew, and shrink and wrinkle [44–47].

Also, Seo H. et. al., [38] discovered from their experimental study of the effect of disc materials on brake emission during moderate-temperature braking, that ceramic disc exhibited significantly lower brake emissions due to high wear resistance and no iron transfer to the pad surface compared to grey cast iron. Among other studies on composite materials in sliding experiments, the consensus of an ideal replacement for the common friction material in use in brakes and clutches is a non-oxide CMCs (ceramic matrix composite) based on carbon/carbon composites which were first introduced and developed in the 1970s as lightweight structures for aerospace applications. They were initially used in applications of high temperature such as rocket nozzles and brake discs of aircraft etc. Although, good tribological and overall properties of C/C being superior to common friction materials, it is not a material with long lifetime because of its insufficient oxidation resistance, the low COFs in humid conditions and at temperatures below 200 °C [29]. With C/C lacking in lifetime, the addition of ceramic compound remedies this, by further eliminating noise, improving the wear resistance, improving heat dissipation capabilities, and reducing thermal wear and tear [48]. Their lifetime under highest thermomechanical requirements surpassed its metallic counterparts. Therefore, instead of using carbon as the matrix in these composites an improvement to use ceramic was exhaustively researched due to its high oxidation resistance, high creep resistance and superior temperature and thermal shock ability. In addition, using CMC based friction material ensured no potential health hazard like with the use of asbestos and no environmental hazard like with the use of copper and other heavy metals. Although, a replacement for heavy metal friction material is CMC friction material, it is relatively expensive compared to copper-based friction materials.

In general, the reinforcement in such composite affects its material microstructure making it either homogenous or heterogenous. The nature (hetero-/homo-genous) is determined by the reinforcement arrangement, in rare cases are the reinforcement aligned in a specific direction unless using pre-pregnated sheets and layered in a particular orientation, therefore, most commonly are they randomly oriented and makes the composite homogenous, but when the reinforcements are all aligned in a single direction, or the mixture is compacted, the material displays anisotropy (transverse isotropy or orthotropy). During the study of the effect of composite material properties on thermal-mechanical instability, the dissertation focused on transverse isotropy and orthotropy material properties and ceramic matrix composite carbon-carbon silicon carbide composite material (C-C/SiC).

1.4 OVERVIEW OF DISSERTATION

Chapter II

The coupled and uncoupled problems of thermal buckling and vibration are analyzed using an ABAQUS benchmark vented brake model. It is known that different assumptions of temperature, either in the radial or axial direction, may lead to different solutions of thermal buckling. In this study, we assumed some representative temperature profiles in the radial direction, including linear, sinusoidal, and exponential functions, meanwhile, the circumferential distribution of temperature was maintained uniform. The effect of structural vibration on the thermal buckling modes, as well as the effect of buckling modes on vibration in this simplified situation, were both analyzed. Although it is concluded that vibration during braking does not significantly increase the chance of buckling for the ABAQUS benchmark model, the results are highly dependent on the chosen parameters including materials, dimensions, and rotational velocity, and the coupling can be strong in some conditions.

Chapter III

In this study the distributions of temperature variations were obtained from the eigenmodes based on the classical TEI analyses. The critical buckling temperatures and the associated deformation modes were subsequently computed using the commercial software ABAQUS. The effects of sliding speed, coefficient of friction and boundary conditions have been investigated for both banding and focal modes. It is concluded that the TEI induced temperature variations can significantly alter the distribution of thermal stresses, and that there could exist a strong coupling between TEI and thermal buckling under some conditions. Although the analyses were performed in the settings of clutch applications, the conclusions are applicable to brake discs as well because of the shared similarities.

Chapter IV

Computational and numerical methods were utilized in the study of thermal-mechanical instabilities and how it is affected by anisotropic parameters of a nonmetallic friction material. The material properties for the friction material used in this paper are experimental and calculated values obtained from literature for a unidirectional C-C/SiC composite. Anisotropic parametric studies were performed to investigate the effect of the anisotropic parameters on thermal-mechanical instabilities and to determine which parameter is more dominant. The axis definition was converted from cartesian to polar, to accurately represent a brake rotor or clutch disc. It was found that an increase in the radial, circumferential modulus of elasticity or coefficient of thermal expansion decreases the buckling temperature which increases the chance of thermal buckling to occur. It was revealed that a decrease of the axial elastic modulus or an increase of the radial thermal conductivity greatly reduces thermoelastic instability (TEI) onset. Further, an increase of out-of-plane Poisson's ratio (ν_{23}) produced a higher chance of the occurrence of TEI in a clutch disc. It was also revealed that thermal conductivity has no effect on thermal buckling and coefficient of thermal expansion has very little effect of TEI. It was concluded that a uniform temperature distribution along the thickness of a disc negates the effect of coefficient of thermal expansion on thermal buckling.

Chapter V

A method was developed and used in conjunction with a finite element method (FEM) Micromechanics. The method coined packing is a compression of randomly distributed inclusion composite mixture in a single direction. The method developed uses an algorithm to generate non intersecting inclusions in a unit cell and compresses the unit cell to introduce internal stresses and requires little strain to fracture during the FEM simulation. The FE method is the chosen micromechanics method in calculating the material properties of the composite. The corresponding material properties are used to calculate the thermomechanical instabilities in a clutch disc. The increase in carbon fiber increases the buckling temperature and the increase in silicon carbide decreases the buckling temperature. The increase in carbon fiber decreases the coefficient of thermal expansion of the composite but increases with an increase in silicon carbide. The proposed method in conjunction with a random search method was used to predict the ideal carbon fiber volume and silicon carbide volume of the carbon-carbon silicon carbide (C-C/SiC) composite mixture that maximizes both the critical buckling temperature and critical sliding speed of a clutch disc. Although, the method used in calculating the composite material properties is focused on 2D and generalized, it should be noted that the method can be extended to three dimensions (3D).

CHAPTER II

A COUPLING ANALYSIS OF THERMAL BUCKLING AND VIBRATION IN DISC BRAKES

2.1 INTRODUCTION

Vibrations have been used to study and quantitate the equilibrium state of a system. Such simplified systems are often represented with a mass and spring system. Although it would be reasonable to assume a vibrating system is out of balance, the amplitude of a frequency determines the severity of a fault [49]. In reality, vibrating systems or bodies are not necessarily out of balance. All bodies vibrate at a certain frequency; this frequency is known as the natural frequency of the body. Various studies of vibration have been conducted throughout the years in various areas, such as human anatomy, civil and structural engineering, mechanics, automotive industry, etc. Many vibration studies conducted for the automotive industry have been on the brake disc and these have mainly been squeal analysis and brake judder analysis. Brake judder is a braking induced forced vibration occurring in different types of vehicles. Brake judder is usually felt in the steering wheel, which affects the operation of the vehicle and can cause veering. Hence, the study of such has been prudent to reduce the transfer frequency from the brake to the steering wheel. The first two modes of the wheel are the dominant vibration modes, and the vibration signal of the brake pedal has similar components to the steering wheel, except for showing lower vibration amplitudes in the natural frequencies of the transfer path [50]. Meyer, Ralf [51] studied disc brake judder that is attributable to thickness variations in the disc and that these deviations from the ideal plane surface can be caused either by wear and corrosion or by thermal stresses (changes within the microstructure of the disc material). They are termed “cold judder” and “thermal judder” respectively. It is known that automotive brakes and clutches can fail at elevated temperatures and thermal stresses due to the frictional heat generation at the contact surfaces during brake operations or clutch engagements. The mechanism of failure, however, varies depending on the operating conditions. Thermal buckling is believed to be one of the dominant failure mechanisms in clutch plates due to their small thickness [52]. It cannot be said the same for brake rotors due to their slightly bigger thickness and non-axisymmetric geometry. Stibich, Paul R., et al. [53] developed a technique to predict thermal buckling by obtaining temperature profiles from a heat transfer analysis and applied in the buckling analysis.

Audebert et al. [54] study on buckling of automotive clutch plates due to thermoelastic residual stresses revealed that clutch plates subjected to axisymmetric temperature excursions can develop residual in-plane bending moments of sufficient magnitude to cause buckling during unloading. The coning mode occurred when the residual stress at the outer radius was tensile, and the potato chip mode occurred when it was compressive. Ma [55] extended the method to automotive disc brakes and investigated the effect of geometric and material parameters on the critical buckling loads via the finite element method. These studies revealed that both axisymmetric and non-axisymmetric buckling modes can be caused by a uniformly distributed thermal loading in the circumferential direction. In addition, a slightly changed temperature profile in the radial direction can greatly affect the buckling modes.

In previous investigations of thermal buckling, a simplified geometry of an annular ring was used and assumed a hundred percent contact area at the frictional interface during braking. However, if there is some vibrational deflection, the contact area at the frictional interface will be affected by the vibrational distortion which can affect the distribution of the temperature generated during braking. Therefore, it is essential to study the coupling between vibration and thermal buckling. The present work will investigate the coupling of vibration and thermal buckling in brakes by considering various vehicle speeds that affect the vibration modes and investigate if vibration does increase the possibility of thermal buckling. It should also be noted that vibration modes can also be excited by the thermal buckling modes. Palmer, E, et al. [56] stated that in high-demand braking applications, vented discs are increasingly being used as these are considered to have high heat-dissipating characteristics. Therefore, a more realistic vented brake model will be analyzed in this study. Based on previous works, finite element analysis has proven to be efficient in analyzing vibrations and thermal buckling. Therefore, a finite element method is chosen for the coupling numerical study of vibration and thermal buckling in automotive brake discs.

2.2 METHOD

The geometric model of the brake rotor is based on the benchmark brake model for squeal analysis in ABAQUS [57]. Cast irons are commonly used in brake discs production because of low costs of production, the excellent thermal conductivity, the ease of dissipating heat generated by the friction of the pads during a stop, and the capacity of damping vibrations, which are prime characteristics of this kind of component [58]. Therefore, cast iron was the chosen material in this study for the brake rotor. The meshed 3D model is a mixture of 8-noded hex element (C3D8) and wedge elements (C3D6) with 25,457 nodes and 17,105 elements. Figure 2.1 shows the brake rotor in the meshed state before the analysis is conducted. Table 2.1 shows the dimensions of the brake rotor and Table 2.2 shows the material properties for gray cast iron. Figure 2.2 shows a cross-section schematic of a disc brake rotor to illustrate the dimensions shown in Table 2.1, where C.L represent the center line or rotation axis. The setup for the study only required some constraints to be placed on the model. The constraints on the model followed a realistic boundary condition for a brake rotor, where the brake rotor is fixed to the wheel of the car via the bolts, and the inner and outer radii are free. The same constraints were used in both the vibration and thermal buckling simulations. Initial conditions were imposed on the brake rotor for both the vibration and thermal buckling studies. The applied initial conditions for the vibration and thermal buckling simulations are rotational velocity in rad/s and prescribed temperature field in degree celsius respectively. Highway speed, interstate speed, and school zone speed limits were used in the vibration study and converted to rotational velocity using equation 2.2.

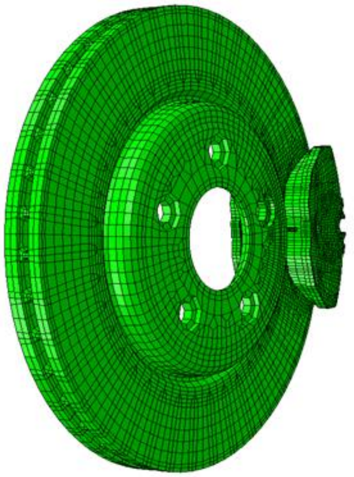

Figure 2.1**:** Finite element model of a brake disc*.

*Based on the brake squeal analysis benchmark model in ABAQUS

Table 2.1: Geometric dimensions of the brake rotor

	Outer Radius	Inner Radius	Hat Radius	Hat Height	Thickness
Symbol	Ro	Ri	Rh	Hh	t
Unit	mm	mm	mm	mm	mm
Value	144	32	92	13	20

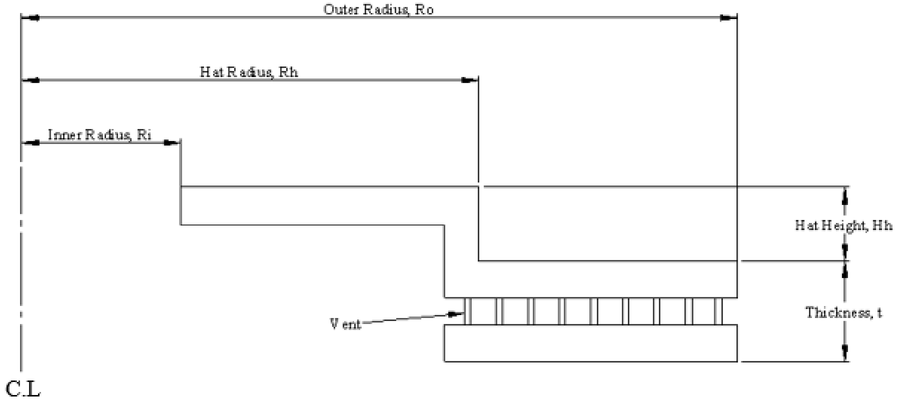

Figure 2.2: Cross-section schematic of a disc brake rotor

Table 2.2: Material properties of the brake rotor

	Young's Modulus	Mass Density	Poisson's Ratio	Thermal Expansion	Thermal Conductivity	Specific Heat
Symbol	E	ρ	ν	α	k	Cp
Unit	MPa	Kg/m3	NA	10-5/K	W/m*K	J/kg*K
Value	66178.1	7200	0.27	1.2	45	510

Various temperature profiles are used in the thermal buckling analysis. Linear, exponential, and sinusoidal distributions have been found among the most representative temperature profiles. The linear distribution can be caused by the sliding speed as a linear function of the radius and by the fact that the frictional heat generation rate is a linear function of the sliding speed. The sinusoidal distribution is related to the local high-temperature regions known as hot spots that could be excited by thermoelastic instability. An exponential distribution can be caused by the non-uniform convective cooling on the surface or a non-uniform contact pressure during the engagement and separation of the sliding bodies. For reasons stated earlier, a linear, sinusoidal, and exponential temperature profiles are used in the buckling simulation. In this study, a maximum temperature of 250°C was assumed for all buckling simulation to correspond with Belhocine Ali, and Mostefa Bouchetara's [59] finding of average temperatures through a disc thickness of three types of cast irons. For the purpose of this paper, it is also assumed displacement is proportional to temperature as shown in equation 2.1, chosen to quantitate the coupling analysis. The coupling study consists of four consecutive steps. The first step is the vibration simulation and exporting the resulting displacement from the simulation into excel. The second step is calculating the k value and generating a nodal temperature data. The k value is calculated using the maximum displacement obtained from the vibration simulation and calculated to have the node with the corresponding maximum displacement have a maximum temperature of 250°C. The value of k is then multiplied by the displacement results obtained from the simulation to generate a dataset of nodal temperatures. The third step, a plot of temperature as a function of the nodes radial and axial locations is created and a regression toolbox is utilized to fit an equation to the curve that best describes the plot. The last step, the equation obtained in the third step is used to describe the prescribed temperature field varying in the radial or axial direction for the thermal buckling simulation. All loading and constraint conditions applied follow a cylindrical axis system radial (R), circumferential (theta, θ), and axial (z).

$$U_{ji} \alpha \frac{1}{k} \times T_i \qquad 2.1$$

Where U, T, i, and j represents nodal displacement, nodal temperature, current node, and direction (R, theta, or Z)

2.3 RESULTS AND DISCUSSIONS

2.3.1 EFFECT OF ROTATIONAL SPEEDS ON VIBRATION

The rotational velocity was calculated using equation 2.2, assuming a traveling speed of the vehicle in miles per hour (mph). The speed of the vehicle in miles per hour (mph) is then converted to meters per hour and then to meters per minute. Using the circumference of the wheel in meters, convert meters per minute to revolutions per minute (rpm), which is then converted to rotational velocity in radians per second (rad/s).

$$\mathrm{RV} = \mathrm{S_v} \times \left(\frac{1609.34}{3600 \times R}\right) \qquad 2.2$$

Here, RV represents rotational velocity in radians per second, S_v represents the speed of the vehicle in miles per hour and R represents the radius of the wheel in meters, not to be confused with the radius of the brake rotor. The radius of the wheel used in this study is based on Daws, J. W., et al [60] Chevrolet Avalanche wheel radius of 0.389m. Using equation 2.1, the calculated rotational velocities from speeds of 25mph, 55mph, and 75mph are 29rad/s, 63rad/s, and 86rad/s respectively. Table 2.3 shows the result obtained from the vibration simulation with the calculated rotational velocities. As seen in Table 2.3, the displacement got lower at higher speeds. It should be noted the displacement is the resultant displacement.

Table 2.3: Vibration study results

Element Type		C3D8 & C3D6		
Rotational Velocity [rad/s]		29	63	86
Frequency [Hz]		674.11	670.55	667.65
Displacement [mm]	Maximum	5.34	4.95	4.76
	Minimum	0	0	0

The corresponding vibration mode with a rotational speed of 86rad/s is shown in Figure 2.3. Figure 2.3 also shows an out-of-plane vibration first mode displacement. The color represents the values of the resultant displacement, where red and blue correspond to the maximum and minimum value respectively. Red represents deflection in the positive z axis, and blue represent deflection in the negative z axis.

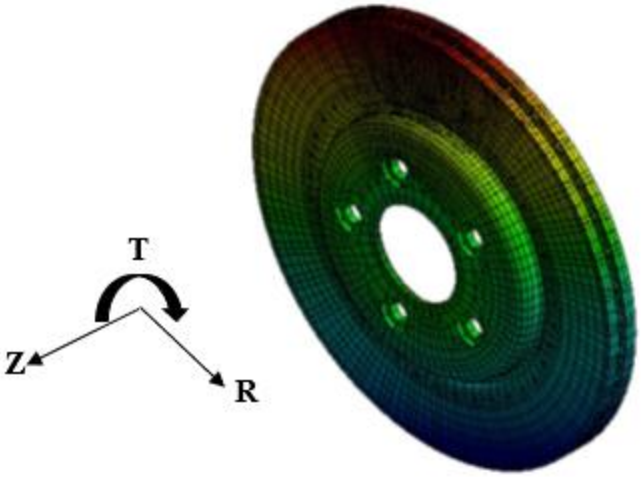

Figure 2.3**:** Mode 1 axially deformed result at 86rad/s of the brake rotor

A path parallel to the global y-axis was created on the brake disc midplane to describe the brake discs' radial location. Another path parallel to the global z-axis was created on the brake disc top plane to describe the brake discs' axial location. Figure 2.4 and Figure 2.5 are plots of displacement as a function of the brake discs' axial location and radial location respectively at 86rad/s. The zero values shown in Figure 2.4 represent the vent space and the hollow area of the rotor hat, while the zero value in Figure 2.5 represent the empty area of the inner radius. The x-axis in Figure 2.4 - Figure 2.5 and Figure 2.9 - Figure 2.10 represent in mm the radial and axial locations on the created paths, and the y-axis in Figure 2.4 and Figure 2.5 represents the nodes' displacement in mm at the corresponding locations. While the y-axis in Figure 2.9 and Figure 2.10 represents the temperature of each node in the radial and axial direction.

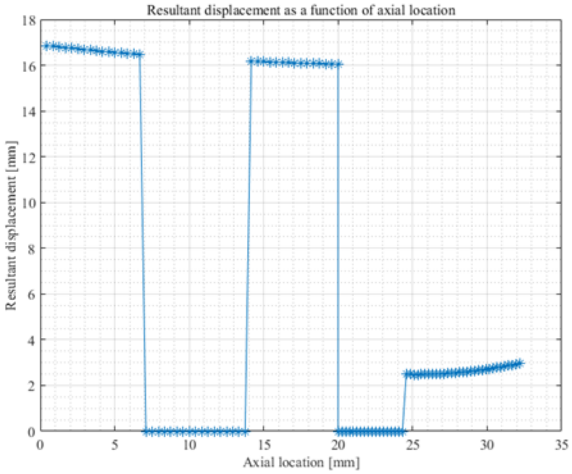

Figure 2.4: Resultant displacement vs. axial location

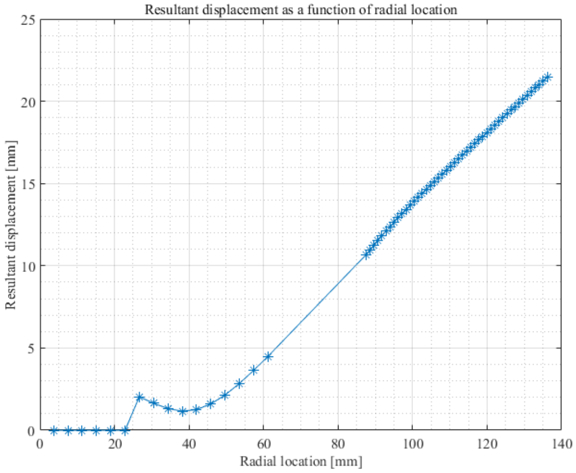

Figure 2.5: Resultant displacement vs. radial location

2.3.2 EFFECT OF TEMPERATURE PROFILE ON THERMAL BUCKLING

The critical buckling temperature is defined as the product of the highest nodal temperature and the computed eigenvalue in equation 2.3.

$$T_{cr} = \lambda_i T_{max} \qquad 2.3$$

Where T_{cr}, λ_i, and T_{max} represents the critical buckling temperature, eigenvalue, and maximum nodal temperature. The eigenvalue determines the lowest acceptable thermal load before buckling occurs. The temperature profile affects the critical buckling temperature and the associated buckling deformation mode which is evident in Table 2.4. The temperature distributions in the analysis are set as increasing from the hat radius to the outer radius of the rotor following either a linear, sinusoidal, or exponential pattern, meanwhile having the inner and outer radii free to move but constrained at the bolt holes. Figure 2.6 shows a radially increasing linear temperature profile applied to the brake rotor. Figure 2.7 shows the first and third buckling modes respectively, which are also known as the potato chip and coning modes because of the resemblance to a potato chip and cone. Figure 2.8 shows an axially distributed linear temperature. Equations 2.4, 2.5, and 2.6 describe the linear, sinusoidal, and exponential temperature profiles used for the bucking study respectively.

$$228 \times \left(\frac{R - 32}{144 - 32}\right) + 22 \tag{2.4}$$

$$228 \times sin\big(0.0302 \times (R - 32)\big) + 22 \tag{2.5}$$

$$\frac{228 \times (\exp\big(0.104 \times (R - 32)\big) - 1)}{4.3 \times (144 - 32)} + 22 \tag{2.6}$$

The equations and constants are chosen such that the temperature difference for each scenario is the same at 228°C across the radius, with a low of 22°C at the inner radius and a high of 250°C at the outer radius. The blue color in the figures indicates the low temperature and the red indicates the high temperature.

Table 2.4: Buckling temperature with obtained simulation eigenvalues.

Temperature Profile	Linear	Sinusoidal	Exponential
Eigenvalue	25.637	23.688	38.259
Buckling Temperature [°C]	6409.25	5922	9564.75

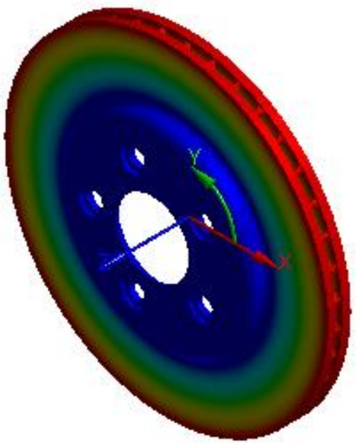

Figure 2.6**:** Linear temperature profile in the radial direction

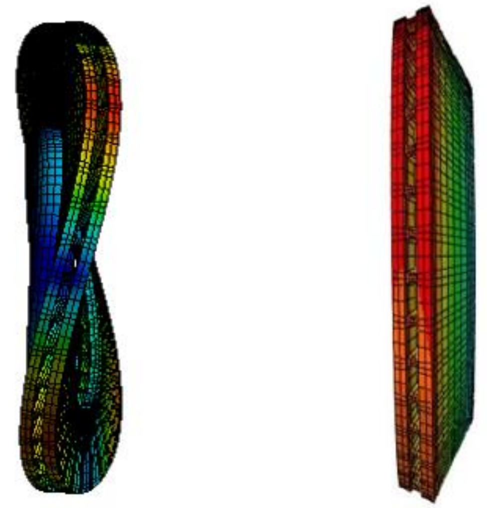

(a) (b)

Figure 2.7: Buckling modes for linear temperature radially distributed: (a) Mode 1 “potato chip mode; (b) Mode 3 “coning mode”

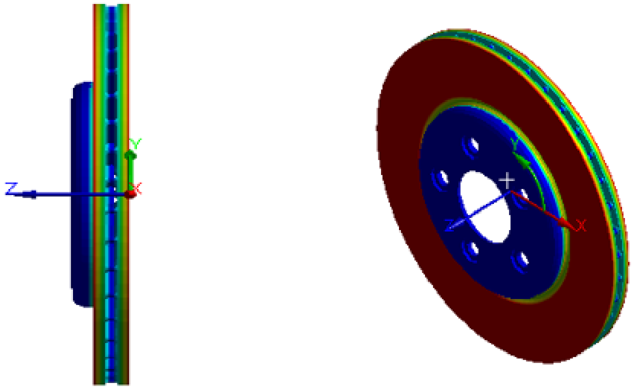

(a) (b)

Figure 2.8: Linear temperature distributed axially: (a) Side View; (b) Isometric view.

The axially distributed temperature is shown to reduce linearly from the outer surface to the midplane of the rotor thickness. The resulting mode 1 eigenvalue, and buckling temperature associated with this axially distributed temperature are 82.256 and 20,564°C respectively. This result shows that a temperature distributed axially has a significant effect on the buckling temperature than a temperature distributed radially.

2.3.3 EFFECT OF VIBRATION ON THERMAL BUCKLING

Due to the initial assumption shown in equation 2.1, the temperature profiles follow the same profiles as the displacement plots shown in Figure 2.4 and Figure 2.5. Table 2.5 and Table 2.6 show the calculated values for k, based on the maximum resultant displacement obtained from the vibration simulation. Figure 2.9 and Figure 2.10 are plots of the nodal temperature vs. radial location and of nodal temperature vs. axial location respectively. The maximum and minimum temperatures calculated using equation 2.1 are 249.99°C and 23.719°C respectively. Table 2.7 and Table 2.8 Table 2.8 show the resulting eigenvalues and buckling temperatures in the presence of vibration.

Table 2.5: Values of k based on the displacement vs radial location for each rotational velocity.

Rotational Velocity [rad/s]	29	63	86
Maximum Displacement [mm]	4.81	4.46	4.29
Value of k	51.98	56.05	58.28

Table 2.6: Values of k based on the displacement vs axial location for each rotational velocity.

Rotational Velocity [rad/s]	29	63	86
Maximum Displacement [mm]	3.78	3.50	3.37
Value of k	66.14	71.43	74.14

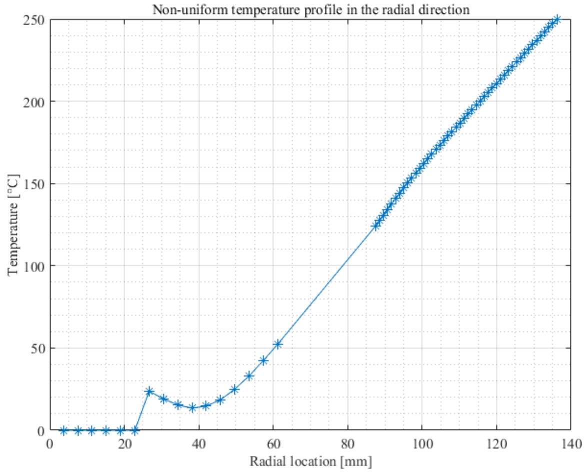

Figure 2.9: Radial temperature profile associated with 86rad/s rotational velocity.

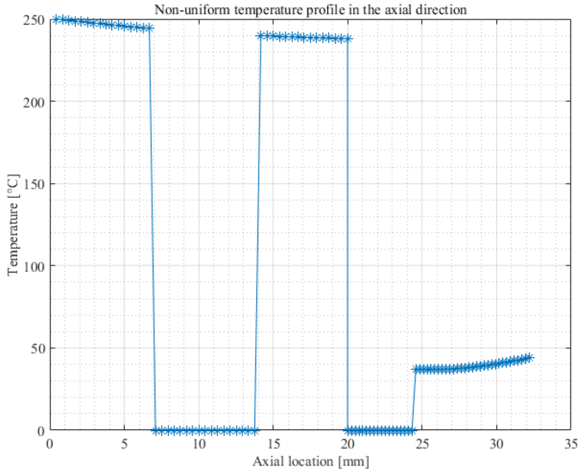

Figure 2.10: Axial temperature profile associated with 86rad/s rotational velocity.

A curve fitting technique was utilized to generate an expression for the radial temperature profile varying from the inner radius to the outer radius shown in Figure 2.9 and the axial temperature profile shown in Figure 2.10. The technique determined an eight-order polynomial best fits the radial temperature profile in the form shown in equation 2.7 and a sinusoidal model for the axial temperature profile in the form shown in equation 2.8.

$$\mathrm{p}_1\mathrm{x}^8 + \mathrm{p}_2\mathrm{x}^7 + \mathrm{p}_3\mathrm{x}^6 + \mathrm{p}_4\mathrm{x}^5 + \mathrm{p}_5\mathrm{x}^4 + \mathrm{p}_6\mathrm{x}^3 + \mathrm{p}_7\mathrm{x}^2 + \mathrm{p}_8\mathrm{x} + \mathrm{p}_9 \qquad 2.7$$

$$a_1 \sin(b_1 + c_1) + a_2 \sin(b_2 + c_2) + \cdots + a_8 \sin(b_8 + c_8) \qquad 2.8$$

Table 2.7: The buckling temperature at the studied rotational velocities with a radially distributed temperature

Rotational Velocity [rad/s]	29	63	86
Eigenvalue	38.107	39.857	38.109
Buckling Temperature [°C]	9527.035	9536.875	9527.056

Table 2.8: The buckling temperature at the studied rotational velocities with an axially distributed temperature

Rotational Velocity [rad/s]	29	63	86
Eigenvalue	119	119.19	119.2
Buckling Temperature [°C]	29795.137	29798.430	29799.452

2.3.4 EFFECT OF BUCKLING MODE ON VIBRATION MODE

In a coupling situation, the phenomenon coupled is suspected to influence each other. Therefore, the study of the effect of thermal buckling modes on vibration modes is conducted. The buckling modes obtained thermal buckling simulation with various temperature profiles are used as influencers in the vibration simulation to determine the influence of thermal buckling on vibration. The displacement obtained from the first buckling mode is used as an initial condition in addition to the rotational velocity for the vibration study. The resulting displacement from this vibration simulation is larger because the overall displacement is a concatenation of the initial nodal displacement and the displacement resulting from the rotational velocity.

2.4 CONCLUSION

It can be concluded that vibration during braking does not significantly increase the chance of buckling for the ABAQUS benchmark model, the results are highly dependent on the chosen parameters including materials, dimensions, and rotational velocity, and the coupling can be strong in some conditions. This is evident as shown in Table 2.7 and Table 2.8 the buckling temperatures are greater than the operating temperatures of 250°C. Vibration modes are affected in the presence of thermal buckling, the displacement present during thermal buckling tends to excite the vibration modes. It is also noted in Table 2.7 and Table 2.8 that the difference in the buckling temperature is not significant, because the displacements witnessed during vibration at the studied speeds were relatively close. At different speeds other than what was studied in this paper might show a significant difference in the buckling temperatures.

CHAPTER III

INSTABILITIES INDUCED BY THERMAL-MECHANICAL COUPLINGS IN CLUTCH AND BRAKE DISCS

3.1 INTRODUCTION

Thermoelastic instability (TEI) and thermal buckling are among the most important failure mechanisms in automotive clutches and brakes [54,61]. Heat due to friction in sliding systems has a proportional relationship to the sliding speed, and the contact pressure between the friction disc and metal disc is nominally uniform. During sliding there is a point known as the critical sliding speed. When the sliding speed exceeds the critical sliding speed the pressure disturbances on the contacting interfaces can grow rapidly. When the speed is above the critical value, the pressure or temperature disturbances may become unstable [62,63]. As a result, the contact would become separated regions on the sliding interface [21]. Zagrodzki et al. [64] studied the transient behaviors of TEI. Burton et al. [62] first applied the perturbation method, which was later extended to more complex geometries, both analytically and numerically [63,65]. Yi et al. [66] developed the Fourier finite element model to investigate this phenomenon, while Jang and Ang [67] discovered that the functionally graded material coatings on the surfaces of the metal discs increase the dominant critical speed. Zhao et al. [68] further revealed that the friction material properties affect the dominant deformation modes. On the other hand, it is well known that thermal buckling is induced by the condition when the hoop stress due to thermal expansion reaches a critical value [69]. Because of its practical significance, a lot of effort has been devoted to this field. Some prior achievements have been summarized by Tauchert and Thornton [70]. Audebert et al. [54] evaluated the thermal buckling of clutch discs based on Timoshenko's [52] beam theory. Ma studied the effects of geometric parameters and material properties on thermal buckling numerically. It was found that both coning and wavy deformation modes can be excited. Najafizadeh et al. [71] studied the thermal buckling behavior of a circular disc on the basis of first- and higher-order shear deformation theories. Multiple researchers studied axisymmetric thermal buckling deformation modes and post buckling behaviors of annular plates analytically [72,73]. Zhao et al. [74] revealed that various types of temperature distributions produce different buckling deformation fields, and that the temperature distributions affect the critical buckling temperatures. Xiong et al. [75] experimentally studied thermal buckling in clutch discs and claimed that Timoshenko's beam theory is applicable to estimate the critical buckling temperatures.

In the previous investigations on thermal buckling, the temperature distributions were based on either experimental observations or plausible assumptions. For instance, the assumed linearly distributed temperature field was based on the fact that the heat generation is proportional to the linear sliding speed. However, the temperature fields can be strongly altered by the excited TEI temperature modes, which might be significantly different from those assumed previously. Therefore, it is essential to study the coupling between TEI and thermal buckling. The current study aims at assessing the susceptibility of thermal buckling in the presence of TEI, particularly how the TEI temperature modes affect the critical buckling temperatures and the corresponding deformation modes. Hotspotter© [76] (a numerical tool investigating TEI) is used to generate the required temperature fields. The commercial finite element software is subsequently used to obtain the thermal buckling deformation modes and the corresponding critical buckling temperatures. It should be noted that thermal buckling can affect TEI as well, as the contact pressure and the frictional heat generation rate may change in a buckled disc.

The focus in this chapter is on the effects of TEI on thermal buckling only, due to the difficulties in mathematical formulation for the reverse process. We will endeavor to solve this problem in the future.

3.2 METHOD

There are two consecutive steps to this chapter's analysis. The first step is utilizing Hotspotter to obtain TEI temperature modes and the corresponding temperature distributions. The second step is performed using ABAQUS to investigate the critical buckling temperatures and the associated buckling modes. The dimensions and material properties of the model are based on a representative metal disc from an automotive application found in the literature [74]. According to the fundamental TEI theory, the temperature perturbation can be written in the following form in the cylindrical coordinate system:

$$T(r,\theta,z,t) = \Re\left\{e^{bt+jn\theta}\Theta(r,z)\right\} \qquad 3.1$$

$e^{bt+jn\theta}$ is a complex number. Where b is the growth rate, j represent imaginary, t is the time, Θ is eigenvector, and n is the spatial frequency which is equivalent to the number of hot spots in the circumferential direction; r, q and z represent the positions in the radial, circumferential, and axial directions, respectively. The resulting problem is defined by an eigenvalue equation in which the temperature growth rate, b is the eigenvalue [61]. When the sliding speed is specified, the temperature distributions excited by TEI modes can be obtained.

A computational model can be developed through an input script file in Hotspotter. The format of the Hotspotter input file is similar to that of ABAQUS. The coordinates of the nodes located on the surfaces of each disc were generated first. The interior nodes were then generated by specifying the number of intervals through the thickness direction. The 3-D model was then developed by sweeping the cross-sectional geometry in the circumferential direction to cover the entire plane. In the input script the initial conditions (sliding speed) including boundary conditions, and mechanical and thermal material properties are specified. Included in the output file obtained after the simulation is completed is the nodal temperature of the dominant TEI modes. Only the nodal temperatures of the metal disc were used in the subsequent buckling analysis.

The resulting TEI temperature modes from the first step can be classified into two categories. The first category is “banding modes”, in which the temperature is uniformly distributed in the circumferential direction, meanwhile, the distribution of temperature in the radial direction could be arbitrary. Figure 3.1 (a) shows a banding TEI mode. It can be seen that there are several annular regions on the disc surface. In this figure, the different temperatures are represented by different colors. The second category of TEI temperature modes is “focal modes” or “hot spots”. It can be seen in Figure 3.1 (b) that there are several red (i.e., high temperature) and blue (i.e., low temperature) regions around the circumferential direction. Thus, in the focal modes the temperature varies not only in the radial direction but also in the circumferential direction.

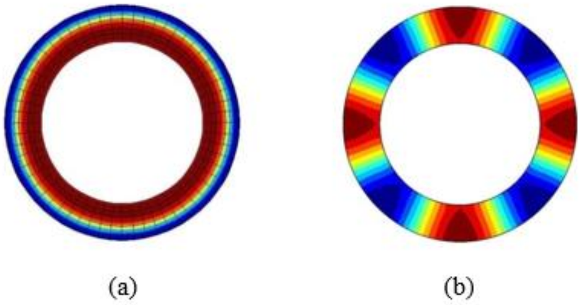

Figure 3.1: Simulated temperature variations excited by TEI in a ring disc: (a) banding mode; (b) focal mode.

The governing equation defining the eigenvalue problem of buckling is shown below.

$$\left([K] + \lambda_{cr}[K_{\sigma}]_{ref}\right)\{\delta D\} = \{0\} \qquad 3.2$$

Here the term "*ref*" represents the reference load, i.e., a load that is first applied to the structure to find the reference stress stiffness matrix, $[K_{\sigma}]_{ref}$. Another load $\{R\} = \lambda_{cr}\{R\}_{ref}$ will then be applied to the structure, where λ_{cr} represents an arbitrary multiplier to the original reference load. Multiplied by δD the buckling mode shapes (eigenvectors).

ABAQUS input script is required in the buckling analysis (i.e. the second step) to make the geometry and model descriptions consistent. The algorithm described in equation 3.2 is incorporated into the "*BUCKLE*" analysis procedure in ABAQUS. The reference loads in the current study are defined in the ABAQUS input script files and not the interactive dialogue window. This is because the temperature profiles can be in arbitrary forms, and it is difficult to define them by closed-form mathematical functions. The critical buckling load for any buckling analysis under either mechanical or thermal loading, is the product of the calculated critical buckling eigenvalue and the applied load.

The selection of the element type used in the current research is critical. Although the temperature distributions are circumferentially uniform, using axisymmetric element types is inappropriate for the banding TEI temperature modes as these elements would yield the axisymmetric buckling deformation modes only. In reality, it has been found that the non-axisymmetric deformation modes may also be dominant in some applications. Moreover, in the prior works on thermal buckling, the shell element type was often implemented to improve the computational efficiency, based on the fact that the temperature variation is usually negligible in the thickness. However, when the TEI effect is taken into account, the temperature oscillates rapidly through the thickness and therefore the temperature gradient is non-negligible. Thus, the three-dimensional elements are used in the current study to account for the temperature gradients in all three directions.

3.3 RESULTS AND DISCUSSIONS

3.3.1 CONVERGENCE STUDY

A convergence study was conducted as a way to validate the finite element results. The material properties and geometric dimensions are listed in Table 3.1. It should be explained that the parameters used in the table, especially those for the friction disc, were from a simplified clutch model. In reality the friction disc has a metal core covered by a layer of friction lining on both sides. In the current study the friction disc has been simplified into a single layer of friction lining only, to demonstrate a proof of concept. This simplification, however, does not affect the main conclusions drawn from the study. Also, the material used for the metal disc is steel rather than cast iron in a typical brake disc. The schematic in Figure 3.2 shows a metal disc sliding between two friction discs.

Table 3.1: Material properties and dimensions of the model used in the analysis.

	Parameter	Metal Disc	Friction Disc
Inner Radius	R_a (mm)	86	86
Outer Radius	R_b (mm)	125	125
Thickness	h (mm)	3	6
Elastic Modulus	E (GPa)	160	2.26
Poisson's Ratio	ν	0.29	0.29
Coefficient of Thermal Expansion	α (10^{-6}/K)	12.7	12.1

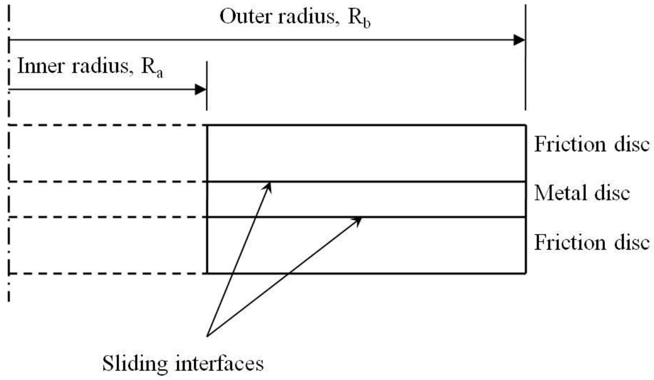

Figure 3.2: Schematic of the cross section of the TEI model.

The chosen element types for TEI model developed in Hotspotter are C3D8 three-dimensional hexahedral) and 2DF (two-dimensional Fourier). Because of the substantial bending moment in thermally buckled disc, a C3D8I element (three-dimensional hexahedral elements with incompatible mode) was chosen, and it is believed that the incompatible elements exhibit better bending performance compared to the regular elements (C3D8).

The temperature variations in the thickness direction are evident in the presence of TEI; therefore, multiple elements were generated through the thickness. The meshes in the friction discs were biased toward the sliding interfaces to account for the large temperature gradients. Three different meshes were tested, and the results are shown in Table 3.2. The mesh size is represented by the product of the element numbers along the three directions: radial, thickness and circumferential, respectively. The largest growth rate (at which the formation of hotspots occurs) of the disturbance was selected as the standard for comparison. It is noted that the maximum difference between the fine mesh (I) and the coarse mesh (III) is only around two percent.

Table 3.2: A comparison of the results using different meshes in TEI analysis.

	Mesh Type		
	I	II	III
Metal Disc	8x4x60	6x3x48	4x2x30
Friction Disc	8x15x60	6x10x48	4x5x30
Simulation Time (s)	4832.31	1237.35	47.70
Largest Growth Rate	1.960	1.962	2.004
Percent Error (%)	NA	1.02	2.24

In addition, convergence tests were performed on the banding TEI temperature modes obtained from the two-dimensional Fourier FEA models. The two-dimensional models generate temperature distributions of TEI modes on the cross-sections of discs, which can be used to reconstruct the three-dimensional temperature fields. The computational results obtained from the three different meshes are presented in Table 3.3. All results have been compared on the basis of the growth rate of mode 0 in which the hot spot number is equal to 0 (i.e., the banding TEI temperature mode). It can be found that the maximum difference among the results is around two percent. As the finest mesh is computationally intensive, the mesh with a medium density (i.e., the mesh shown in the third column in Table 3.3) was chosen to balance the computational accuracy and efficiency.

Table 3.3: Convergence test for TEI analysis.

	Mesh Type		
	I	II	III
Metal Disc	33x9	22x6	11x8
Friction Disc	99x24	22x16	11x3
Simulation Time (s)	5824.66	353.73	113
Largest Growth Rate of mode 0	$1.587\text{x}10^{-4}$	$1.600\text{x}10^{-4}$	$1.636\text{x}10^{-4}$
Percent Error (%)	NA	0.82	2.25

Convergence study was also performed on thermal buckling. As the buckling deformation mode with the lowest critical buckling temperature is the most important one, its buckling temperature was chosen as the indicator of convergence. In order to compare the current results with the prior results reported by the pioneering researchers, the temperature distributions in the testing models were set as linearly increasing from the inner radii to the outer radii of discs, meanwhile the inner and outer radii are free to move. Another mesh in which there are 16, 8 and 120 elements in the radial, thickness and circumferential directions respectively was created for the comparing purpose. As shown in Table 3.4, the mesh in which there are 8, 4 and 60 elements in the radial, thickness and circumferential directions respectively should be selected.

Table 3.4: Convergence test for thermal buckling analysis.

Mesh	0	1	2
Metal Disc Meshes	16x8x120	8x4x60	6x3x48
Buckling Temperature [°C]	-177.45	-177.65	-178.11
First Buckling Mode	Coning	Coning	Coning
Error (%)	NA	0.11	0.37

Analytical solutions were used to validate the computational model. Based on Timoshenko's beam theory, the critical bending moment that causes the buckling of an annular ring can be determined by the following equations.

$$K = \frac{1+\nu}{2};\ a = R_b - R_a;\ R = \frac{R_a+R_b}{2}; \tag{3.3}$$

$$M = \frac{1+K}{2} \pm \sqrt{\left(\frac{1-K}{2}\right)^2 + Kn^2} \tag{3.4}$$

In the above equations, K, ν, M, n, R_a and R_b represent the stiffness ratio, Poisson's ratio, the dimensionless critical bending moment, the buckling wave number, the inner radius, and the outer radius respectively. When n=0 (i.e., the coning mode), the two calculated values of M are 1 and 0.65. The smaller value of M should be used to calculate the critical bending moment.

The bending moment caused by the thermal stress in an annular ring can be obtained through the following equation.

$$M_b = \int_{R_a}^{R_b} t\sigma_{\theta\theta}(r)(r-R)dr \tag{3.5}$$

When the inner and the outer radii are free, $\sigma_{\theta\theta}$ can be expressed as,

$$\sigma_{\theta\theta}(r) = \frac{\alpha E}{r^2}\int_{R_a}^{r} rT(r)dr - \alpha ET(r) + \frac{EC_1}{1-\nu} + \frac{EC_2}{(1+\nu)r^2} \tag{3.6}$$

$$C_1 = \frac{\alpha}{2(1-\nu)} \frac{1}{R_b^2 - R_a^2} \int_{R_a}^{R_b} rT(r)dr \qquad 3.7$$

$$C_2 = \frac{\alpha(1+\nu)R_a^2}{R_b^2 - R_a^2} \int_{R_a}^{R_b} rT(r)dr \qquad 3.8$$

$$T(r) = \frac{\Delta T}{R_b - R_a}(r - R_a);\ \Delta T = T_b - T_a \qquad 3.9$$

where α, $T(r)$ and ΔT represent the coefficient of thermal expansion, the temperature distribution along the radial direction and the temperature difference between the outer and inner radii, respectively. By solving the above equations, it is found that the relation between the bending moment, M_b and the temperature difference, ΔT is

$$M_b = -0.76559\Delta T \qquad 3.10$$

The bending moment M_b is -133.08. Therefore, when the buckling wave number is 0, the critical buckling temperature is 173.83ºC. It should be mentioned that the predefined temperature distribution is linearly increasing from the inner radius to the outer radius. The negative value of the bending moment indicates that the calculated temperature is linearly decreasing from the inner radius to the outer radius.

A comparison between the analytical and numerical results for the critical buckling temperatures is shown in Table 3.5.

Table 3.5: Verification of the FEA model for thermal buckling.

Buckling Wave Number	0	2	3
Buckling Temperature Analytical Result (°C)	-173.83	213.85	429.42
Buckling Temperature FEA Result (°C)	-177.65	212.83	426.44
Error (%)	2.20	0.48	0.69

It should be noted that mode 1 (i.e., *n*=1) represents a rigid body motion and therefore can be ignored.

3.3.2 EFFECTS OF BOUNDARY CONDITIONS

The effects of boundary condition were investigated with sliding speed of 10 m/s, i.e., 97.79 rad/s or 933.83 RPM. The temperature distribution of the TEI temperature mode with the highest growth rate was used for the buckling analysis, as shown in Figure 3.3. Both circumferential and radial distributions of temperature are shown in Figure 3.3. It should be pointed out that the temperature disturbance shown in Figure 3.3 represents the normalized temperature given by the eigenvector. Any multiple of the temperature disturbance could be the actual temperature variation excited by TEI.

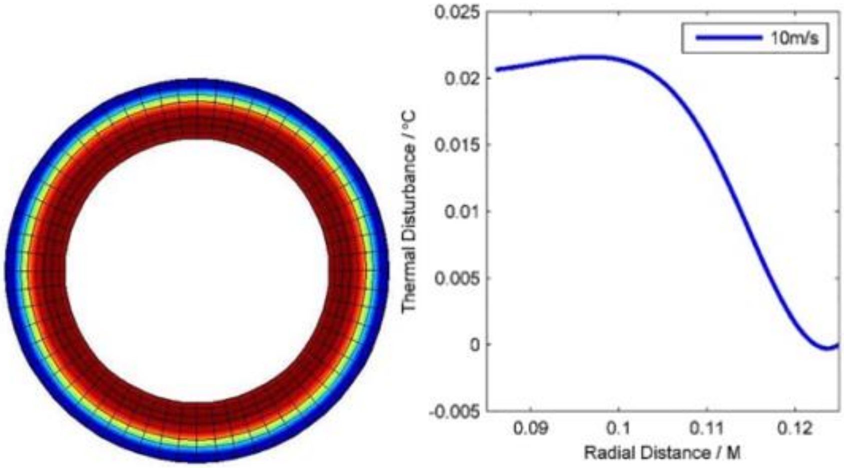

Figure 3.3: Normalized temperature distribution in the TEI model with sliding speed of 10 m/s.

The method described in the following section was developed to investigate the buckling modes and critical buckling temperature. Here the critical buckling temperature is defined as the product of the highest nodal temperature and the computed buckling eigenvalue.

The following was observed as the effect of boundary conditions:

- A fixed inner radius in all directions results in the dominant buckling deformation mode having a wavy shape with an eigenvalue of 1.54×10^5 and the corresponding critical buckling temperature of 3320 ºC, which can be considered as the upper bound of the result.
- A fixed inner radius in the radial and circumferential directions only results in a dominant buckling deformation mode with a lower order wavy mode with an eigenvalue of 8.90×10^4 and the corresponding critical buckling temperature of 1913.6 ºC.
- A fixed inner radius in the circumferential direction only results in a dominant buckling deformation mode which exhibits a “potato chip” like pattern with an eigenvalue of 2.99×10^4 and the corresponding critical buckling temperature of 643.84 ºC. This result is more meaningful for clutches as clutch discs are usually fixed by splines so that they can move freely in the axial direction, meanwhile the inner radius is allowed to move in the radial direction to a certain extent.

The corresponding simulated buckling modes are shown in Figure 3.4 (a), (b), and (c) respectively. The colors in these images represent the values of axial displacements and should be noted that the deformation is exaggerated. In the rest of the study, in order to prevent rigid body motions the inner radii of the models are fixed in the circumferential direction.

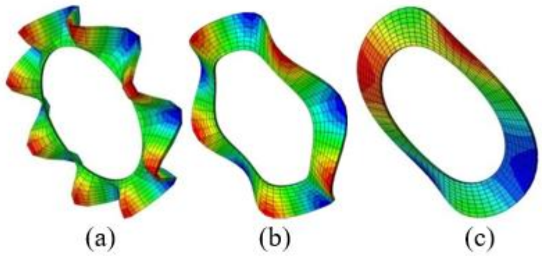
(a) (b) (c)

Figure 3.4: The thermal buckling deformation mode with the sliding speed of 10 m/s under different boundary conditions.

3.3.3 EFFECT OF RELATIVE SLIDING SPEEDS

To investigate the effects of sliding speed, the relative sliding speeds in the TEI model varied from 10 m/s to 50 m/s with an interval of 10 m/s. The obtained temperature profiles are shown in Figure 3.5. It can be seen that the locations of high and low temperature regions vary with the sliding speed, where the high temperature zones formed near the inner radius and low temperature zone at the outer radius at speeds of 10, 30 and 50 m/s and reversed at speeds of 20 and 40 m/s.

When the sliding speeds are set to 10 m/s, 30 m/s and 50 m/s and the inner radii of the metal discs are fixed in the circumferential direction only, the computed critical buckling eigenvalues are 2.99×10^4, 3.26×10^4 and 3.56×10^4 respectively and the corresponding critical buckling temperatures are 597.04ºC, 746.51ºC and 1083.06ºC respectively. It is found that the eigenvalue and the critical buckling temperature increase with the sliding speed. Meanwhile with the same boundary condition and speeds set to 20 m/s and 40 m/s, the critical buckling eigenvalues are 2.48×10^4 and 2.83×10^4 respectively and the corresponding critical buckling temperatures are 643.84ºC and 838.93ºC respectively. The eigenvalues increase with the ranges of temperature variations in the radial direction. Hence, the profile of temperature distribution can significantly affect the critical buckling temperature and the associated buckling deformation mode.

It should be noted that the sliding speed here is defined as the linear speed of the metal disc. When a brake disc rather than a clutch disc is considered, the actual vehicle speed would be used. Assuming the case of a brake, with the car tire radius dimension of 300mm, then the ratio between the two radii (i.e., the tire radius divided by the radius of brake disc) would be 3:1 approximately. Therefore, a sliding speed of 10 m/s in the brake disc could be equivalent to a vehicle speed of 67 MPH; and a speed of 50 m/s in the brake disc would be equivalent to 112 MPH.

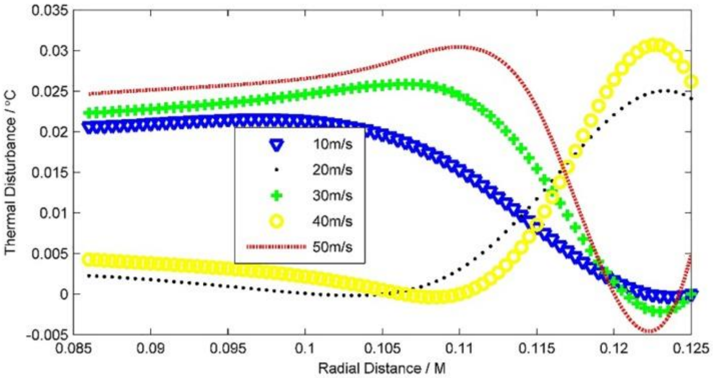

Figure 3.5: Temperature variations with different sliding speeds.

3.3.4 EFFECT OF COEFFICIENT OF FRICTION

To investigate the effects of coefficient of friction (CoF), we varied it from 0.13 to 0.65, with an interval of 0.13. Meanwhile, the other parameters were unchanged. As the coefficient of friction does not alter the pattern of the TEI temperature mode, the temperature profiles are similar to that of the reference model (CoF 0.13). The outer radius is a blue circle at a lower temperature, and the inner radius is a red ring at a higher temperature in each temperature distribution. The temperature variations in the radial direction are shown in Figure 3.6.

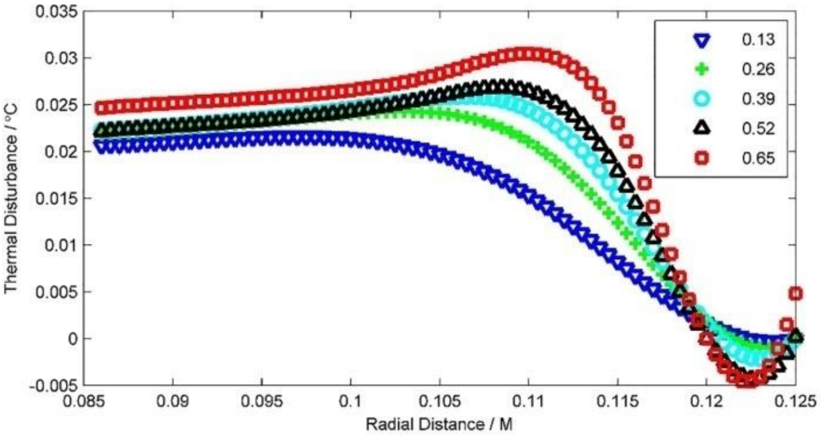

Figure 3.6: Temperature variations with different coefficients of friction.

It is noticed that the range of temperature variation (i.e., the difference between the highest temperature and the lowest temperature) increases with the coefficient of friction. The buckling eigenvalues are 2.99×10^4, 30.9×10^4, 3.26×10^4, 3.47×10^4 and 3.56×10^4 respectively and the corresponding critical buckling temperatures are 643.84 ºC, 743.85 ºC, 838.93 ºC, 915.45 ºC and 1054.15 ºC respectively. The buckling deformation modes are similar to that shown in Figure 3.4 (c).

It should be noted that the critical buckling temperatures increase rapidly with the coefficient of friction. The lowest critical buckling temperature is 643.84 ºC and the highest is 1054.15 ºC which corresponds to the smallest coefficient of friction at 0.13 and largest coefficient of friction at 0.65 respectively. Therefore, an increase in the coefficient of friction can reduce the chance of occurrence of thermal buckling in the system. On the other hand, an increase in the coefficient of friction leads to a higher growth rate of temperature, and thus increases the chance of thermoelastic instability occurrence. Consequently, this could be a more complicated process in real applications.

3.3.5 EFFECT OF FOCAL HOT SPOTS

Thermal buckling due to the focal temperature distributions was also evaluated. First the focal TEI temperature modes were generated using the “Full 3D” module in Hotspotter. The nodal temperatures on the cross-section were retrieved from the eigenvectors of the TEI solutions. The obtained nodal temperature distribution was then multiplied by the corresponding Fourier functions to reproduce the complete temperature fields in the three-dimensional domain. Two focal TEI temperature modes are shown in Figure 3.7. Apparently, there are six and two focal hot spots on the surface of each metal disc, respectively. The thermal buckling analysis was performed based on the temperature fields. For the three TEI modes, the buckling eigenvalues are 2.28×104 and 2.32×104 respectively and the corresponding critical buckling temperatures are 1818.70ºC and 1584.08ºC. These values are only theoretically important, as they are above the melting point of the material. In comparison, the maximum temperatures in clutch or brake in normal cars are typically below 1000ºC but can exceed 1000ºC in high performance race cars. Therefore, it is concluded that thermal buckling in metal discs is more likely to be induced by the banding temperature modes rather than the focal modes.

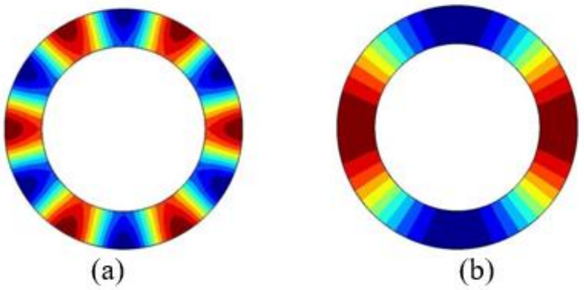

Figure 3.7: TEI generated focal temperature distributions a) six hotspots, b) two hotspots used in the thermal buckling analyses.

3.4 CONCLUSION

This study aims at investigating the effects of TEI-induced temperature variations on the thermal buckling phenomenon in sliding discs. The frictionally excited TEI temperature profiles were obtained by performing finite element analyses in the customized code Hotspotter. The temperature profiles were then used as the reference thermal loads in the subsequent analysis of thermal buckling. The critical buckling temperatures and the deformation modes were obtained numerically in ABAQUS. It can be concluded that TEI and thermal buckling can interact with each other under some conditions, because was found that thermal buckling can be excited by TEI-induced temperature variations and also shows that multiple factors including the coefficient of friction and the sliding speed can affect both TEI modes and critical buckling temperatures.

The parametric studies revealed that the critical buckling temperature increases with the friction coefficient, and that the TEI-induced temperature input can be altered by the sliding speed. The results show that the TEI modes with the temperature decreasing from the inner radius to the outer radius are relatively easier to buckle than the modes of a reversed temperature profile. The overall trend is that the critical buckling temperatures increase with the sliding speed. We also tentatively explored the possibility of thermal buckling induced by focal hot spots. It was found that, in the presence of focal hot spots, the minimum temperature for thermal buckling is typically much higher than the operating temperatures of metal discs, and therefore the coupling between focal TEI hot spots and thermal buckling is of less importance in brake applications.

CHAPTER IV

COMPUTATIONAL PARAMETRIC STUDY OF NONMETALLIC FRICTION MATERIAL ANISOTROPY AND ITS EFFECT ON THERMAL-MECHANICAL INSTABILITIES OF CLUTCHES AND BRAKES

4.1 INTRODUCTION

Anisotropic materials are materials that have directional-based material properties. They are discovered in materials found in nature with organic properties such as wood, muscles, and bones. The mechanical and thermal properties of an anisotropic material appear higher in certain directions such as in wood, for instance, it is shown to be stronger along (parallel to) the grain and weaker in directions perpendicular to the grain, and as such, research has been conducted on how to mimic such phenomena in other materials. One of the manufactured materials today that display such anisotropic properties are known as composite materials. Most friction materials today possess anisotropic properties. Friction materials generate friction to slow or decrease motion in applications including aerospace, automotive, railroad construction, heavy machinery manufacturing, forestry, oil and gas, mining, and defense. Depending on the application, friction materials may consist of phenolic resin, ceramics, advanced fibers, graphitics, metals, and metal alloys. Friction material formulations consist of various ingredients for wear resistance, thermal stability, and mechanical strength [24,77].

For example, automotive brake pads consist of embedded macro- and micro-constituents in cured phenolic resin and most contain macro-particles of copper due to excellent thermal conductivity to reduce localized overheating [78,79]. Existing laws and regulations in the states of Washington and California described in an article by the United States EPA [39] require the phase-out of copper and other heavy metals in brake pads to reduce contact of copper particulates from brake wear with stormwater and subsequent discharge into nearby waterways. Elevated levels of copper are toxic to aquatic life and adversely affect the survival, reproduction, and growth of fish, invertebrates, plants, and amphibians. Therefore, all composites used in this paper are metal-free. Graphite, carbon fibers and nanotubes, minerals, and ceramics are potential replacements for metals in friction materials.

A unidirectional fiber-reinforced composite was used in the analysis of the effect of material anisotropy on thermal-mechanical instabilities. The composites are made up of matrix and fibers. The fibers are embedded in the matrix to give the composite additional strength, hence the term ‘reinforced’. Meanwhile, Jiaxin Zhao et al. [80] and Yi [81] found that the implementation of the stated metal replacement materials may introduce operational safety issues. For example, in brakes, clutches, and seals/bearings, a disturbance in the contact pressure can change the rate of frictional heating, altering the thermal stresses and pressure distribution. In addition, isotropic material properties were an assumption in prior research. Moreover, friction linings usually have anisotropic stiffness and thermal conductivity resulting from the compression of materials during manufacturing. The strength of the composite without being explicit is determined by a few factors such as the fiber arrangement, the fiber’s aspect ratio (l/d), fiber volume fraction, and the fiber catenary. Hockin H. K. Xu et al. [82] discovered for volume fraction values above about 60-70% (depending on the way in which the fibers pack together), tensile stiffness may continue to increase, the laminate's strength will reach a peak and then begin to decrease due to the lack of sufficient resin to hold the fibers together properly. Ciprian et al. [83] extended the work and concluded that the stiffness and strength of a laminate will increase in proportion to the amount of fiber present, but, when the number of fibers in a composite material is too large, the composite’s ultimate strength will degrade.

Oladele et al., [84] used cow fiber-reinforced composite as an alternative to metallic friction material and proved to have very high wear resistance, particularly, from 2 to 10 wt%. This may be due to the presence of fiber as reinforcements in appropriate proportions within the composites (optimum range). Zuo et al. [85] experimentally showed that for a C/C composite in which pyrolytic carbon is not a representatively rough laminar, the wear loss of the composite increases and stability improves with increasing the fiber volume fraction, but when the fiber volume fraction exceeds 30%, the increase of wear loss is very distinct. Also, Zuo et al. [85] found that under the same braking pressure fiber volume fraction does not have an obvious influence on the friction coefficient. For this study, the material chosen for the analysis is a carbon reinforced carbon silicon carbide (C-C/SiC) which is commonly used in high performance cars and a viable substitute to the commonly mass produced metallic (cast iron) counterpart due to reasons concluded and explained through experiments and research conducted by Krenkel [35].

The material properties, albeit, obtained from literature used micromechanics to calculate the properties of the composite material. Micromechanics is the widely used basis in determining a composite material property. There are different methods of micromechanics utilized today from the analytical methods (e.g., rule of mixture, Mori-Tanaka etc.) to the computational (FEM method) method. The purpose of micromechanics is to account explicitly for a material's heterogeneous microstructure while allowing it to be treated as an effective (pseudo-homogeneous) continuum at a higher length scale (e.g., within a structure). To account for this microstructure, micromechanics relies on either a representative volume element (RVE) or a repeating unit cell (RUC). An RVE is a volume of a material whose effective behavior is representative of the material as a whole. Equally important is the concept of a repeating unit cell (RUC). Here, the heterogeneous microstructure is approximated as periodic, where the RUC as the name suggests is the volume of the material that repeats itself to generate the overall microstructure. For better understanding and further studying of micromechanics see Aboudi et al. [86]. Thermal-mechanical instabilities consists of thermoelastic instability (TEI) and thermal buckling. When two surfaces are in contact and sliding against each other heat is generated which is known as frictional heat. The heat also brings about a temperature differential due to the interfacial contact area and exposed surfaces. Barber [21] describes TEI as the instability which results from the interaction of frictional heat generation, thermoelastic distortion and elastic contact is known as frictionally excited thermoelastic instability or better known TEI. Thermoelastic instabilities can be found numerically by perturbed load (non-uniform temperature or pressure) between the two bodies in contact, if the perturbation speed exceeds a certain threshold, then it can be concluded that TEI occurred.

4.2 METHOD

A study of the anisotropic property of a fiber-reinforced composite is conducted using Abaqus, and a MATLAB-based program Hotspotter for numerical analysis of thermal buckling and thermoelastic instability (TEI) respectively. Hotspotter is an engineering analysis software to determine the susceptibility of disc brakes, clutches, or other frictionally sliding systems to thermoelastic instability. Both thermal buckling and TEI simulation were conducted with unidirectional fiber orientation.

The generalized stress-strain relation is shown in equation 4.1, where $\mathrm{C}_{\mathrm{ijkl}}$ is the stiffness tensor.

$$\sigma_{ij} = C_{ijkl}(\varepsilon_{kl} - \alpha_{kl}\Delta T) \tag{4.1}$$

And the inverted stress-strain relation is shown in equation 4.2, where $\mathrm{S}_{\mathrm{ijkl}}$ is the compliance tensor. $[\mathrm{S}] = [\mathrm{C}]'$ and vice versa.

$$\varepsilon_{ij} = S_{ijkl}\sigma_{kl} + \alpha_{ij}\Delta T \tag{4.2}$$

Further, the components of both the stiffness and compliance tensor are 3x3x3x3=81, which is further reduced to 21 components which constitutes the components in the upper triangle of [C] because of these symmetries $\mathrm{C}_{\mathrm{ijkl}} = \mathrm{C}_{\mathrm{klij}} = \mathrm{C}_{\mathrm{jikl}} = \mathrm{C}_{\mathrm{ijlk}}$

$$\begin{bmatrix}\sigma_{11}\\ \sigma_{22}\\ \sigma_{33}\\ \sigma_{12}\\ \sigma_{13}\\ \sigma_{23}\end{bmatrix}=\begin{bmatrix}C_{11} & C_{12} & C_{13} & C_{14} & C_{15} & C_{16}\\ C_{21} & C_{22} & C_{23} & C_{24} & C_{25} & C_{26}\\ C_{31} & C_{32} & C_{33} & C_{34} & C_{35} & C_{36}\\ C_{41} & C_{42} & C_{43} & C_{44} & C_{45} & C_{46}\\ C_{51} & C_{52} & C_{53} & C_{54} & C_{55} & C_{56}\\ C_{61} & C_{62} & C_{63} & C_{64} & C_{65} & C_{66}\end{bmatrix}\left(\begin{bmatrix}\varepsilon_{11}\\ \varepsilon_{22}\\ \varepsilon_{33}\\ \varepsilon_{12}\\ \varepsilon_{13}\\ \varepsilon_{23}\end{bmatrix}-\begin{bmatrix}\alpha_{11}\\ \alpha_{22}\\ \alpha_{33}\\ \alpha_{12}\\ \alpha_{13}\\ \alpha_{23}\end{bmatrix}\Delta T\right) \qquad 4.3$$

The resulting stress-strain relation due to the symmetric conditions is expressed in equation 4.3, where $[\,]_{11}=1,[\,]_{22}=2,[\,]_{33}=3,[\,]_{12}=4,[\,]_{13}=5,[\,]_{23}=6$. Therefore, the fourth-order tensor stiffness and compliance matrix can be rewritten from $\mathrm{C}_{1111}=\mathrm{C}_{11},\mathrm{C}_{1112}=\mathrm{C}_{14}$. This paper focuses on transverse isotropic composite material, which reduces the generalized stress-strain relation to 9 components (equation 4.4) by changing the stiffness tensor matrix. This

$$\begin{bmatrix}\sigma_{11}\\ \sigma_{22}\\ \sigma_{33}\\ \sigma_{12}\\ \sigma_{13}\\ \sigma_{23}\end{bmatrix}=\begin{bmatrix}C_{11} & C_{12} & C_{13} & 0 & 0 & 0\\ C_{21} & C_{22} & C_{23} & 0 & 0 & 0\\ C_{31} & C_{32} & C_{33} & 0 & 0 & 0\\ 0 & 0 & 0 & C_{44} & 0 & 0\\ 0 & 0 & 0 & 0 & C_{55} & 0\\ 0 & 0 & 0 & 0 & 0 & C_{66}\end{bmatrix}\left(\begin{bmatrix}\varepsilon_{11}\\ \varepsilon_{22}\\ \varepsilon_{33}\\ \varepsilon_{12}\\ \varepsilon_{13}\\ \varepsilon_{23}\end{bmatrix}-\begin{bmatrix}\alpha_{11}\\ \alpha_{22}\\ \alpha_{33}\\ 0\\ 0\\ 0\end{bmatrix}\Delta T\right) \qquad 4.4$$

can further be expressed in terms of five independent constants which are known as the engineering constants. For the derivation of a transverse isotropic stiffness matrix, see Aboudi et al. [87]. Equation 4.2 can be written in matrix form, in terms of elastic constants E, ν, and G (equation 4.5).

$$\begin{bmatrix}\varepsilon_{11}\\ \varepsilon_{22}\\ \varepsilon_{33}\\ \varepsilon_{12}\\ \varepsilon_{13}\\ \varepsilon_{23}\end{bmatrix}=\begin{bmatrix}{}^{1}/_{E_1} & -{}^{\nu_{21}}/_{E_2} & -{}^{\nu_{31}}/_{E_3} & 0 & 0 & 0\\ -{}^{\nu_{12}}/_{E_1} & {}^{1}/_{E_2} & -{}^{\nu_{32}}/_{E_3} & 0 & 0 & 0\\ -{}^{\nu_{13}}/_{E_1} & -{}^{\nu_{23}}/_{E_2} & {}^{1}/_{E_3} & 0 & 0 & 0\\ 0 & 0 & 0 & {}^{1}/_{2G_{23}} & 0 & 0\\ 0 & 0 & 0 & 0 & {}^{1}/_{2G_{13}} & 0\\ 0 & 0 & 0 & 0 & 0 & {}^{1}/_{2G_{12}}\end{bmatrix}\begin{bmatrix}\sigma_{11}\\ \sigma_{22}\\ \sigma_{33}\\ \sigma_{12}\\ \sigma_{13}\\ \sigma_{23}\end{bmatrix}+\begin{bmatrix}\alpha_{11}\\ \alpha_{22}\\ \alpha_{33}\\ \alpha_{12}\\ \alpha_{13}\\ \alpha_{23}\end{bmatrix}\Delta T \qquad 4.5$$

The reinforced fibers in this chapter are considered to be oriented parallel to the applied force in the z-direction (along the thickness). Therefore, the plane of isotropy is the r (radial) – t (theta) plane (1 – 2 plane). Hence, $C_{11} = C_{22}$, $C_{44} = C_{55}$, and due to the symmetry in the matrix $C_{12} = C_{21}$, $C_{13} = C_{31}$, and $C_{23} = C_{32}$. Also, in Eq. 4.5, $E_1 = E_2, \nu_{12} = \nu_{21}, \nu_{13} = \nu_{23}, \nu_{31} = \nu_{32}$, $G_{13} = G_{23}$. Therefore, the five engineering constants for transverse isotropy are $E_1, E_3, \nu_{12}, \nu_{31}$, and G_{23}. The relation between the stiffness matrix components and the engineering constants are:

$$C_{11} = C_{22} = E_1(1 - \nu_{23}\nu_{32})\Upsilon \quad C_{33} = E_3(1 - \nu_{12}\nu_{21})\Upsilon \quad C_{12} = E_1(\nu_{21} - \nu_{23}\nu_{31})\Upsilon$$

$$C_{13} = C_{23} = E_1(\nu_{13} - \nu_{12}\nu_{32})\Upsilon \quad C_{66} = 2G_{12} = E_1/(1 + \nu_{12}) \quad C_{44} = C_{55} = 2G_{23}.$$

Where, $\Upsilon = \frac{1}{1-\nu_{12}\nu_{21}-2\nu_{13}\nu_{31}-2\nu_{12}\nu_{13}\nu_{32}}$

The Poisson's ratio $\nu_{13} \neq \nu_{31}$, but the ratio $\nu_{13}/E_1 = \nu_{31}/E_3$ in equation 4.5 therefore, $\nu_{31} = \frac{\nu_{13}}{E_1} E_3$.

Silicon carbide is commonly used in nonmetallic friction materials, especially in brake applications. Therefore, the chosen fiber-reinforced composite for the analysis in this paper is a multiphase composite of carbon-reinforced carbon-silicon carbide (C-C/SiC), where the matrix is a mixture of carbon and silicon carbide with a non-unity carbon to silicon carbide ration and a 5% porosity. Table 4.1 shows the material properties of the C-C/SiC composite relevant for both the TEI and thermal buckling simulation. The composite material exhibits transverse isotropy and has a varying fiber volume of 40% - 50%. The properties of the composite was determined via experiment and reported by Krenkel [35] and corroborated by Pardini & Gregori [88] using Reuss and Voight methods.

Table 4.1: Material properties of carbon-carbon/silicon carbide (C-C/SiC) composite

	Value		
Carbon fiber volume (%)	40	45	50
C/SiC matrix ratio	65/35	60/40	55/45
	Elastic modulus (GPa)		
E_{11}	36	35	33
E_{22}	36	35	33
E_{33}	141	156	167
	Shear modulus (GPa)		
G_{12}	20	21	21
G_{13}	14	14	13
G_{23}	14	14	13
	Poisson's ratio		
ν_{12}	0.18	0.18	0.18
ν_{13}	0.25	0.25	0.25
ν_{23}	0.25	0.25	0.25
Density, ρ (kg/m^3)	2060	2100	2140
	Thermal conductivity (W/m. K)		
k_{11}	35	30	25
k_{22}	35	30	25
k_{33}	57	50	45
	Coefficient of thermal expansion, α (10^{-6}/°C)		
α_{11}	0.68	0.34	0.63
α_{22}	0.68	0.34	0.63
α_{33}	0.12	0.70	1.05

4.2.1 THERMOELASTIC INSTABILITY (TEI)

Thermoelastic instabilities occur if the perturbation speed exceeds a certain threshold. This threshold is known as the critical sliding speed. The critical speed is then determined by searching for the lowest speed at which at least one mode has a positive growth rate. The exponential growth rate of eigenmodes of the system for a given rotational speed is determined by an eigenvalue method. Hotspotter is utilized in finding the critical sliding speed, which uses an axisymmetric model for the finite element simulation. It treats axisymmetric systems using Fourier series in the circumferential direction and hence involves modeling the cross-section of the model. User input to the program includes the geometric shape of all the components, the relevant material (thermal and elastic) properties, the coefficient of friction, and the boundary conditions at both internal and external surfaces. Output from the program includes the exponential growth rate and migration speed of the eigenmode for specified sliding speed, the critical speed as a function of wavenumber (number of hot spots around the circumference), and the spatial form of the dominant eigenmode in both the plane of the discs and the cross-sectional plane. During the onset of TEI, there is an instant when the perturbation becomes unstable and renders the system unstable. The instability and stability of the system can be inferred from the plot of the critical speed as a function of wavenumber (number of hot spots around the circumference) output described by Lee & Barber [63], which is the region above and below the graphical curve respectively.

Figure 4.1 shows the finite element models used in the TEI simulations. The disc for the clutch setup has dimensions of 125mm, 86mm, and 3mm, for the outer radius, inner radius, and thickness respectively and the friction disc has a thickness of 4mm and the same radii dimensions as the clutch disc. Layer 1 and layer 2 in Figure 4.1 represents the friction and steel disc respectively. The boundary condition of the axisymmetric clutch model at the left edge (inner diameter) is fixed in all translation direction but free to rotate about the Z-axis at 630rad/s (approximately 6,000rpm because most cars redline at 6,000 rpm to prevent engine braking), at the right edge (outer diameter) is free, the top edge has an anti-symmetric boundary condition, and the bottom edge has a symmetric boundary condition. For the brake model, the inner radius of the brake rotor has the same boundary condition as the clutch disc, but rotating about the Z-axis at 50rad/s. While the pad and backing plate are fixed in all directions while in contact with the brake rotor.

The symmetric boundary condition means that the system is mechanically symmetric and thermally insulated (Uz = 0; Szr = Szt = 0; Qz = 0) while the anti-symmetric means that it is mechanically antisymmetric and thermally insulated (Ur = Ut = 0; Szz = 0; T = 0), where T, Qz, Uz, Ur, Ut, Szz, Szr, and Szt represents temperature, heat flux in the axial (Z) direction, translational displacements in the axial, radial and circumferential directions, the stress in the axial direction and shear stresses axial-radial plane and axial-circumferential plane respectively.

In Hotspotter, the anisotropic material properties are specified using the format in equation 4.5. The brake model is a benchmark model obtained from Hotspotter and modified for this paper. The brake rotor is made of cast iron, the pad backing plate steel, and the pads C-C/SiC composite. Due to the current limitation of Hotspotter, thermal conductivity can only be specified as isotropic. Therefore, in order to determine the effect of anisotropic thermal conductivity, the average of the anisotropic thermal conductivity was taken, which was also done when doubling or halving the anisotropic conductivity for the TEI simulation. The 2D axisymmetric model in Figure 4.1a shows a biased mesh at the interface where the meshes was biased toward the sliding interfaces to account for the large temperature gradients. This is done to accurately capture the temperature distribution by discretizing interface surface to small elements and eliminate any errors in numerical results.

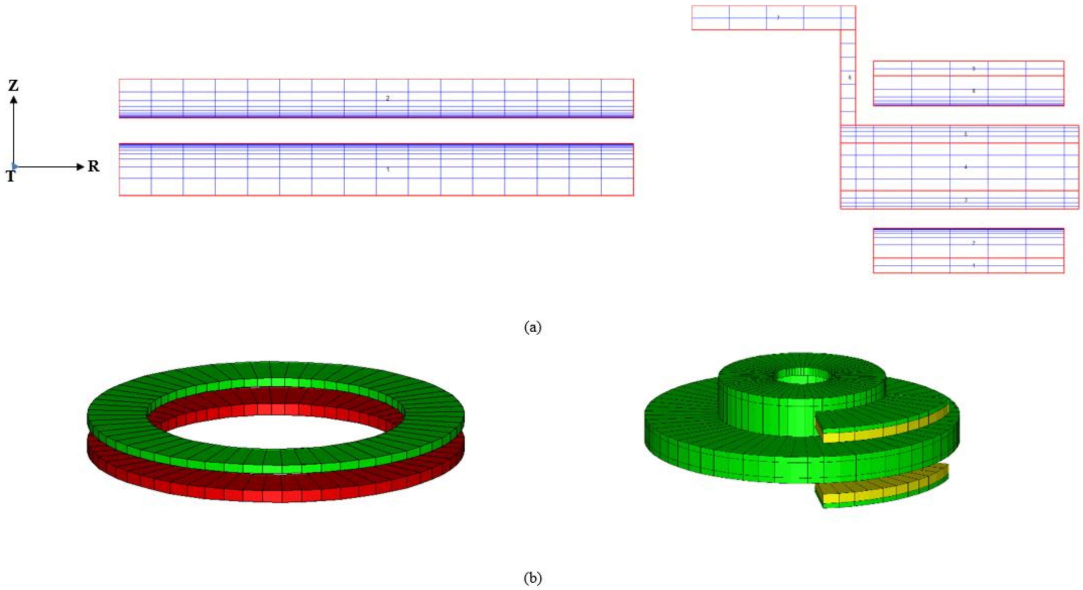

(a)

(b)

Figure 4.1: TEI finite element setup a) axisymmetric clutch and 2D brake model; b) 3D clutch and brake model

4.2.2 THERMAL BUCKLING

Thermal buckling occurs when the working temperature of the structure exceeds the critical buckling temperature. The critical buckling temperature is calculated as the product of the maximum nodal temperature and the first eigenvalue. In an eigenvalue solution, the most dominant mode is the first mode (eigenvalue). Therefore, for thermal buckling to occur, the working temperature must exceed the critical buckling temperature. During braking or gear changes, the temperature gradient along the radius of the rotor or clutch plate is commonly found to have a linear profile.

Equation 4.6 is the governing equation defining the eigenvalue problem of buckling.

$$\left([K] + \lambda_{cr}[K_{\sigma}]_{ref}\right)\{\delta D\} = \{0\} \tag{4.6}$$

Where, "ref" represents the reference load, i.e., a load that is first applied to the structure to find the reference stress stiffness matrix, $[K_{\sigma}]_{ref}$. Another load $\{R\} = \lambda_{cr}\{R\}_{ref}$ will then be applied to the structure, where λ_{cr} represents an arbitrary multiplier to the original reference load. The boundary conditions for the thermal buckling analysis changes depending on the model. The boundary condition for the brake rotor is a prescribed displacement on the inner radius via a multipoint constraint, where all translational displacement, rotational displacement about the radial and circumferential axis is zero (Ur = Ut = Uz = URr = URz = 0) but is free to rotate about the z axis (URt ≠ 0). While the clutch disc has similar boundary condition with the brake model, it differs by having a free translational displacement in the z direction (Ur = Ut = URr = URz = 0; Uz = URt ≠ 0) which is applied to the inner nodes via a multipoint constraint function to a reference point node at the center of the model. The clutch disc has dimensions of 125mm, 86mm, and 3mm, for outer radius, inner radius, and thickness respectively. A linear, sinusoidal, and exponential temperature profiles are common surface temperature profiles along the radius of a disc after sliding contact with another surface. Although these profiles are common, the highest temperature experienced in a brake disc is dependent on several factors such as braking force, coefficient of friction, time of applied brake, number of consecutive brakes etc. These factors were studied by Belhocine & Bouchetara [89] with three types of cast iron brake rotor and found an average temperature of 250°C through a disc thickness. While, Abdullah & Schlattmann [90] and Faidh-Allah [91] extended the effect of such factors to clutches and found the surface of the clutch resulted in a linear temperature profile distributed along the radius of the clutch after engagement with the temperature of 315°C at the inner radius and 345°C at the outer radius. Shaahu et al. [16] and Yi et al. [13] extended the work to explain the linear profile and found that a linear temperature profile can be caused by the sliding speed as a linear function of the radius and by the fact that the frictional heat generation rate is a linear function of the sliding speed. Therefore, the thermal buckling analysis of the brake rotor is simulated with a prescribed linear temperature along the radius having a maximum temperature of 250°C and a minimum of 25°C (room temperature), while the clutch has a linear temperature profile along the radius ranging from 315°C to 345°C (inner radius to outer radius). Figure 4.2 shows the finite element model of the clutch disc and brake rotor used in the thermal buckling analysis which is a vented brake rotor.

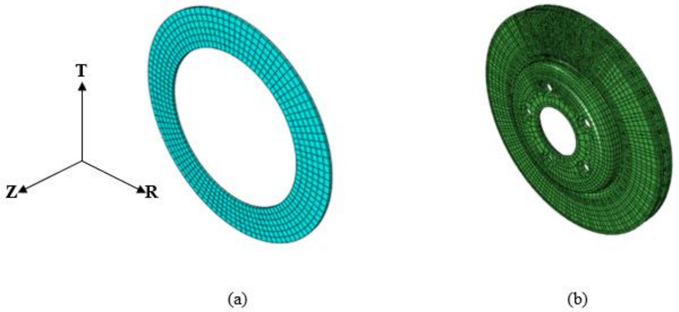

Figure 4.2: Thermal buckling finite element setup a) 3D clutch disc, b) 3D brake rotor

The dimension of the clutch disc is the same as that in the TEI simulation, and the dimension of the brake rotor axle radius, hat radius, outer radius, disc thickness and hat height is 32mm, 92mm, 148mm, 20mm and 10mm respectively.

4.3 RESULT

A buckling analysis was conducted with some common current metal-free composite material in Table 4.2 The carbon fiber volume used in the mixture was 60%. All the composites have an isotropic matrix and are reinforced with carbon fiber. The properties of the composites were calculated using the rule of mixtures. The material properties of the constituent material were obtained from CES EduPack [92] shown in Table 5.1.

Table 4.2: Critical buckling temperature with common metal-free fiber-reinforced composite

Composite Material	Buckling Temperature (°C)
Carbon-Graphite	1269
Carbon-Carbon	4375

Figure 4.3 shows the relationship between carbon fiber volume and critical sliding speed of a (a) clutch disc and (b) brake rotor. An increase in fiber volume ratio by 0.05 decreases the maximum critical sliding speed by a factor of approximately 1.2 in a clutch disc and increased the maximum critical sliding speed by a factor of 4 in a brake rotor. While an increase in fiber volume ratio by 0.1 decreases the maximum sliding speed in a clutch disc by a factor of 1.3 and increases the maximum critical sliding speed in a brake rotor by a factor of 5. After visual inspection of Figure 4.3b it is seen that a composition with 40% fiber volume has a smaller area (stable region) under the curve which translates to a likely chance of susceptibility to TEI compared to a composition with fiber volume of 45% and 50%. The critical sliding speed of the clutch setup with a friction disc thickness of 4mm has a magnitude of a hundred rpm and the critical sliding speed of the

brake setup with a friction pad thickness of 10mm has a magnitude of one million rpm which agrees with Hartsock & Fash [93] finding, that the thickness of the friction material influences the critical sliding speed.

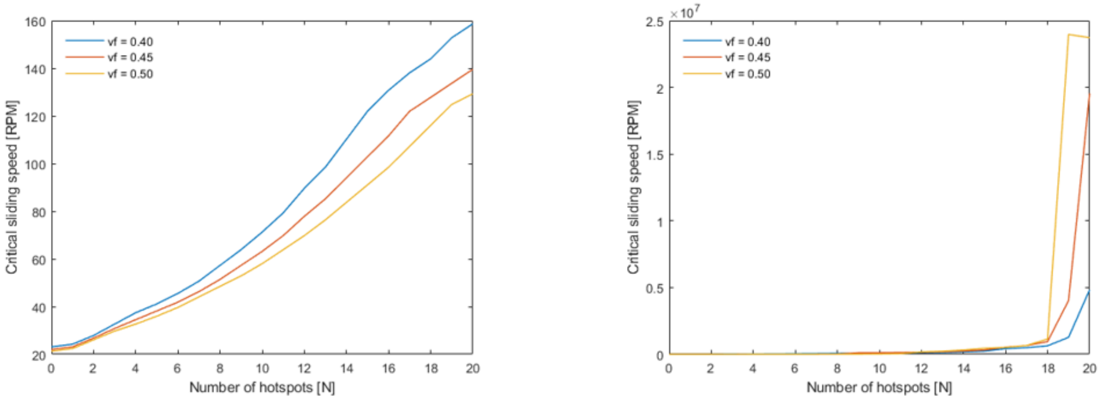

(a) (b)

Figure 4.3: Effect of fiber volume on TEI a) clutch disc; b) brake rotor

Table 4.3 shows the effect of carbon fiber volume on thermal buckling. Increasing the fiber volume from 40% to 45% increases the buckling temperature but lowers between 45% and 50% fiber volume. This decrease in buckling temperature can be a result of the fiber packing and the matrix volume between neighboring fibers in the composite, because an increase in the fiber volume ratio decreases the matrix volume between fibers and the overall matrix volume ratio, which can affect the buckling temperature.

Table 4.3: Effect of fiber volume on thermal buckling

Fiber volume (%)	Buckling temperature (°C)	
	Brake	Clutch
40	915.83	344.58
45	1868.1	723.67
50	1016.8	409.55

Figure 4.4 shows four plots of the effect of material properties on the buckling temperature of a brake rotor. From observation, it shows that increasing either the radial or circumferential elastic modulus reduces the buckling temperature, while increasing the axial elastic modulus increases the buckling temperature. The relationship between the elastic modulus and buckling temperature is evidently not a linear relation but has an exponential decay relationship between the radial or circumferential elastic modulus and the buckling temperature; and a logarithmic increase function relationship between the axial elastic modulus and buckling temperature. This suggests that past a certain value of either the radial, circumferential, or axial modulus of elasticity there would be no change to the buckling temperature. The lack of effect by the axial coefficient of thermal expansion (CTE) on thermal buckling can be due to the uniform temperature distribution across the thickness which was stated in the method as having a linear temperature distribution only in the radial direction. Both increase in either radial or circumferential CTE decreases the buckling temperature in a pattern similar to a decreasing quadratic function.

The effect of Poisson's ratio is greater than the effect of thermal conductivity and axial CTE but less compared to the effect of moduli and radial and circumferential CTE. An expanded view of the effect of Poisson's ratio is shown to better visualize the trend. The relationship between the Poisson's ratio and buckling temperature is linear with a change of approximately 20°C for a Poisson's ratio value range of 0.15 to 0.26, where increasing the value of either ν_{13}or ν_{23} increases the buckling temperature and increasing ν_{12} decreases the buckling temperature. In Figure 4.4 and Figure 4.5 E, CTE, nu, k, r, c, and z represent modulus of elasticity, coefficient of thermal expansion, Poisson’s ratio, thermal conductivity, radial, circumferential, and axial respectively.

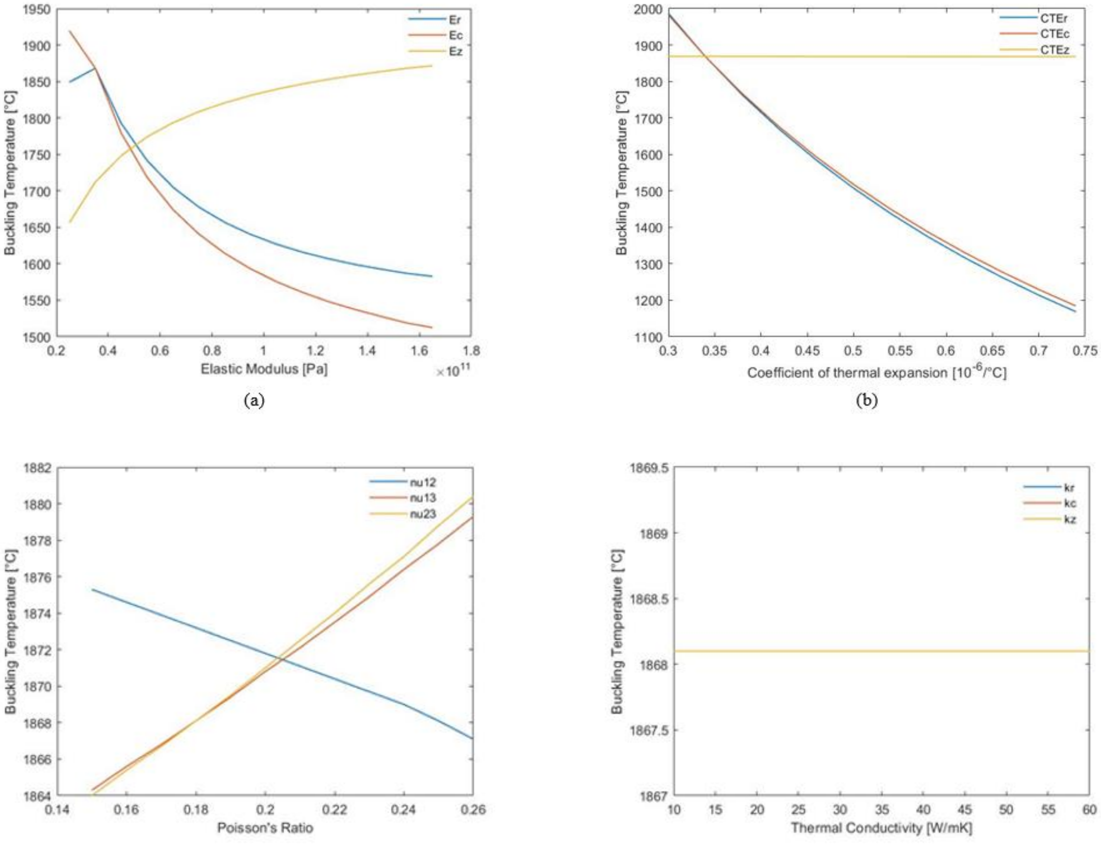

(a) (b)

(c) (d)

Figure 4.4: Plot of the effect of anisotropic material properties a) Elastic modulus, b) coefficient of thermal expansion, c) Poisson’s ratio, and d) thermal conductivity on buckling temperature of a brake rotor

Thermal conductivity has no effect on thermal buckling. Hence the horizontal line in the labeled ‘d’ plots in Figure 4.4 and Figure 4.5. Figure 4.5 have graphical plots showing the effect of material properties on the buckling temperature of a clutch disc. The results of the effect of the anisotropic material properties on buckling for a clutch disc are slightly similar to that of a brake rotor except in instances of the axial modulus of elasticity, Poisson’s ration, radial and circumferential CTE.

An increase of either the radial or circumferential modulus of elasticity reduces the buckling temperature, but no change occurs in the buckling temperature with a change in the axial modulus of elasticity, which can be a result of the constant temperature along the thickness and its relatively small thickness comparatively to the brake rotor's thickness.

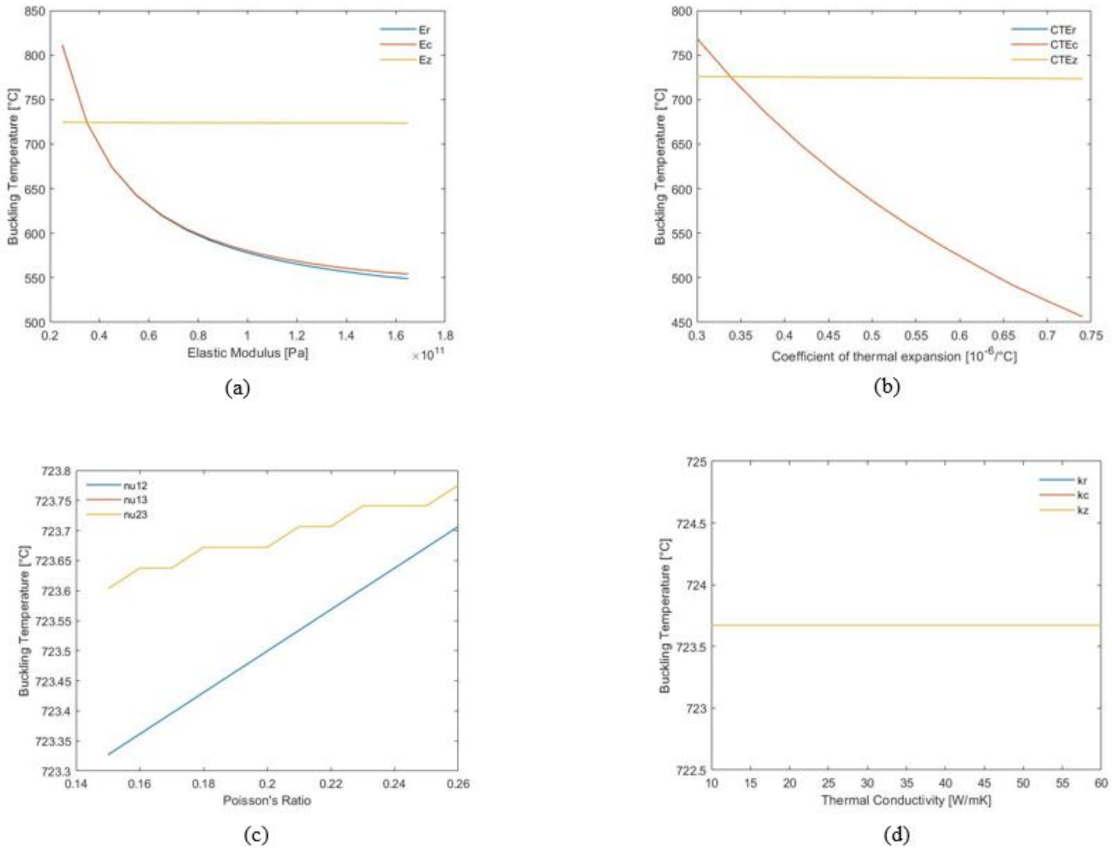

Figure 4.5: Plot of the effect of anisotropic material properties a) Elastic modulus, b) coefficient of thermal expansion, c) Poisson's ratio, and d) thermal conductivity on buckling temperature of a clutch disc

Both radial and circumferential CTE have the same effect on the thermal buckling for the clutch disc. This equality in result can be a result of the geometry, because same equality is not experienced in the brake rotor which has a larger thickness than the clutch disc. Unlike in a brake rotor, the Poisson's ratio has a minimal effect on thermal buckling with a buckling temperature change of approximately 0.4°C.

Figure 4.6 shows graphical representation of the effect of anisotropy in critical sliding speed and occurrence of TEI. They plots are a relationship between critical sliding speed and number of hotspots (N) (or mode of deformation) of a clutch disc. The axial (referenced as Z in Figure 4.1 axis) elastic modulus has a greater effect on the critical sliding speed compared to the other elastic moduli. An increase of the circumferential elastic modulus has an inverted response to the sliding speed. Also, an increase in the any thermal conductivity increases the critical sliding speed. The effect of thermal conductivity experienced in this analysis corresponds with the closed form solution derived by Lee & Barber [63] where the half planes are rigid non-conductors shown in equations 4.7 & 4.8. Although the models are different from the model that produced equation 4.7 & 4.8, it can be used as a guide into deriving and understanding the effects a non-homogenous material has on sliding speeds.

$$V_s^* = \frac{fV_s(1+\nu)\alpha\mu a}{(1-\nu)K} = \frac{Asinh(2A)tanh\,(A)}{sinh(2A)+2A} \qquad 4.7$$

$$V_A^* = \frac{fV_A(1+\nu)\alpha\mu a}{(1-\nu)K} = \frac{Asinh(2A)coth\,(A)}{sinh(2A)-2A} \qquad 4.8$$

Where $\mathrm{V_s}$, $\mathrm{V_A}$ are critical sliding speeds for symmetric and antisymmetric modes respectively, ν, α, μ, K and $A = ma$ are Poisson's ratio, CTE, modulus of rigidity, thermal conductivity, and dimensionless half-layer thickness respectively.

Coefficient of thermal expansion has minimal effect in the critical sliding speed in TEI. Which is shown as closely aligned lines in the plot for Figure 4.2b with varying

CTE. The legends in Figure 4.6 and Figure 4.7 refer to how the anisotropic material properties were varied, where r, t, and z refer to radial, circumferential, and axial respectively, and the values 2 and 0.5 refer to double and half the respective material property. As an example, 2Ez represents the radial elastic modulus increased by a factor of approximately 2. Although, there are 8 legends and 5 lines shown in Figure 4.6d, this is because some of the lines overlap for instance a decrease by half of circumferential thermal conductivity is the same as the result for a decrease of axial thermal conductivity by half. The fibers are considered aligned in the axial (Z) direction and the results show that the properties in the direction parallel to the applied load have more effect in thermoelastic instability. The alignment of the fiber in correlation to the model axis does affect the critical sliding speed.

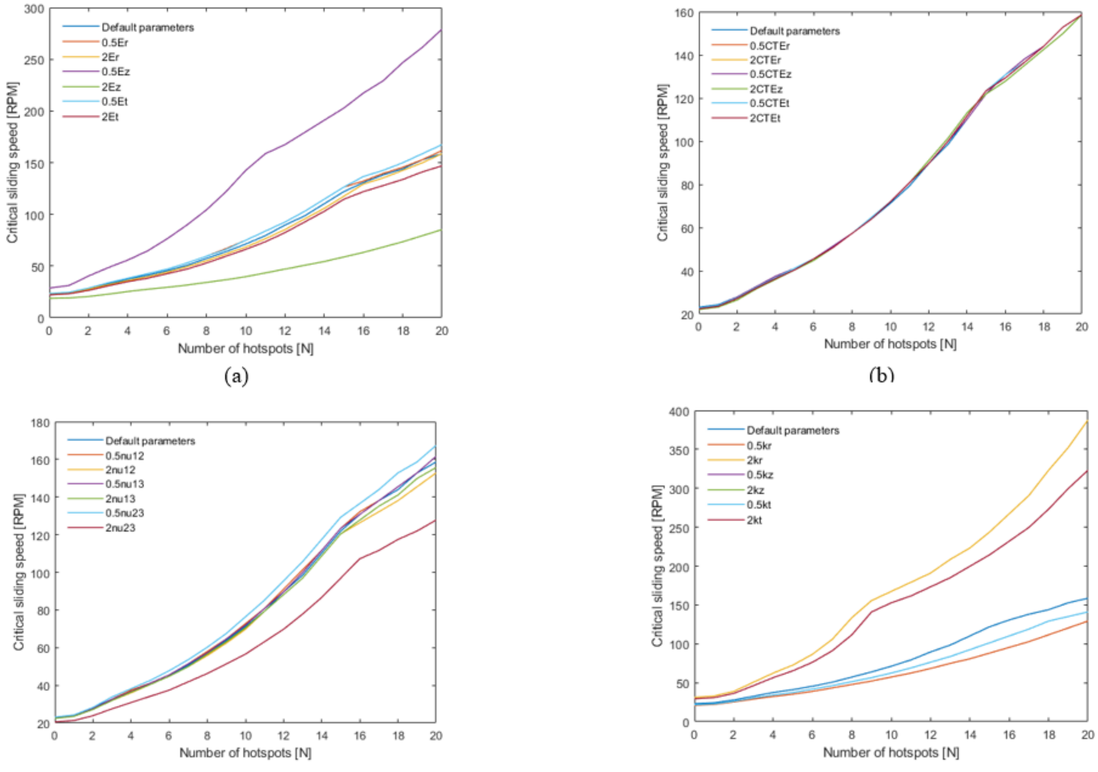

(a) (b)

(c) (d)

Figure 4.6: Critical sliding speed vs hotspot number of a clutch disc for a) varied elastic modulus; b) varied coefficient of thermal expansion; c) varied Poisson's ratio; d) varied thermal conductivity.

Figure 4.7 are plots of critical sliding speed against the number of hotspots (N) of a brake rotor while varying the anisotropic material properties. Unlike the clutch disc, the critical sliding speed of a brake rotor is in the magnitude of millions. This is due to the pad geometry, contact area, thickness of 10mm compared to 4mm of the friction disc of the clutch system and the brake rotor thickness. In a brake rotor with the current geometry, thermal conductivity has a greater positive effect on the critical sliding speed producing the highest critical sliding speed and doubling the axial modulus of elasticity produces the lowest critical sliding speed.

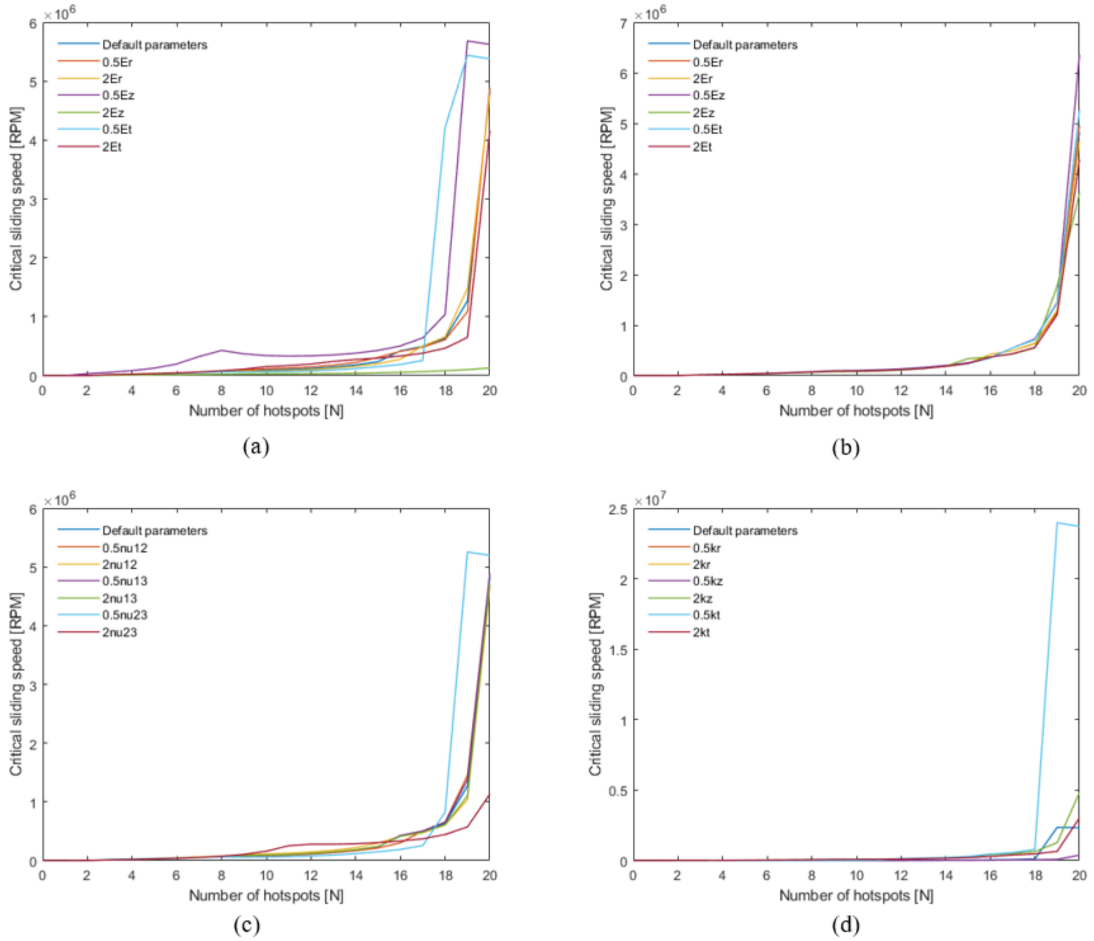
(a)
(b)
(c)
(d)

Figure 4.7: Critical sliding speed vs hotspot number of a brake rotor for a) varied elastic modulus; b) varied coefficient of thermal expansion; c) varied Poisson's ratio; d) varied thermal conductivity.

Another output in addition to the stated outputs from Hotspotter is temperature distribution as a result of frictional heat generation. The temperature distribution (surface and cross-section) for first deformation mode of the clutch disc with doubled axial elastic modulus as a sample is shown in Figure 4.8. Depending on the material composition the number of hotspots is different for the first mode deformation. The number of hotspots (N) present for the first mode deformation of the previously stated configuration is four

(N = 4). The first mode represents the dominant mode for which it has a positive growth rate at the lowest speed. Figure 4.9 shows the deformation of the brake rotor corresponding to the first non-negative eigenvalue (first mode) in the thermal buckling analysis which is also known as the coning mode due to the resemblance of a cone.

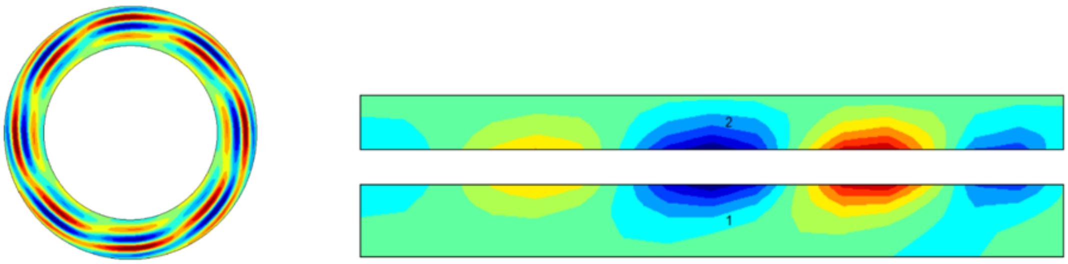

(a) (b)

Figure 4.8: Temperature distribution of the a) Surface and b) Cross-section corresponding to the first mode deformation.

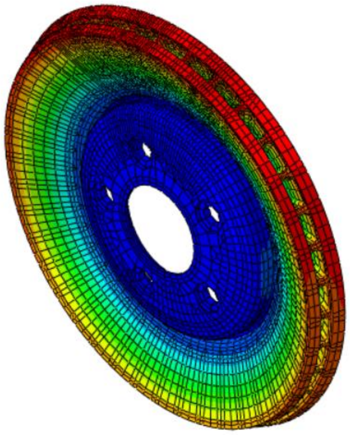

Figure 4.9: Deformed brake rotor corresponding to the first non-negative eigenmode.

4.4 CONCLUSION

The following conclusions were reached from a parametric study that was conducted computationally using ABAQUS and Hotspotter to investigate the dominant anisotropic parameter that affects thermal-mechanical instabilities (TMI) of non-metallic friction material of clutches and brakes. The properties in the direction perpendicular to the sliding direction tend to have significant effect on the sliding speed. Coefficient of thermal expansion has little effect on TEI, and thermal conductivity has no effect on thermal buckling. Uniform temperature across the thickness mitigates the effect of coefficient of thermal expansion. Therefore, uniform temperature distribution across the thickness of a disc causes coefficient of thermal expansion to have negligible effect on thermal bucking.

Increasing the radial thermal conductivity has a high positive (increase in critical sliding speed) influence on the onset of TEI and due to the structure of the Hotspotter software and how thermal conductivity is entered, the results from the circumferential and axial increase or decrease of the thermal conductivities is equal. Decreasing the axial elastic modulus resulted in the largest critical sliding speed. While increasing the axial modulus of elasticity or increasing the out-of-plane Poisson's ratio produced the lowest critical sliding speed. Therefore, the axial modulus of elasticity has a greater positive effect on TEI. The radial and circumferential elastic modulus and coefficient of thermal expansion have a significant effect on the buckling temperature in both the clutch disc and brake rotor. Increasing the radial or circumferential modulus of elasticity reduces the buckling temperature and vice versa for the axial modulus of elasticity in a brake rotor.

CHAPTER V

IDEAL COMPOSITION OF C-C/SIC COMPOSITE AND ANISOTROPIC MATERIAL PROPERTIES TO MINIMIZE OCCURRENCE OF THERMAL-MECHANICAL INSTABILITIES IN A CLUTCH DISC

5.1 INTRODUCTION

This chapter proposes a model and method based on FEM micromechanics. The method to generate the RVE utilizes an additional step coined “packing” to describe a manufacture process that the friction material undergoes. The effect of anisotropy on thermal-mechanical instabilities (TMI) have been partially studied in the past years especially focusing on the effect of functionally graded materials (FGMs) on thermoelastic instability (TEI). Where Mao et al. [94] studied the effect of FGM of a half plane sliding against a homogenous half plane, with the FGM graded along the thickness following an exponential function. Although FGMs are anisotropic, the material properties in one direction are dependent on the material properties in the other direction like transverse isotropy which was studied in previously published article and shown that an anisotropic material property independent of the similar property in a different direction does change the result of TMI significantly. Some studies have been done looking into alternative materials for the brake rotor and clutch disc, but this research is focused on the friction material as an anisotropic composite material sliding against a homogenous disc or rotor. A study conducted by Zhao et al. [68] proved how much importance the frictional material properties plays in TEI which stated “that a dominant. TEI deformation mode is strongly dependent on the properties of frictional material”. Material anisotropy is not just affected by fiber volume ratio, but also orientation and aspect ratio. Most published works have focused a great deal of research on fiber volume ratio and very little into the effect of fiber aspect ratio. Qiu [95] , Tawerghi [96] , and D. Zhao [97] studied effect of percolation on material properties and shapes and aspect ratio of inclusions on percolation using a Monte Carlo scheme for generating the inclusions. They studied inclusion shape and orientation on effective material properties, and the work was forwarded by author to anisotropy of material properties but not using a Monte Carlo scheme, which theoretically should not change the way the particles are generated and randomly oriented.

Percolation is a physical hypothetical phenomenon where a minimum number of particles form a network like pathway. This is possible with particle overlap, physically particles in a composite do not overlap, but Y. B. Yi [98] showed that in case of overlap or not involving particulate inclusions of high density the interfacial contact must be considered to reliably predict the relevant transport properties, therefore, if there is overlap or percolation the interfacial contact is already considered and should predict the material properties accurately. Machine learning has become prevalent in the past decade in industries that deal with data, but recently its application has been found beneficial to other industries. Machine learning is “a buzz word” for optimization which has been shown with mathematical expressions to describe the change of parameters to minimize a certain response. The machine learning application has been gradually extended into material science and Markworth & Saunders [99] developed a model for spatial variation of composition of a metal/ceramic FGM and optimized flow of heat through material, where this work was extended by Ootao et al. [100] using a neural network to optimize material compositions for a nonhomogeneous hollow sphere with varied FGM properties. Only after a few years did Na & Kim [101] incorporate optimization of FGM in thermal buckling. Although optimization was incorporated in TMI, all material were considered FGM, whereas an optimization algorithm was incorporated in this chapter to predict the ideal composite material composition that produces the maximum TMI response (buckling temperature and critical sliding speed) in clutches.

5.2 METHOD

A study to optimize the composition of a composite friction material for thermomechanical instabilities is conducted using MATLAB, ABAQUS and Hotspotter. A flow chart (Figure 5.1) shows the methodology progression for this study, where a detailed explanation and insight for each progression will be given in the following subsections.

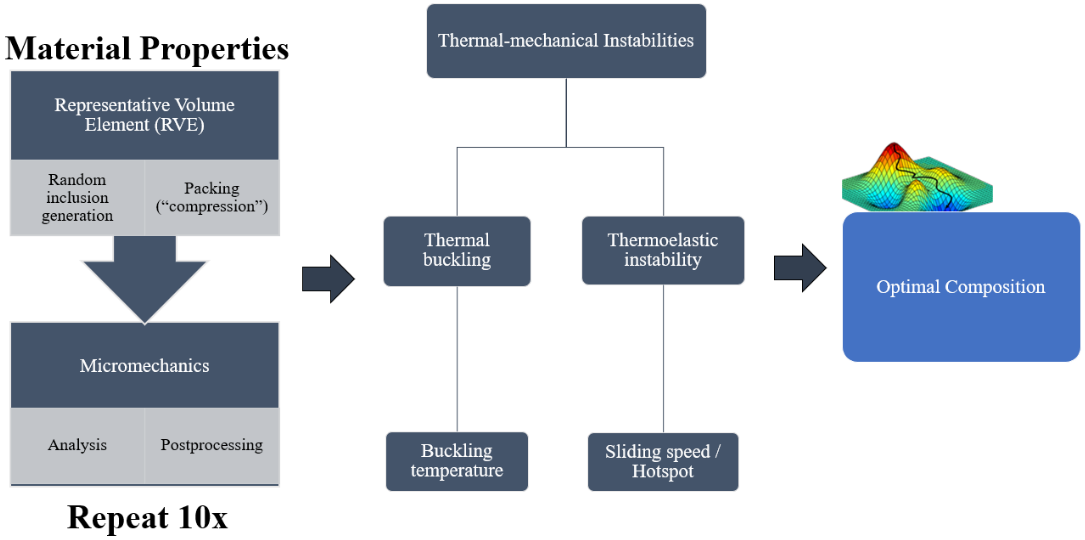

Figure 5.1: Flow chat for research study

5.2.1 MATERIAL PROPERTIES

This subsection is the first step in the flow chart shown in Figure 5.1. This describes the RVE (representative volume element) setup (randomly generated particles and packing) and the calculation of the material properties using micromechanics (FEM model, analysis, and post-processing). The chosen material for study is a carbon-carbon silicon carbide (C-C/SiC). The composite consists of a matrix (carbon), reinforced fiber (carbon) and interface (silicon carbide).

5.2.1.1 MATERIAL SELECTION

The research into alternative materials to common homogenous materials have been mostly led by the aerospace industry in the last generation, especially to achieve lightweight or high heat resistance. This alternative material research has proven beneficial in the field of tribology, especially in brakes and clutches. The aeronautic industry spear-headed the use of composite materials in their brake system, mainly carbon reinforced carbon (C/C) composite which displayed excellent results to its counterpart homogenous materials. Some advantages of C/C composite are it was light weight, higher resistance to heat, low coefficient of thermal expansion, corrosion resistance, and high resistance to wear. The automotive industry took the C/C composite a step further and added silicon carbide to the mix to produce carbon fiber reinforced carbon silicon carbide (C-C/SiC). The addition of silicon carbide increased the composites' heat resistance. Although, it did not dissipate heat very well which affected its coefficient of friction, which is why today most brakes made of C-C/SiC have vents and veins to help dissipate surface heat and keep its coefficient of friction. This research analyzes the different constituents' ratios of the C-C/SiC composite. In the future a proposed mixture to include aramid fiber will be investigated because aramid fiber also displays high resistance to heat, highly abrasiveness, and low wear, which is believed to improve the coefficient of friction and reduce wear to the pads. These are the reasons for the choice of material constituents for the analysis. Table 5.1 shows the material properties of the composite constituents.

Table 5.1: Composite constituents material properties

Property	Carbon matrix	Carbon fiber	Silicon carbide	Unit
Density, ρ	1330	1825	3210	kg/m^3
Elastic modulus, E	13.5	380	448	GPa
Shear modulus, G	5.65	170	191.5	GPa
Poisson's ratio, ν	0.2	0.105	0.17	
CTE, α	0.75	0.3	3.5	$10^{-6}/°C$
Thermal conductivity, k	6.95	140	78	$W/m\mathrm{K}$
Specific heat, Cp	1107.5	710	1040	J/kgK
Tensile strength, TS	6.9	2405	235	MPa

5.2.1.2 REPRESENTATIVE VOLUME ELEMENT

A MATLAB code is written to first generate non-overlapping randomly distributed elliptical particles (inclusions) in a 2D unit cell. A pseudo algorithm for generating the non-overlapping random inclusion in the 2D cell is shown in Figure 5.2. The number of particles in the cell is controlled by volume fraction, size of particle, and size of the cell as shown in equation 5.1.

$$N = \frac{v_f 4LH}{\pi ab} \tag{5.1}$$

Where N, L, H, a, b and v_f represents number of particles, length of cell, height of cell, major and minor diameter of elliptical inclusion, and volume fraction of inclusion respectively.

- Create boundary (cell dimension)

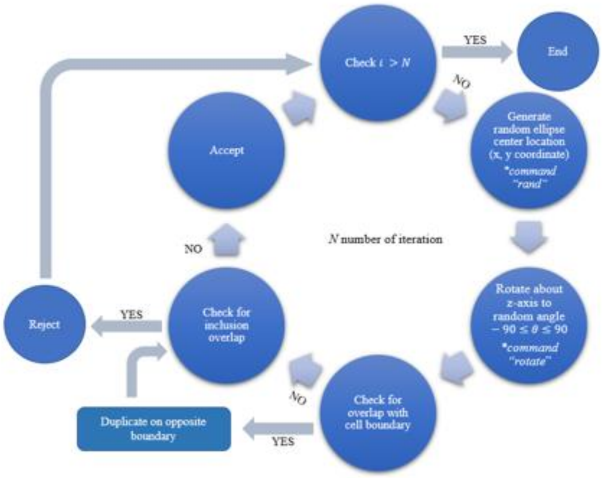

Figure 5.2: Flow chart of the randomly generated inclusion algorithm

Where *i* in the above figure represents the *ith* inclusion and *N* is the number of inclusions estimated using equation 5.1. The major and minor diameter used in equation 5.1 is used to control the aspect ratio of the elliptical inclusion.

As noted by Aboudi et. al., [87] the material properties of a composite with randomly distributed reinforced inclusion tends to be isotropic in nature as the volume fraction of the inclusions increase. The purpose of this study is to look at anisotropic effect, therefore, the model of the composite created in MATLAB requires an additional line of code after the required number of inclusions is reached. This additional step is believed to alter the internal stresses in the RVE and prevent isotropy in the composite. This step is identified as “packing”. The “packing” increases the density (number of inclusions per unit length) of the particles in a specific direction to introduce percolation. The “packing” of the inclusions is a process that mimics a vital production step in the production process of a brake pad which is the compression stage. The mixture for the brake pad is compressed and heated to compact the materials and create adhesion between each constituent, hence, the model follows a compression stage which reduces the cell by half in the y-direction resulting in a 1 x 1/2 cell. The particles are not generated in the new cell because that would change the number of particles and create isotropy in the material. A simplified form to creating this “packing” in the new RVE the y-coordinate values for the particles are multiplied by 0.5, which is intended to keep the relative position to other inclusions and the boundary the same. Additionally, the new orientations of the inclusions are calculated as responses to the compression which accounts for the magnitude of the compression.

As the volume fraction increases there are three scenarios that are likely to occur as shown in Figure 5.3. Cases II and III are more likely to occur in real world situations. Although case I is highly improbable, it is the scenario accepted in this study to keep equal aspect ratios of all the inclusion unlike in case II, and the x-location the same before and after “packing” unlike case III. Therefore, the code allows for overlap during “packing” as the volume fraction increases.

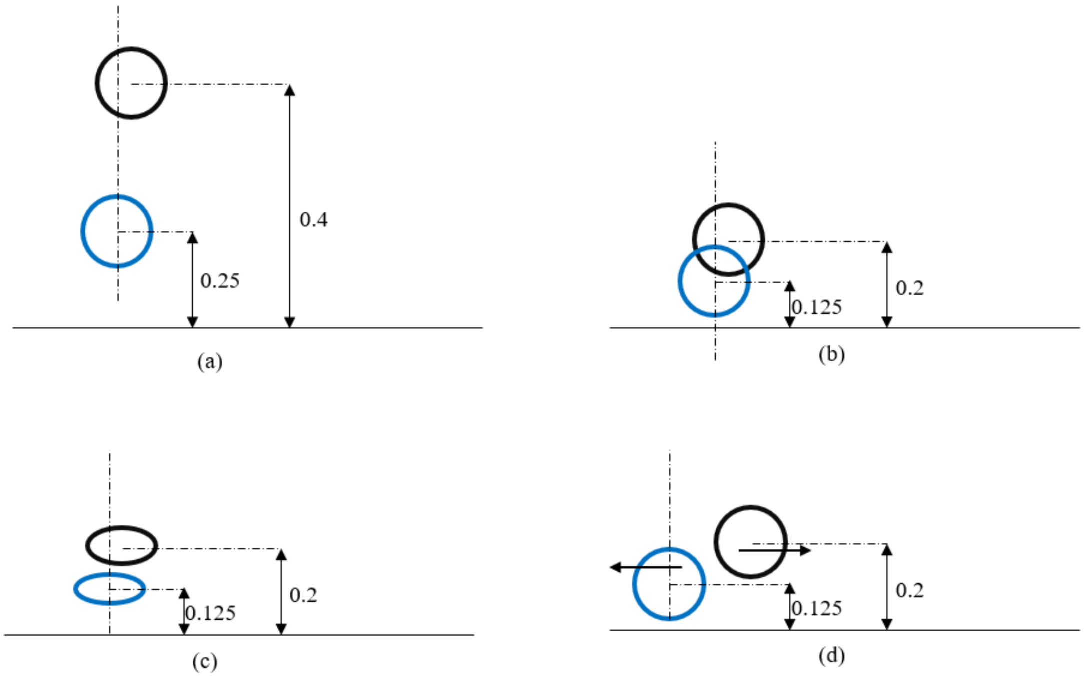

Figure 5.3: Possible scenarios of “packing” a) Original inclusion location; b) Case I; c) Case II; d) Case III

No units are shown in the figure above, because the dimensions are based on a normalized RVE cell of 1. Figure 5.4 shows the RVE of the composite with the randomly generated inclusions before and after “packing” with an aspect ratio of 1.

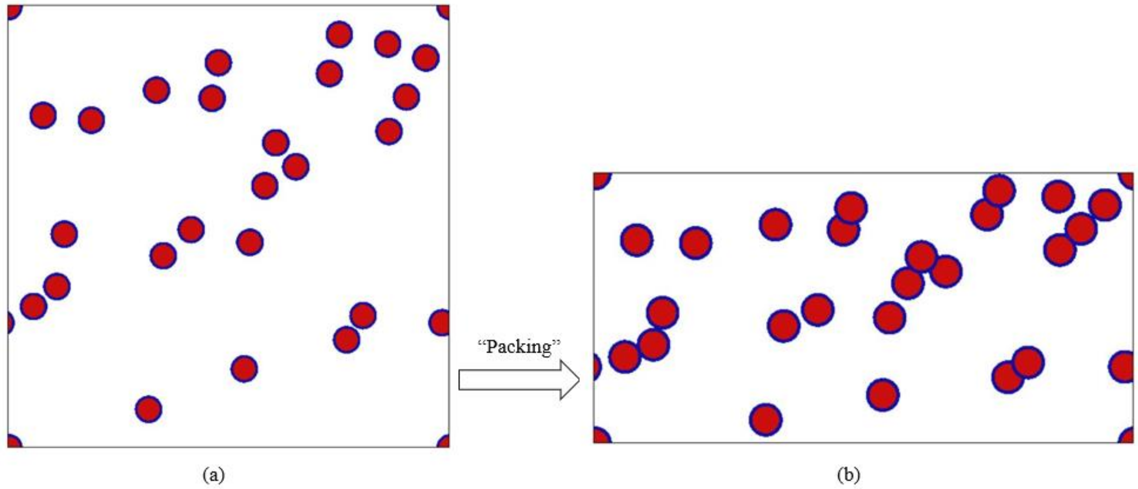

Figure 5.4: Representative element of C-C/SiC composite a) Before; b) After compression phase

Although the thicknesses of carbon fiber and silicon carbide differ, their aspect ratios are considered for all purposes equal. This is because in this study the silicon carbide is assumed to be wrapped around the carbon fibers (shown in red) and acts as the interface (shown in blue) between the reinforcements and the matrix of the composite, as shown in Figure 5.4. Where the radius of the silicon carbide is determined by the volume content.

5.2.1.3 FINITE ELEMENT MODEL, ANALYSIS AND POSTPROCESSING

This section describes the FE micromechanics method. The model setup using ABAQUS, the analysis, and postprocessing. The model is created using data (inclusion coordinates and angles of orientation) obtained from the RVE created using MATLAB, where the FE method is utilized to find the composite's elastic and thermal properties excluding density and specific heat. All micromechanics methods have advantages and disadvantages. The biggest disadvantages that occur is usually the improper use of method for a specific scenario. For example, the Voigt and Reuss method under predicts the material properties, because it does not consider the aspect ratio or orientation angles of the inclusions. Although the Voigt and Reuss method (ROM) is outdated and sometimes inaccurate, it has been shown to accurately predict the density and specific heat of a composite, because the density and specific heat are homogenous properties unaffected by direction. Hence, the rule of mixture shown in equations 5.2 & 5.3 are used to calculate the density and specific heat of the composite respectively.

$$\rho_c = \rho_f v_f + \rho_m v_m + \rho_i v_i \tag{5.2}$$

$$C_{pc} = \frac{1}{\rho_c}\Big(\big(v_f C_{pf} \rho_f\big) + \big(v_m C_{pm} \rho_m\big) + \big(v_i C_{pi} \rho_i\big)\Big) \tag{5.3}$$

The subscript *f*, *m*, and *i* represent fiber phase, matrix phase, and additional phases respectively. The model undergoes different loading conditions to determine the elastic and thermal properties of the composite.

The loading and boundary conditions determine what material property is to be calculated. For the elastic properties, the model has a periodic boundary condition (Figure 5.5) imposed on it, because the model itself has periodicity from the inclusions otherwise a Dirichlet boundary condition will be imposed.

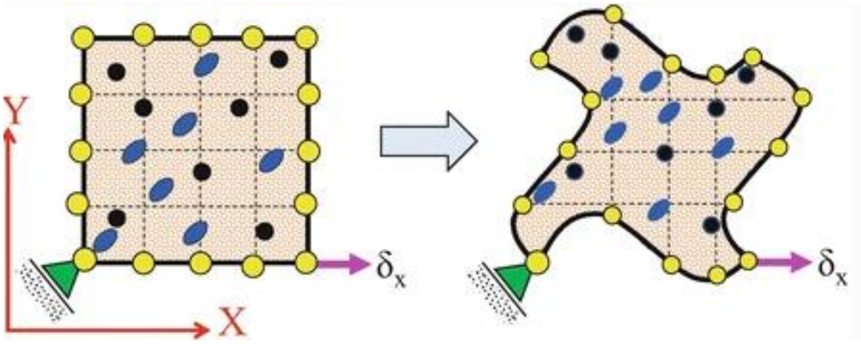

Figure 5.5: Periodic boundary condition visual representation

The periodic boundary condition is imposed on the edge nodes. A generalized form of the periodic boundary condition is shown in equation 5.4.

$$\xi^{ni} = \xi^{nj} \quad 5.4$$

Where, ξ represent any parameter such as displacement, temperature, etc., n represent node number, *i* represent an edge in the model, and *j* represent the edge opposite the *i* edge. The loading conditions for the elastic properties are imposed in the form of strain by calculating the total displacement of the model, because of the known relationship between strain and displacement shown equation 5.5.

$$\varepsilon = \frac{\Delta\Omega}{\Omega} \quad 5.5$$

Where, Ω represent parameters such as length, height, radius, etc.

A periodic boundary condition is imposed on the model for a thermo-mechanical simulation to find the thermo-mechanical properties (moduli, Poisson’s ratio, and coefficient of thermal expansion), while the Dirichlet boundary condition with adiabatic boundary (Figure 5.5) is imposed on the model in the thermal simulation for finding the thermal conductivity. Since the thermal loading does not result in a displacement, either a periodic or Dirichlet boundary condition will suffice, but other works published shows a Dirichlet boundary condition is common for thermal loadings.

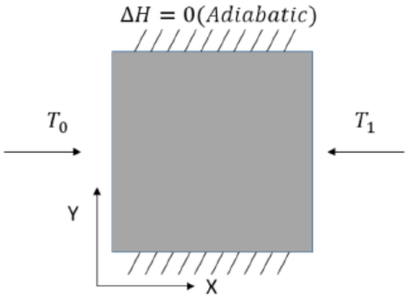

Figure 5.6: Dirichlet boundary condition for thermal loading

A failure criterion is imposed on the RVE. The composite is a three-phase composite; therefore, the failure criterion is limited to the least tensile strength. If the tensile stress reaches the prescribed tensile strength the material fractures. The governing failure criterion is shown in equation 5.6 which is based on the Von Mises stress.

$$f_i = F_i(\sigma) \tag{5.6}$$

Where, $F_{\mathrm{X}}(\sigma) = (\sigma_{11} - \sigma_{22})^2 + 2\sigma_{12}^2$ is Von Mises stress.

Two reference points were created as nodes in the model, one on the right side of the RVE (RP_1) and the other above the top boundary of the RVE (RP_2). The nodes on the right edge and the top edge of the RVE are linked to nodes RP_1 and RP_2 respectively using a multipoint constraint function.

After the tensile and thermal loading is done and the simulation is finished, the postprocessing is done on the obtained results. Postprocessing is done in the form of equations 5.7 - 5.12 to determine the material properties. Equation 5.7 is used to calculate the moduli (modulus of elasticity and shear modulus) of the composite material which is a rearranged Hooke's law, which uses the average stresses and strains generated during the tensile loading of the RVE. It can also be found graphically as the slope of a line parallel to the elastic region in a stress-strain curve with a 0.2% offset from the origin.

$$\xi_{ij} = \frac{\bar{\sigma}_{ij}}{\bar{\varepsilon}_{ij}} \qquad 5.7$$

Where, $\bar{\sigma}_{ij} = \frac{F}{A}$ is the average stress and $\bar{\varepsilon}_{ij} = \frac{u_{xRP1}}{L}$ is the average strain. While $F = \sum_{i=1}^{2}((x * Fx) + (y * Fy))_{RPi}$ is the sum of the reaction forces produced in tension, and $A = LH$ is the area of the RVE. The subscripts *i* & *j* above represent loading and response direction. In the case of uniaxial loading the parameter ξ represent modulus of elasticity, which in this case the subscripts *i* & *j* are the same and denote the loading direction, but when a shear loading is imposed the ξ represents the shear modulus and the *i* & *j* subscripts are not the same, for *i* represents the loading direction and *j* response direction. Although the RVE model is represented in a simplified 2D (plane-strain) space, the elastic properties in the third direction (z) are negligible compared to the "x" & "y" direction.

Equation 5.8 is the ratio of the strains experienced in both directions during loading (Poisson's ratio ν_{ij}), it also can be found graphically as the slope from the plot of the strain in the direction perpendicular to the loading direction vs. the strain parallel to the direction of the loading direction. The subscripts *i* and *j* are not the same, and *i* & *j* is either equal to 1 or 2 for a 2D model.

$$\nu_{ij} = \frac{-\bar{\varepsilon}_j}{\bar{\varepsilon}_i} \qquad 5.8$$

The negative sign means compression, therefore, the numerator in the above equation shows compression of the side perpendicular to the applied tensile load. The thermal conductivity is calculated using equation 5.9 which is a rearranged heat transfer equation. Also, the thermal conductivity can be found as the slope from a plot of heat flux vs. temperature gradient.

$$k_i = \frac{-q_i}{\Delta T_i} \qquad 5.9$$

Where q is the heat flux, ΔT_i is the temperature gradient, and subscript i is the thermal loading direction. For simplicity the temperature gradient (change in temperature) is 1°C. Therefore, the thermal conductivity will be equal to the negative value of an already negative heat flux. Equation 5.10 shows the generalized stress-strain equation which can be rearranged as shown in equation 5.12 to calculate the coefficient of thermal expansion (CTE).

$$\sigma_{ij} = C_{ijkl}\varepsilon_{kl}^{M} \qquad 5.10$$

Where, ε_{kl} is the elastic (mechanical) strain, but the total strain which is the sum of the mechanical and thermal strains

$$\varepsilon_{kl} = \varepsilon_{kl}^{M} + \varepsilon_{kl}^{T}$$

and the thermal strain can be written in terms of coefficient of thermal expansion and temperature gradient.

$$\varepsilon_{kl}^{T} = \alpha\Delta T\delta_{kl}$$

Where, δ_{kl} is the Kronecker-delta and the mechanical strain can be rewritten as the thermal strain subtracted from the total strain

$$\varepsilon_{kl}^{M} = \varepsilon_{kl} - \alpha\Delta T\delta_{kl}$$

Therefore, equation 5.10 can be rewritten as equation 5.11.

$$\sigma_{ij} = C_{ijkl}\left(\varepsilon_{kl} - \alpha_{ij}\Delta T\right) \tag{5.11}$$

Rearranging equation 5.11, to solve for coefficient of thermal expansion, with change in temperature (ΔT) of 1°C results in equation 5.12

$$\alpha_{ij} = I\varepsilon_{kl} - S_{ijkl}\sigma_{ij} \tag{5.12}$$

Where, I is the identity matrix and S is the compliance matrix which is the inverse of the stiffness matrix C.

When there is randomness in a system there tends to be errors associated with the randomness and this error is known as stochastic error. Walker [103] defined stochastic error as the possibility that the outcome is not expected, given that both the model and parameters are correct. In order to eliminate the presence of this error in the results, the material properties phase of this research is repeated ten (10) times. The average of each material property is calculated as the properties of the composite and used in the thermal-mechanical instabilities analysis.

5.2.2 THERMAL-MECHANICAL INSTABILITY

Thermomechanical instabilities can be described as the physical response of a system such as deformation due to a coupling effect of mechanical loads and thermal stresses. Two types of thermomechanical instability are studied in this paper namely thermal buckling and thermoelastic instability (TEI). They both require different loading conditions and the output expected from a thermal buckling analysis is the critical buckling temperature and critical sliding speed for a TEI analysis.

5.2.2.1 THERMAL BUCKLING

The most common buckling problem is a fully constrained beam under compressive load. Thermal buckling occurs in bodies not fully constrained but exposed to non-uniform thermal conditions. The eigenvalue buckling problem finds loads for which the determinant of the stiffness matrix is zero (singular matrix). The eigenvalue problem is stated in equation 5.13.

$$\left(K^{mn} + \lambda_i K_p^{mn}\right) X_i^n = 0 \tag{5.13}$$

Where, K^{mn} is the base state stiffness matrix with effects of a preload condition, λ_i represents the eigenvalues, K_p^{mn} represents stiffness matrix corresponding to perturbed loading condition, and X_i^n represents the eigenvectors (buckling mode). Therefore, the critical buckling load is $P + \lambda_i T$, where P is the preload, T is the maximum nodal temperature, and λ_i is the eigenvalue (usually the smallest) corresponding to the first eigenvector. For further information on buckling see ABAQUS [57]. An axisymmetric model is used in the thermal buckling analysis with dimensions shown in Table 5.2.

The thermal buckling analysis is conducted on a clutch disc and Figure 5.7 shows the axisymmetric model of a clutch disc. The non-uniform thermal load imposed on the clutch disc has a linear temperature profile increasing radially from the inner radius with a temperature of 315°C, to the outer radius with a temperature of 345°C. The boundary condition imposed on the model for the simulation is a $U_R^{IR} = 0$ (fixed) and $U_Z^{IR} = U_Z^{OR} \neq 0$ (free). Where *IR* & *OR* are inner radius and outer radius respectively.

Table 5.2: Dimension of single clutch disc for thermal buckling

	Clutch	Unit
Inner radius	44.5	mm
Outer radius	57	mm
Thickness	0.79	mm

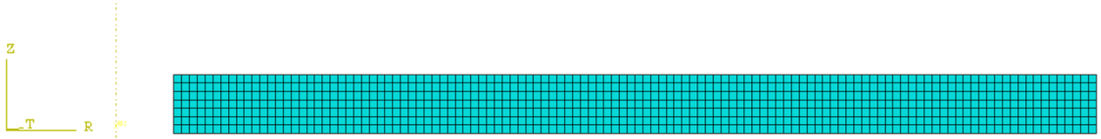

Figure 5.7: Axisymmetric model of a single disc clutch for thermal buckling simulation

5.2.2.2 THERMOELASTIC INSTABILITY

When two bodies slide against each other, frictional heat is generated and the resulting thermoelastic deformation alters the contact pressure distribution. This coupled thermal-mechanical process is susceptible to thermoelastic instability (TEI). Above a certain speed, the nominal pressure distribution becomes unstable, giving way to localization of load and heat generation and hence development of hot spots at the sliding interface. A MATLAB based software created by PhD students at the university of Michigan called Hotspotter [76] was utilized in find the critical sliding speed. It uses an eigenvalue method to find the exponential growth rate of eigenmodes for a given rotational speed. Therefore, the critical sliding speed is determined by searching for the lowest speed at which the growth rate is zero. It also uses an axisymmetric model as shown in Figure 5.8 of a clutch disc and friction disc, with the dimensions shown in Table 5.3.

Table 5.3: Dimension of an axisymmetric clutch and friction disc

	Clutch	Unit
Inner radius	44.5	mm
Outer radius	57	mm
	Thickness	
Friction material	0.673	mm
Steel disc	1.375	mm

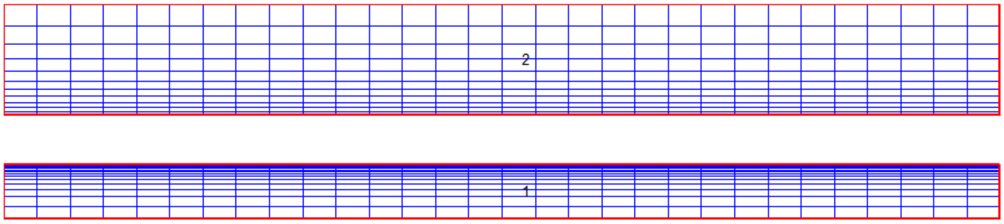

Figure 5.8: Axisymmetric model of a single disc clutch for TEI simulation

The layers shown in the above figure represent steel disc (layer 2) and friction disc (layer 1). Figure 5.8 shows a biased mesh, the mesh is biased toward the sliding interfaces to account for the large temperature gradients. This is done to accurately capture the temperature distribution by discretizing interface surface to small elements and eliminate any errors in numerical results.

5.3 RESULT

In numerical simulations, the mesh density plays a significant role as to the accuracy of the result and as such a mesh convergence study was conducted in calculating the material properties which is shown in Figure 5.9. The number of nodes represent the quality of mesh as coarse, medium, fine, and superfine. Below a certain number of nodes/elements the result does not converge and that is due to the connection between the inclusion and the matrix. This connection (interface) is so small, that it requires an even fine mesh quality to be able to transfer the stresses accurately between the inclusion and the matrix.

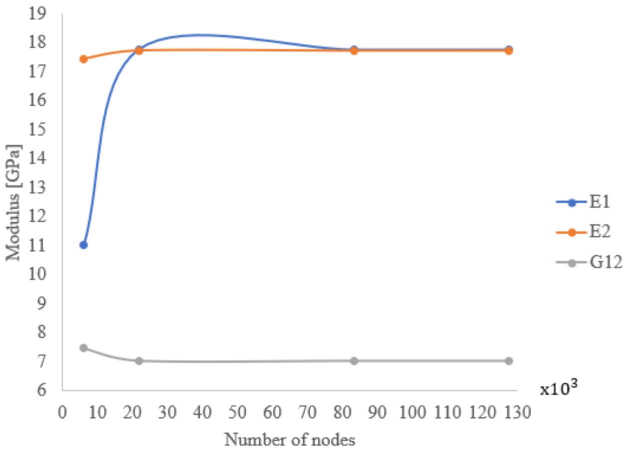

Figure 5.9: Convergence plot for the modulus material property

Figure 5.10 & Figure 5.11 show the stress plots of the RVE in uniaxial tensile loading and shear loading respectively. The deformation or elongation of the RVE in Figure 5.10 is very noticeable because a C-C/SiC composite is highly brittle that the strain to failure was found experimentally by Krenkel [35] to be 0.20% - 0.26%, and corroborated by this result.

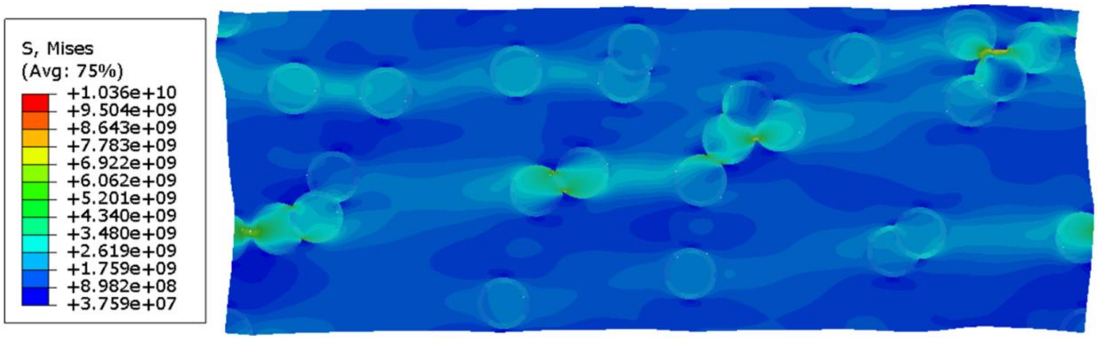

Figure 5.10: Stress contour plot of RVE under a uniaxial tensile load in the x-direction

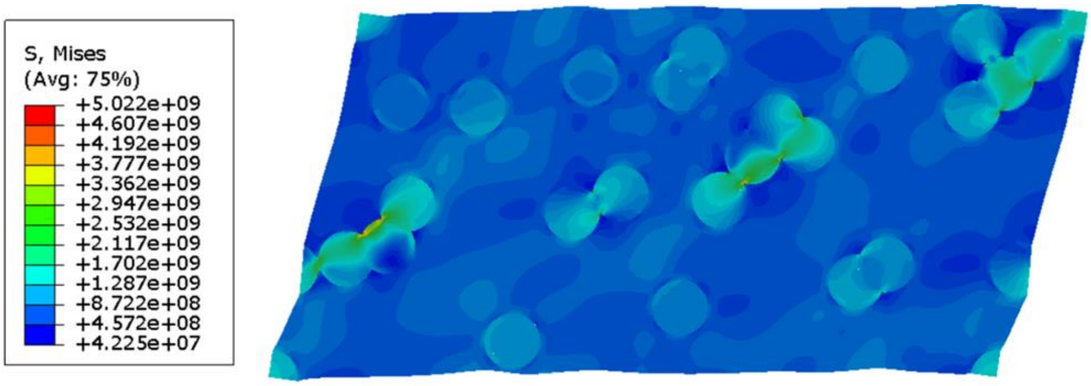

Figure 5.11: Stress contour plot of RVE under a shear load

Figure 5.12 - Figure 5.14 shows the variation of the material properties based on the change of carbon fiber content in the C-C/SiC composite.

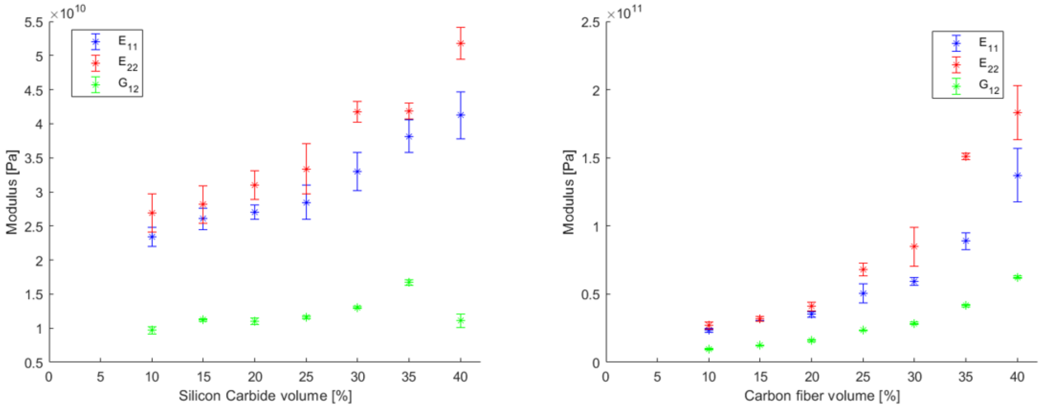

(a)

(b)

Figure 5.12: Effect of composite constituent content on modulus a) Silicon Carbide volume; b) Carbon fiber volume

An increase in either carbon fiber or silicon carbide in the composite increases the moduli (elastic & shear). An increase in carbon fiber has a greater response in the moduli property compared to a change in silicon carbide content. Carbon fiber has an inverse correlation to coefficient of thermal expansion (CTE), an increase in carbon fiber content decreases the composite's CTE, and vice versa for silicon carbide, whereas, an increase in silicon carbide content increases the CTE of the composite.

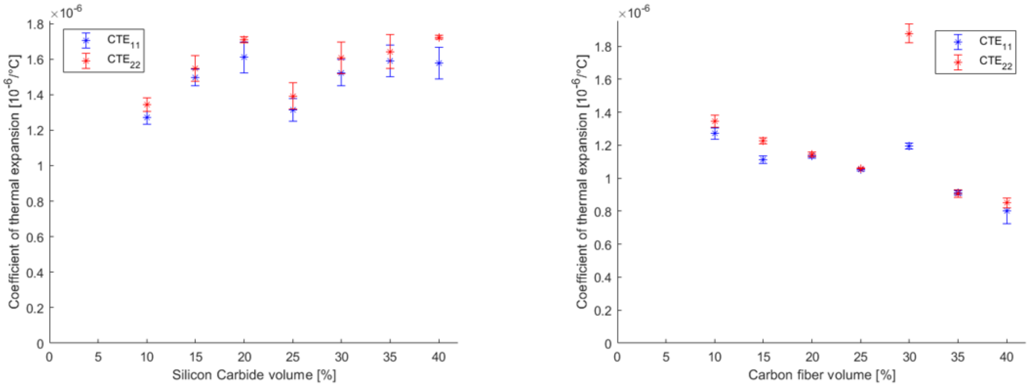

(a) (b)

Figure 5.13: Effect of composite constituent content on CTE a) Silicon Carbide volume; b) Carbon fiber volume

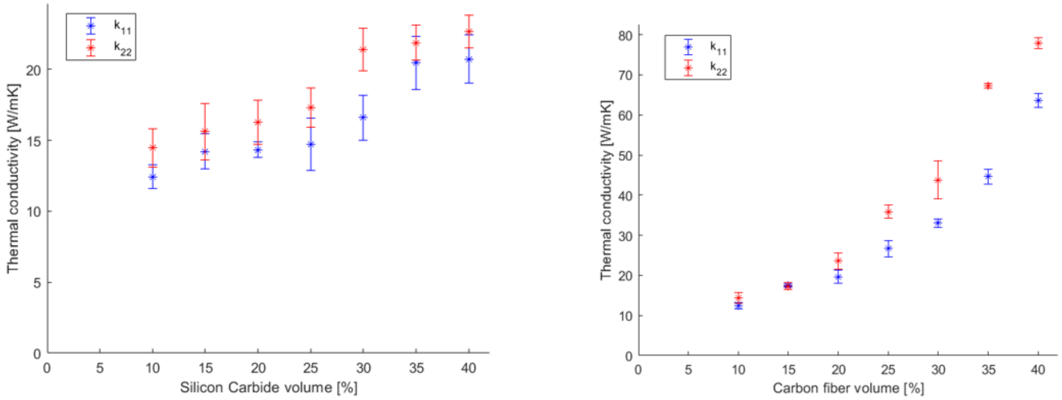

(a) (b)

Figure 5.14: Effect of composite constituent content on thermal conductivity a) Silicon Carbide volume; b) Carbon fiber volume

After the 10 trial runs, the error was calculated using the standard deviation and mean. The error was plotted on the same plot with Figure 5.12 - Figure 5.14 as error bars. The reason for the trial runs is to eliminate the stochastic error. Figure 5.12- Figure 5.14 proves the elimination of the error, because the average error was less than 3% for all the material properties.

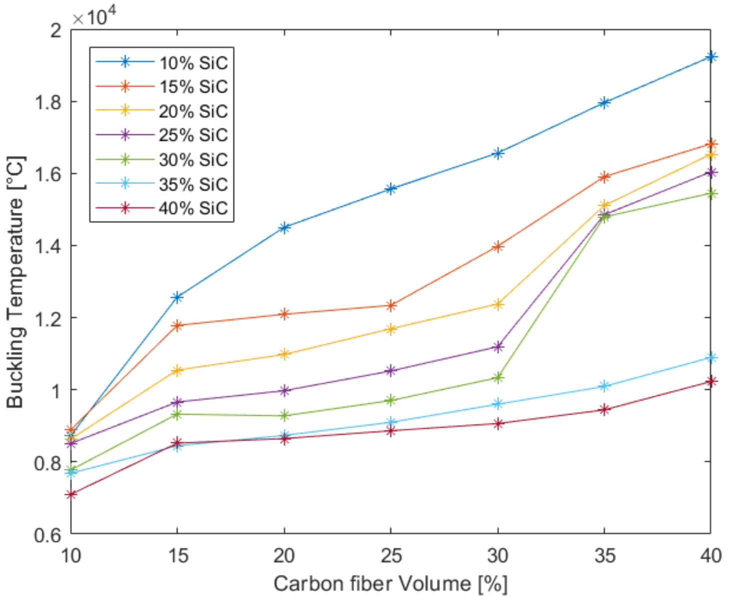

Figure 5.15: Effect of fiber volume on buckling temperature

The plot of buckling temperature in response to varying carbon fiber volume is shown in Figure 5.15. Increasing the carbon fiber volume increases the buckling temperature, also, an increase in silicon carbide volume in turn decreases the buckling temperature. Given the geometry, non-uniform temperature profile, and the result, it can be concluded that the clutch disc will buckle when the operating temperature exceeds approximately 7000 °C with a composite mixture of 10% carbon fiber and 40% silicon carbide. It should be noted this result is purely theoretical as the maximum temperature a clutch can achieve is significantly less than 7000 °C. The variation between the maximum and the minimum critical buckling temperature can be stipulated that the lowest silicon carbide content has a greater effect on the buckling temperature, which in this scenario is 10% silicon carbide (SiC).

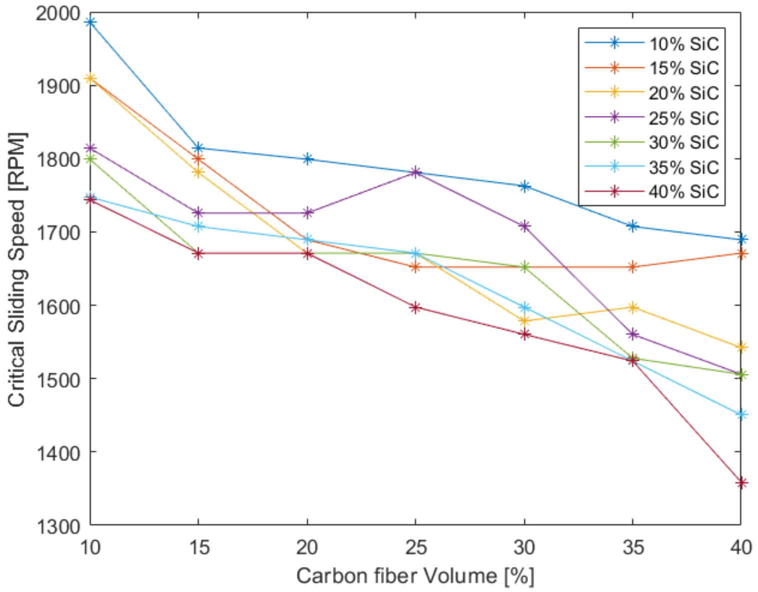

Figure 5.16: Effect of fiber volume on critical sliding speed for TEI

The plot of critical sliding speed in response to varying carbon fiber volume is shown in Figure 5.16. On average increasing the carbon fiber volume decreases the critical sliding speed, likewise, an increase in silicon carbide volume also decreases the critical sliding speed. Given the geometry, non-uniform temperature profile, and the result, it can be concluded that TEI in the clutch will occur at a low speed of approximately 1350 RPM and high-speed of 1990 RPM with a composite mixture of 10% carbon fiber and 10% silicon carbide; and 40% carbon fiber and 40% silicon carbide. It should be noted this result does not consider the time of contact and how many times the contact between the clutch disc and flywheel occurs. Therefore, for theoretical basis the clutch will show signs of hotspots. The variation between the maximum and the minimum critical buckling temperature can be stipulated that the lowest silicon carbide content has a greater effect on the buckling temperature, which in this scenario is 10% silicon carbide (SiC).

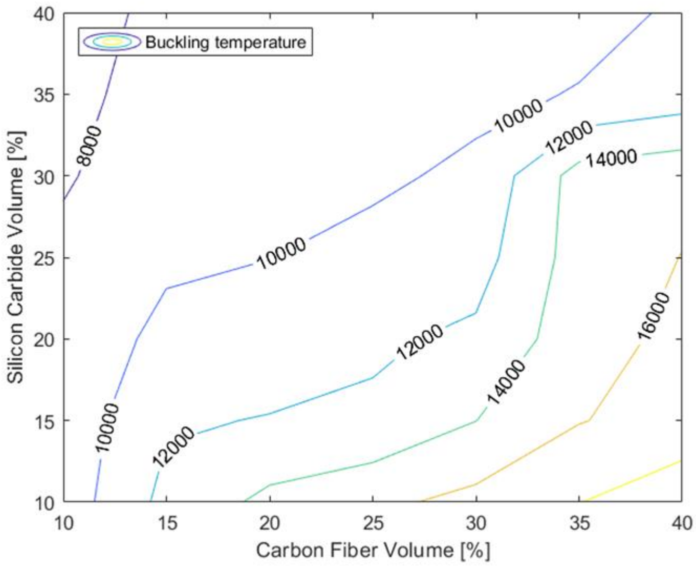

Figure 5.17: Contour plot of buckling temperature with varying volume ratios

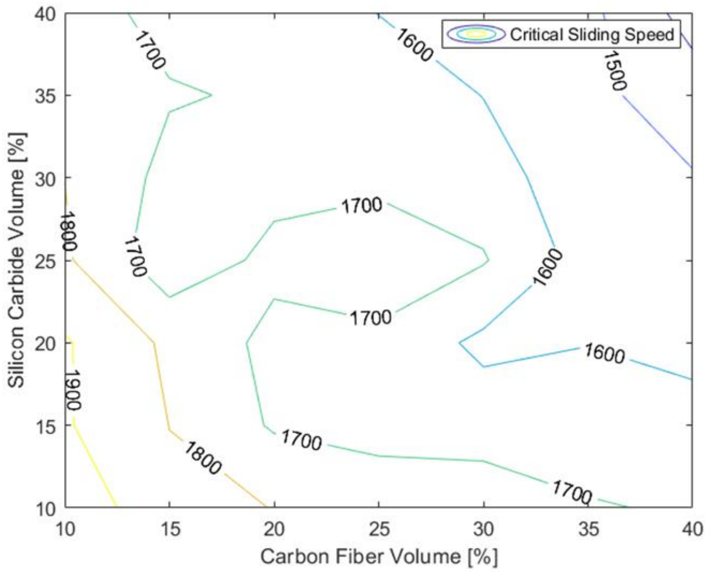

Figure 5.18: Contour plot of critical sliding speed with varying volume ratios

Figure 5.17 and Figure 5.18 are contour plots of buckling temperature and critical sliding speed respectively, showing varying carbon fiber volume and silicon carbide volume and how together they both affect the buckling temperature; a peak (maximum) value for buckling temperature occurs at a mixture with carbon fiber volume 40% and silicon carbide volume of 10%, while a carbon fiber volume of 10% and 10% silicon carbide volume produces a maximum critical sliding speed. A contour plot is relevant to clearly visualize the maximum and minimum value. Figure 5.19 shows a surface plot of normalized buckling temperature and critical sliding speed against varying carbon fiber and silicon carbide content in the composite material. The increasing surface plot represents the buckling temperature and the other critical sliding speed. The intersecting line created by the surfaces will determine the ideal composition of the composite that discourages the occurrence of TMI in a clutch disc. After inspection, the maximum point on the intersecting line corresponds to a 35% carbon fiber content and 20% silicon carbide content.

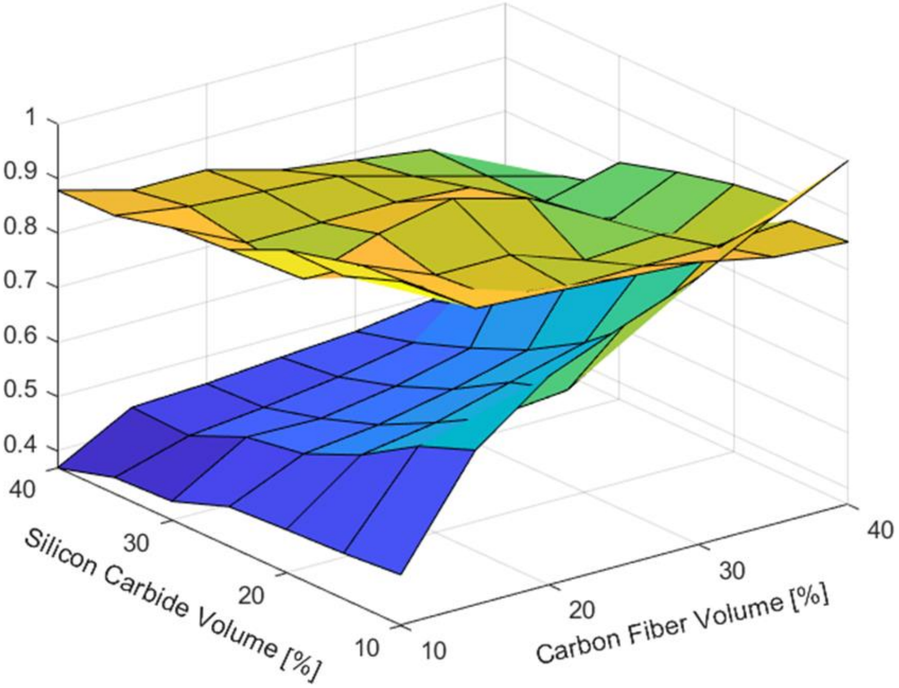

Figure 5.19: Normalized surface plot of critical sliding speed and buckling temperature.

5.4 CONCLUSION

The goal of this chapter is to find an ideal carbon fiber to silicon carbide ratio in the carbon-carbon silicon carbide composite that minimizes the occurrence of thermomechanical instability (TMI) in a clutch disc. The results show that an increase in carbon fiber increases the buckling temperature while an increase in silicon carbide decreases the buckling temperature. Ideally the highest carbon fiber content and lowest silicon carbide content will reduce the chances of thermal buckling occurrence in a clutch disc. The critical sliding speed that determines the presence of thermoelastic instability (TEI) shows a fluctuating trend with varying carbon fiber or silicon carbide content.

Therefore, after investigation of the results, it can be concluded that the ideal carbon content and silicon carbide to minimize the occurrence of TMI is 35% and 20% respectively. The composition does not produce the highest buckling temperature, nor does it result in highest critical sliding speed, but the combination produces both a high buckling temperature and critical sliding speed.

It can also be concluded that the increase in carbon fiber or silicon carbide increases the moduli of the composite, but the carbon fiber has a greater effect in the moduli of the composite. With this finding, an inference can be made that an increase in elastic modulus or shear modulus can increase the buckling temperature. Whereby the same increase in carbon fiber reduces the CTE of the composite. This decrease can be seen from the material properties of the individual constituents where the carbon fiber CTE is much lower than the CTE of the silicon carbide.

The increase of silicon carbide or carbon fiber increases the thermal conductivity of the composite, which can be inferred as the increase in thermal conductivity can increase thermal buckling. Because of the response of critical sliding speed, there is no direct correlation between an anisotropic property to thermoelastic instability.

CHAPTER VI

CONCLUSIONS AND FUTURE WORK

6.1 CONCLUSION

The dissertation research has been focused on studying the phenomenon of thermal-mechanical instability mostly experienced in automotive brakes and clutch disc. Quite a lot of theoretical work have been done on this topic and due to inaccessibility to experimental equipment, this research has focused on computational methods in studying thermal-mechanical instability. The research focused on two areas of thermal-mechanical instability thermal buckling and thermoelastic instability. The research primarily studied the events that cause these instabilities by looking into coupling of mechanical and thermal stress and friction material effect on thermal-mechanical instabilities.

Conclusions were made during this research. Under certain conditions instabilities can interact with one another to increase mechanical or elastic instability. The displacement alters the contact area and as such during sliding creates an uneven temperature gradient that can induce thermal buckling, and the buckling mode changes the rotational line which shifts the centrifugal forces at the outer radius and creates a moment which increases the instability and cause it to vibrate. Also, the occurrence of hotspots prevalent with thermoelastic instability can induce thermal buckling by lowering the critical buckling temperature closer to the operating temperature of the clutch, this has a higher chance of occurring in clutch disc, as the vice versa was seen for brakes.

Friction material plays a significant role in thermal-mechanical instability. Just altering the material by changing the coefficient of friction is seen to change the temperature and hence the internal stresses which can lead to thermal-mechanical instability. C-C/SiC composite was studied and its effect on thermal-mechanical instability. This composite was of interest due to its innate ability of being heat resistant, low wear rate, high heat dissipation among others and was chosen as the friction material of study for thermal-mechanical instabilities. In addition, C-C/SiC proved to be a suitable substitute to the more generally used and common metallic based friction material and eliminate potential environmental hazard. Alternatively, studying composite materials anisotropic properties and its effect on thermal-mechanical instability shows that not only does it reduce the chances of such instability occurring in brakes and clutches, but the arrangement of the reinforcement in the composite drastically changes the critical sliding speed and thermal buckling temperature. The properties in the direction perpendicular to the sliding direction of a unidirectional composite tend to have significant effect on the sliding speed. Coefficient of thermal expansion has little effect on TEI, and thermal conductivity has no effect on thermal buckling. Uniform temperature across the thickness mitigates the effect of coefficient of thermal expansion. Therefore, uniform temperature distribution across the thickness of a disc causes coefficient of thermal expansion to have negligible effect on thermal bucking. A ceramic matrix composite with randomly distributed inclusion proved to address the environmental pollution problem due to harmful metallic residue from a more traditional metallic based friction material.

To reduce the chances of thermal buckling from occurring the C-C/SiC composite is proposed to have a higher carbon fiber content compared to the SiC content, and to limit the introduction of TEI in a sliding frictional contact system like clutches the SiC content should be higher than the carbon fiber content. In the scenario of creating a brake or clutch friction material to limit damaged from thermal-mechanical instabilities, then a compromise should be considered. Because the same formulation that reduces the initiation of thermal buckling will be more susceptible to TEI and vice versa. This compromise to limit TMI in brakes and clutches is proposed to have carbon fiber volume of 35%, with aspect ratio of 1 and silicon carbide volume of 20%. The CMC alternative is lighter in weight than its traditional steel or grey cast iron and shows to have a higher critical buckling temperature and sliding speed.

6.2 FUTURE WORK

6.2.1 MACHINE LEARNING

Machine learning is an algorithm that learns and predicts certain responses based on a set of input data. For this study, machine learning will be utilized to predict the optimal composition of the composite material that minimizes the occurrence of thermal buckling and TEI based on the fiber volume fraction, aspect ratio, and constituents present. Machine learning is divided in supervised and unsupervised learning. The simplest and the most complex supervised learning machine learning algorithm is linear regression and artificial neural network (ANN) respectively. The regression method works well for problems with a single output, where the response plot results in single peak or valley, while deep neural network works well for equations with multiple outputs. The author hypothesize that ANN will be best suited with the data set collected from both thermal buckling and TEI simulations because of its nonlinearity. The architecture (structure) of the artificial neural network is shown in Figure 6.1, with an input layer, output layer and three (3) hidden layers.

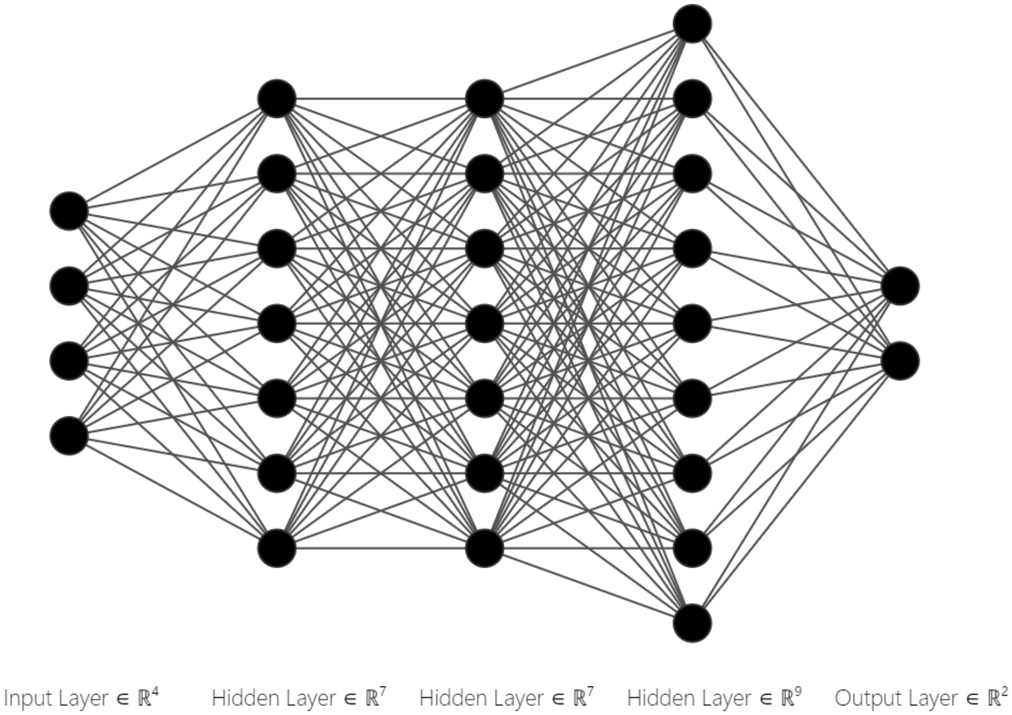

Figure 6.1: Neural network architecture for optimizing material properties.

The input layer has four (4) neurons (nodes), two (2) output nodes and a total of seventeen (17) nodes in the hidden layers. The nodes of the input layer each represent the constituents of the composite material. The output nodes represent the thermal buckling eigenvalue and the sliding speed. The number of hidden layers works in a similar fashion to the Taylor series, where the more terms you have in the Taylor series the more accurate the approximation is, and similarly, the more hidden layers, the more accurate the artificial neural network is. The output layer needs a “trigger” to activate, this “trigger” is known as the activation. Generally, for regression problems with a linear response output a Sigmoid function (equation 6.1) is used as the activation function,

$$\sigma(x) = \frac{1}{1 + e^{-x}} \tag{6.1}$$

shown graphically in Figure 6.2, where negative inputs end up close to zero (0) and positive inputs approaches one (1)

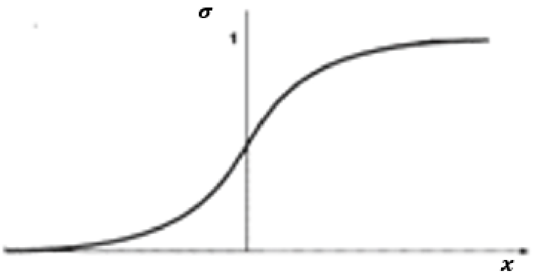

Figure 6.2: Graphical representation of Sigmoid function

In the case of a non-linear response output a more suitable activation is (rectified linear unit) ReLU (equation 6.2), graphically shown in Figure 6.3.

$$ReLU(x) = max\ (0, x) \tag{6.2}$$

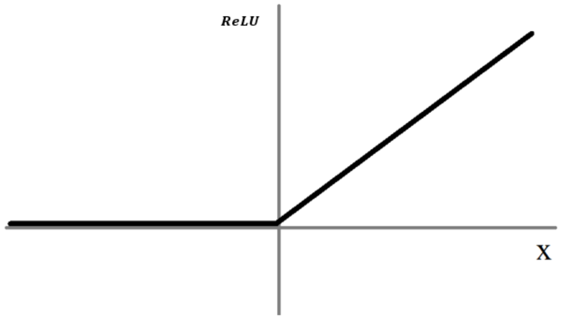

Figure 6.3: Graphical representation of ReLU

Optimizing a function is usually interpreted as minimizing the error between the predicted value and the actual value. This error is denoted as a “cost” function. The cost function is chosen based on the output response. In the case of this study where the multiple outputs have a non-linear relationship to the multiple inputs, the cost function is shown in equation 6.3.

$$J(\theta) = -\frac{1}{m}\left[\sum_{i=1}^{m}\sum_{k=1}^{K} y_k^i log\left(h_\theta(x^i)\right)_k\right] \qquad 6.3$$

Where *m, K, y, and* $h_\theta(x)$ is the number of test data, number of output nodes, actual output value, and predicted output value.

The purpose of this section is to use machine learning for optimization; therefore, an optimizer must be implemented in this algorithm. The chosen optimizer is the gradient descent. The gradient descent is chosen because it is versatile in optimizing all the data at once. The gradient descent (equation 6.4) uses the slope and a learning rate to optimize the weights to find the global minima.

$$y(\chi) = \frac{dy}{d\chi} = \nabla y \qquad 6.4$$

The weights are values multiplied with the nodal values in order to predict an output and is back propagated through the network to change the weight to predict another value and this is the iterative process. The output has a generalized form shown in equation 6.5.

$$y_i = w_1 x_{i1} + w_2 x_{i2} + \cdots + w_n x_{in} + w_0 \qquad 6.5$$

The step size of the gradient descent is proportional to the cost loss (error), which is multiplied by the negative derivative of the function. A mathematical representation is shown in the equation below.

$$-J(\theta)\ \nabla y \qquad 6.6$$

Where the negative sign controls the direction in which to step; if the step is negative, it implies the slope is decreasing and it should step in the positive direction by increasing the weight and vice versa if positive.

REFERENCES

(1) *Drum Brakes ∕ Brakes for Automobiles ∕ Product ∕ Products and Technologies | Akebono Brake Industry Co., Ltd.* https://www.akebono-brake.com/english/product_technology/product/automotive/drum/ (accessed 2023-11-23).

(2) *Difference Between Drum Brake vs Disc Brake - Explained in Detail*. https://www.spinny.com/blog/index.php/drum-brakes-vs-disc-brakes/ (accessed 2023-11-23).

(3) Niknafs, H.; Faridkhah, M.; Kazemi, C. Analytical Approach to Product Reliability Estimation Based on Life Test Data for an Automotive Clutch System. *Mech. Mech. Eng.* **2018**, *22* (4), 845–864. https://doi.org/10.2478/mme-2018-0065.

(4) Xue, J.; Ma, B.; Chen, M.; Zhang, Q.; Zheng, L. Experimental Investigation and Fault Diagnosis for Buckled Wet Clutch Based on Multi-Speed Hilbert Spectrum Entropy. *Entropy* **2021**, *23* (12), 1704. https://doi.org/10.3390/e23121704.

(5) Eslami, M. R.; Kiani, Y. Slender Beams, Thermal Buckling. In *Encyclopedia of Thermal Stresses*; Hetnarski, R. B., Ed.; Springer Netherlands: Dordrecht, 2014; pp 4427–4432. https://doi.org/10.1007/978-94-007-2739-7_514.

(6) Yang, Q.; Gai, F.; Song, L.; Yu, H.; Zhang, B. *Characteristics of a Brake Disc's Nonuniform Thermomechanical Responses to an Emergency Braking*; SAE Technical Paper 2019-01–2118; SAE International: Warrendale, PA, 2019. https://doi.org/10.4271/2019-01-2118.

(7) Ma, C. Thermal Buckling of Automotive Brake Discs. Ph.D., University of Michigan, United States -- Michigan. https://www.proquest.com/docview/305183107/abstract/79D2A157C0164832PQ/1 (accessed 2023-10-12).

(8) *Ansys Innovation Courses | Ansys Innovation Space*. ANSYS Innovation Courses. https://courses.ansys.com/ (accessed 2023-10-12).

(9) Chen, Z.; Yi, Y.-B.; Zhao, J. Fourier Finite Element Model for Prediction of Thermal Buckling in Disc Clutches and Brakes. *J. Therm. Stress.* **2016**, *39* (10), 1241–1251. https://doi.org/10.1080/01495739.2016.1215728.

(10) Belhocine, A.; Bouchetara, M. Investigation of Temperature and Thermal Stress in Ventilated Disc Brake Based on 3D Thermomechanical Coupling Model. *Ain Shams Eng. J.* **2013**, *4* (3), 475–483. https://doi.org/10.1016/j.asej.2012.08.005.

(11) Koranteng, K.; Shaahu, J.; Yi, Y.-B. *Transient Heat Transfer Simulation and Buckling Analysis of Disc Brakes in In-Wheel Motor-Driven Vehicles*; SAE Technical Paper 2020-01–1618; SAE International: Warrendale, PA, 2020. https://doi.org/10.4271/2020-01-1618.

(12) Li, M.; Ma, B.; Li, H.; Li, H.; Yu, L. Analysis of the Thermal Buckling of Annular Disks in Clutches under the Condition of Radial Temperature Gradient. *J. Therm. Stress.* **2017**, *40* (10), 1275–1284. https://doi.org/10.1080/01495739.2017.1334251.

(13) Yi, Y.-B.; Shaahu, J.-S.; Chen, Z. Instabilities Induced by Thermal-Mechanical Couplings in Clutch and Brake Discs; 2018; pp 2018-01–1894. https://doi.org/10.4271/2018-01-1894.

(14) Gong, Y.; Ge, W.; Yi, Y.-B. Finite Element Analysis of Thermal Buckling Characteristics of Automotive 430 Dry Clutch Pressure Plate. *Int. J. Veh. Des.* **2018**, *78* (1–4), 108–130. https://doi.org/10.1504/IJVD.2018.100098.

(15) *Brake Rotor: The Ultimate Guide - MZW Motor*. https://mzwmotor.com/brake-rotor-guide/ (accessed 2023-10-12).

(16) Shaahu, J.; Koranteng, K.; Yi, Y.-B. A Coupling Analysis of Thermal Buckling and Vibration in Disc Brakes; 2020; pp 2020-01–1606. https://doi.org/10.4271/2020-01-1606.

(17) Ling, H.; Meng, D.; Zhang, L.; Li, B. An Investigation of Initial Topography on Thermoelastic Behavior of Brake Disc under Thermal Load. *Mech. Syst. Signal Process.* **2023**, *200*, 110521. https://doi.org/10.1016/j.ymssp.2023.110521.

(18) Xiong, C.; Ma, B.; Li, H.; Zhang, F.; Wang, Y. Modeling and Analysis of Transient Temperature Field in Finite Thickness Plate under Symmetrically Located Moving Heat Sources. *Adv. Mech. Eng.* **2015**, *7* (11), 1687814015619554. https://doi.org/10.1177/1687814015619554.

(19) Audoly, B. Buckling and Post-Buckling of Plates. In *Encyclopedia of Continuum Mechanics*; Altenbach, H., Öchsner, A., Eds.; Springer: Berlin, Heidelberg, 2020; pp 222–237. https://doi.org/10.1007/978-3-662-55771-6_134.

(20) Chen, Z.; Yi, Y.-B.; Bao, K. Prediction of Thermally Induced Postbuckling of Clutch Disks Using the Finite Element Method. *Proc. Inst. Mech. Eng. Part J J. Eng. Tribol.* **2021**, *235* (2), 303–314. https://doi.org/10.1177/1350650120901978.

(21) Barber, J. R. Thermoelastic Instabilities in the Sliding of Conforming Solids. *Proc. R. Soc. Lond. Math. Phys. Sci.* **1969**, *312* (1510), 381–394. https://doi.org/10.1098/rspa.1969.0165.

(22) Yi, Y.; Barber, J. R.; Zagrodzki, P. Eigenvalue Solution of Thermoelastic Instability Problems Using Fourier Reduction. *Proc. R. Soc. Lond. Ser. Math. Phys. Eng. Sci.* **2000**, *456* (2003), 2799–2821. https://doi.org/10.1098/rspa.2000.0641.

(23) Dow, Th. A.; Burton, R. A. Thermoelastic Instability of Sliding Contact in the Absence of Wear. *Wear* **1972**, *19* (3), 315–328. https://doi.org/10.1016/0043-1648(72)90123-8.

(24) Barber, J. R. Frictionally Excited Thermoelastic Instability (TEI). In *Encyclopedia of Thermal Stresses*; Hetnarski, R. B., Ed.; Springer Netherlands: Dordrecht, 2014; pp 1825–1830. https://doi.org/10.1007/978-94-007-2739-7_145.

(25) Li, J.; Barber, J. R. Solution of Transient Thermoelastic Contact Problems by the Fast Speed Expansion Method. *Wear* **2008**, *265* (3), 402–410. https://doi.org/10.1016/j.wear.2007.11.010.

(26) Yi, Y.-B. Implementation of the Perturbation Method for Thermo Elastic Instability in Disk Clutches and Brakes. *J. Appl. Mech. Eng.* *3* (1), 1–3. https://doi.org/10.4172/2168-9873.1000e126.

(27) *Asbestos - Overview | Occupational Safety and Health Administration*. https://www.osha.gov/asbestos (accessed 2023-10-11).

(28) *Asbestos Exposure and Cancer Risk Fact Sheet - NCI*. https://www.cancer.gov/about-cancer/causes-prevention/risk/substances/asbestos/asbestos-fact-sheet (accessed 2023-10-11).

(29) Langhof, N.; Rabenstein, M.; Rosenlöcher, J.; Hackenschmidt, R.; Krenkel, W.; Rieg, F. Full-Ceramic Brake Systems for High Performance Friction Applications. *J. Eur. Ceram. Soc.* **2016**, *36* (15), 3823–3832. https://doi.org/10.1016/j.jeurceramsoc.2016.04.040.

(30) Zhao, E.; Ma, B.; Li, H. The Tribological Characteristics of Cu-Based Friction Pairs in a Wet Multidisk Clutch Under Nonuniform Contact. *J. Tribol.* **2017**, *140* (011401). https://doi.org/10.1115/1.4036720.

(31) Koranteng, K.; Shaahu, J.-S.; Chengnan, M.; Li, H.; Yi, Y.-B. The Performance of Cu-Based Friction Material in Dry Clutch Engagement. *Proc. Inst. Mech. Eng. Part J J. Eng. Tribol.* **2021**, *235* (6), 1114–1123. https://doi.org/10.1177/1350650120944281.

(32) Boz, M.; Kurt, A. The Effect of Al2O3 on the Friction Performance of Automotive Brake Friction Materials. *Tribol. Int.* **2007**, *40* (7), 1161–1169. https://doi.org/10.1016/j.triboint.2006.12.004.

(33) Ram Prabhu, T.; Varma, V. K.; Vedantam, S. Effect of Reinforcement Type, Size, and Volume Fraction on the Tribological Behavior of Fe Matrix Composites at High Sliding Speed Conditions. *Wear* **2014**, *309* (1), 247–255. https://doi.org/10.1016/j.wear.2013.10.001.

(34) Ram Prabhu, T.; Varma, V. K.; Vedantam, S. Effect of SiC Volume Fraction and Size on Dry Sliding Wear of Fe/SiC/Graphite Hybrid Composites for High Sliding Speed Applications. *Wear* **2014**, *309* (1), 1–10. https://doi.org/10.1016/j.wear.2013.10.006.

(35) Krenkel, W. Carbon Fibre Reinforced Silicon Carbide Composites (C/SiC, C/C-SiC). In *Handbook of Ceramic Composites*; Bansal, N. P., Ed.; Springer US, 2005; pp 117–148. https://doi.org/10.1007/0-387-23986-3_6.

(36) Krenkel, W.; Heidenreich, B.; Renz, R. C/C-SiC Composites for Advanced Friction Systems. *Adv. Eng. Mater.* **2002**, *4* (7), 427–436. https://doi.org/10.1002/1527-2648(20020717)4:7<427::AID-ADEM427>3.0.CO;2-C.

(37) Cheng, Y.; Xiao, Y.; Du, J.; Ji, D.; Shen, M. Size Effect of CrFe Particles on Tribological Behavior and Airborne Particle Emissions of Copper Metal Matrix Composites. *Tribol. Int.* **2023**, *183*, 108376. https://doi.org/10.1016/j.triboint.2023.108376.

(38) Seo, H.; Park, J.; Kim, Y. C.; Lee, J. J.; Jang, H. Effect of Disc Materials on Brake Emission during Moderate-Temperature Braking. *Tribol. Int.* **2021**, *163*, 107185. https://doi.org/10.1016/j.triboint.2021.107185.

(39) US EPA, O. *Aquatic Life Criteria - Copper*. https://www.epa.gov/wqc/aquatic-life-criteria-copper (accessed 2021-07-23).

(40) US EPA, O. *Copper-Free Brake Initiative*. https://www.epa.gov/npdes/copper-free-brake-initiative (accessed 2022-11-13).

(41) *Brake Friction Registration*. NSF. https://www.nsf.org/automotive-aerospace/brake-friction-registration (accessed 2023-10-11).

(42) Akıncıoğlu, G.; Öktem, H.; Uygur, I.; Akıncıoğlu, S. Determination of Friction-Wear Performance and Properties of Eco-Friendly Brake Pads Reinforced with

Hazelnut Shell and Boron Dusts. *Arab. J. Sci. Eng. Springer Sci. Bus. Media BV* **2018**, *43* (9), 4727–4737. https://doi.org/10.1007/s13369-018-3067-8.

(43) Milosevic, M.; Valášek, P.; Ruggiero, A. Tribology of Natural Fibers Composite Materials: An Overview. *Lubricants* **2020**, *8* (4), 42. https://doi.org/10.3390/lubricants8040042.

(44) Mann, G. S. ADVANTAGES AND DISADVANTAGES OF USING NATURAL FIBERS AS REINFORCEMENT MATERIALS. **2019**, *6* (3).

(45) Singaravelu, D. L.; Vijay, R.; Rahul, M. *Influence of Crab Shell on Tribological Characterization of Eco-Friendly Products Based Non Asbestos Brake Friction Materials*; SAE Technical Paper 2015-01–2676; SAE International: Warrendale, PA, 2015. https://doi.org/10.4271/2015-01-2676.

(46) Ammar, Z.; Ibrahim, H.; Adly, M.; Sarris, I.; Mehanny, S. Influence of Natural Fiber Content on the Frictional Material of Brake Pads—A Review. *J. Compos. Sci.* **2023**, *7* (2), 72. https://doi.org/10.3390/jcs7020072.

(47) Adekunle, A.; Okunlola, M.; Omoniyi, P.; Adeleke, A.; Ikubanni, P.; Popoola, T.; Ibrahim, K. DEVELOPMENT AND ANALYSIS OF FRICTION MATERIAL FOR ECO-FRIENDLY BRAKE PAD USING SEASHELL COMPOSITE. *Sci. Iran.* **2022**, *0* (0), 0–0. https://doi.org/10.24200/sci.2022.59835.6454.

(48) Krenkel, W.; Langhof, N. Ceramic Matrix Composites for High Performance Friction Applications. In *Proceedings of the IV Advanced Ceramics and Applications Conference*; Lee, B., Gadow, R., Mitic, V., Eds.; Atlantis Press: Paris, 2017; pp 13–28. https://doi.org/10.2991/978-94-6239-213-7_2.

(49) Geitner, F. K.; Bloch, H. P. Vibration Analysis. In *Machinery Failure Analysis and Troubleshooting*; Elsevier, 2012; pp 391–478. https://doi.org/10.1016/B978-0-12-386045-3.00005-2.

(50) Hajnayeb, A.; Baghi Abadi, M. K.; Hosseingholizadeh, A. An Experimental and Theoretical Study on the Vehicle Brake Judder. *SAE Tech. Pap.* https://doi.org/10.4271/2012-01-1820.

(51) Meyer, R. Brake Judder - Analysis of the Excitation and Transmission Mechanism within the Coupled System Brake, Chassis and Steering System. *SAE Tech. Pap.* https://doi.org/10.4271/2005-01-3916.

(52) Prokofʹevič, T. S.; Monroe, J. *Theory of Elastic Stability*; Dover, 2009.

(53) Stibich, P.; Wu, Y. H.; Zhang, W.; Guo, M.; Srinivasan, K.; Surapaneni, S. A Technique to Predict Thermal Buckling in Automotive Body Panels by Coupling Heat Transfer and Structural Analysis. *SAE Tech. Pap.* https://doi.org/10.4271/2014-01-0943.

(54) Audebert, N.; Barber, J. R.; Zagrodzki, P. BUCKLING OF AUTOMATIC TRANSMISSION CLUTCH PLATES DUE TO THERMOELASTIC/PLASTIC RESIDUAL STRESSES. *J. Therm. Stress.* **1998**, *21* (3), 309–326. https://doi.org/10.1080/01495739808956149.

(55) Ma, C. Thermal Buckling of Automotive Brake Discs.

(56) Palmer, E.; Mishra, R.; Fieldhouse, J. An Optimization Study of a Multiple-Row Pin-Vented Brake Disc to Promote Brake Cooling Using Computational Fluid

Dynamics. *Proc. Inst. Mech. Eng. Part J. Automob. Eng.* **2009**, *223* (7), 865–875. https://doi.org/10.1243/09544070JAUTO1053.

(57) *ABAQUS Analysis User's Manual (v6.6)*. https://classes.engineering.wustl.edu/2009/spring/mase5513/abaqus/docs/v6.6/books/usb/default.htm?startat=pt03ch06s02at02.html (accessed 2022-10-22).

(58) Maluf, O.; Angeloni, M.; Milan, M. T.; Spinelli, D.; Filho, W. W. B. DEVELOPMENT OF MATERIALS FOR AUTOMOTIVE DISC BRAKES.

(59) Belhocine, A.; Bouchetara, M. Thermal Analysis of a Solid Brake Disc. *Appl. Therm. Eng.* **2012**, *32*, 59–67. https://doi.org/10.1016/j.applthermaleng.2011.08.029.

(60) Daws, J. W.; Engineering, D.; Dr, W. M. Technical Considerations for Plus-Sizing. **2008**.

(61) Yi, Y.-B. Thermoelastic Instabilities in Automotive Disc Brakes and Clutches.

(62) Burton, R. A.; Nerlikar, V.; Kilaparti, S. R. THERMOPLASTIC INSTABILITY IN A SEAL-LIKE CONFIGURATION. 12.

(63) Lee, K.; Barber, J. R. Frictionally Excited Thermoelastic Instability in Automotive Disk Brakes. *J. Tribol.* **1993**, *115* (4), 607–614. https://doi.org/10.1115/1.2921683.

(64) Zagrodzki, P.; Lam, K. B.; Al Bahkali, E.; Barber, J. R. Nonlinear Transient Behavior of a Sliding System With Frictionally Excited Thermoelastic Instability. *J. Tribol.* **2001**, *123* (4), 699–708. https://doi.org/10.1115/1.1353180.

(65) Decuzzi, P.; Ciaverella, M.; Monno, G. Frictionally Excited Thermoelastic Instability in Multi-Disk Clutches and Brakes. *J. Tribol.* **2001**, *123* (4), 865–871. https://doi.org/10.1115/1.1352740.

(66) Yi, Y.; Barber, J. R.; Zagrodzki, P. Eigenvalue Solution of Thermoelastic Instability Problems Using Fourier Reduction. *Proc. R. Soc. Lond. Ser. Math. Phys. Eng. Sci.* **2000**, *456* (2003), 2799–2821. https://doi.org/10.1098/rspa.2000.0641.

(67) Jang, Y. H.; Ahn, S. Frictionally-Excited Thermoelastic Instability in Functionally Graded Material. *Wear* **2007**, *262* (9–10), 1102–1112. https://doi.org/10.1016/j.wear.2006.11.011.

(68) Zhao, J.; Yi, Y.-B.; Li, H. Effects of Frictional Material Properties on Thermoelastic Instability Deformation Modes. *Proc. Inst. Mech. Eng. Part J J. Eng. Tribol.* **2015**, *229* (10), 1239–1246. https://doi.org/10.1177/1350650115576783.

(69) Zagrodzki, P. Numerical Analysis of Temperature Fields and Thermal Stresses in the Friction Discs of a Multidisc Wet Clutch. *Wear* **1985**, *101* (3), 255–271. https://doi.org/10.1016/0043-1648(85)90080-8.

(70) Tauchert, T. R. Thermally Induced Flexure, Buckling, and Vibration of Plates. *Appl. Mech. Rev.* **1991**, *44* (8), 347–360. https://doi.org/10.1115/1.3119508.

(71) Najafizadeh, M. M.; Heydari, H. R. Thermal Buckling of Functionally Graded Circular Plates Based on Higher Order Shear Deformation Plate Theory. *Eur. J. Mech. - ASolids* **2004**, *23* (6), 1085–1100. https://doi.org/10.1016/j.euromechsol.2004.08.004.

(72) Ghiasian, S. E.; Kiani, Y.; Sadighi, M.; Eslami, M. R. Thermal Buckling of Shear Deformable Temperature Dependent Circular/Annular FGM Plates. *Int. J. Mech. Sci.* **2014**, *81*, 137–148. https://doi.org/10.1016/j.ijmecsci.2014.02.007.

(73) Sepahi, O.; Forouzan, M. R.; Malekzadeh, P. Thermal Buckling and Postbuckling Analysis of Functionally Graded Annular Plates with Temperature-Dependent Material Properties. *Mater. Des.* **2011**, *32* (7), 4030–4041. https://doi.org/10.1016/j.matdes.2011.03.063.

(74) Zhao, J.; Chen, Z.; Yang, H.; Yi, Y.-B. Finite Element Analysis of Thermal Buckling in Automotive Clutch Plates. *J. Therm. Stress.* **2016**, *39* (1), 77–89. https://doi.org/10.1080/01495739.2015.1123590.

(75) Cenbo, X.; Biao, M.; Heyan, L.; Fenglian, Z.; Da, W. Experimental Study and Thermal Analysis on the Buckling of Friction Components in Multi-Disc Clutch. *J. Therm. Stress.* **2015**, *38* (11), 1323–1343. https://doi.org/10.1080/01495739.2015.1073524.

(76) Hotspotter.

(77) Sriwiboon, M.; Tiempan, N.; Kaewlob, K. Non-Asbestos Organic (NAO) Disc Pad Wear Behavior: Divergence of Thickness Loss and Weight Loss. *SAE Tech. Pap.* **2018**. https://doi.org/10.4271/2018-01-1866.

(78) Sanguineti, A.; Samela, A.; Rampinelli, F.; Bottalico, L. Cementitious-Based Brake Pads Technology: Performance, Low Energy Consumption, Emission Drop. *SAE Tech. Pap.* **2018**. https://doi.org/10.4271/2018-01-1867.

(79) Solomon, D. G.; Berham, M. N. Characterization of Friction Material Formulations for Brake Pads. *Proc. World Congr. Eng.* **2007**, *2*.

(80) Jiaxin Zhao; Biao Ma; Heyan Li. Investigation of Thermoelastic Instabilities of Wet Clutches. In *2013 IEEE International Symposium on Assembly and Manufacturing (ISAM)*; IEEE: Xi’an, China, 2013; pp 69–72. https://doi.org/10.1109/ISAM.2013.6643490.

(81) Yi, Y.-B. Perturbation Methods in Thermoelastic Instability (TEI) with Finite Element Implementation. In *Encyclopedia of Thermal Stresses*; Hetnarski, R. B., Ed.; Springer Netherlands: Dordrecht, 2014; pp 3635–3641. https://doi.org/10.1007/978-94-007-2739-7_154.

(82) Hockin H. K. Xu; Claudia P. Ostertag; Linda M. Braun; Isabel K. Lloyd. Effects of Fiber Volume Fraction on Mechanical Properties of SiC-Fiber/Si3N4-Matrix Composites. *J. Am. Ceram. Soc.* **1994**, *77* (7), 1897–1900. https://doi.org/10.1111/j.1151-2916.1994.tb07068.x.

(83) Ciprian, L.; Radu, P.; Ioana, E. The Effects of Fibre Volume Fraction on a Glass-Epoxy Composite Material. *INCAS Bull.* **2015**, *7* (3), 113–119. https://doi.org/10.13111/2066-8201.2015.7.3.10.

(84) Oladele, I. O.; Agbeboh, N. I.; Omokafe, S. M.; Ibrahim, O. I. Effects of Fiber Fraction on the Mechanical and Abrasion Properties of Treated Cow Hair Fiber Reinforced Polyester Composites. *Tribol. Ind.* **2018**, *40* (2), 254–262. https://doi.org/10.24874/ti.2018.40.02.09.

(85) Zuo, J.-L.; Zhang, H.-B.; Li, J.-H.; Xiong, X. Effect of Fiber Volume Fraction on Friction and Wear Properties of C/C Composites. **2005**, *36*, 555–559.

(86) Aboudi, J.; Arnold, S. M.; Bednarcyk, B. A. Fundamentals of the Mechanics of Multiphase Materials. In *Micromechanics of Composite Materials: A Generalizied*

Multiscale Analysis Approach; Elsevier, 2013; pp 87–145. https://doi.org/10.1016/B978-0-12-397035-0.00003-3.

(87) Aboudi, J.; Arnold, S. M.; Bednarcyk, B. A. Constituent Material Modeling. In *Micromechanics of Composite Materials: A Generalizied Multiscale Analysis Approach*; Elsevier, 2013; pp 26–33. https://doi.org/10.1016/B978-0-12-397035-0.00002-1.

(88) Pardini, L. C.; Gregori, M. L. Modeling Elastic and Thermal Properties of 2.5D Carbon Fiber C/SiC Hybrid Matrix Composites by Homogenization Method. *J. Aerosp. Technol. Manag.* **2010**, *2* (2), 183–194. https://doi.org/10.5028/jatm.2010.02026510.

(89) Belhocine, A.; Bouchetara, M. Thermomechanical Coupling Analysis of a Disc Brake Rotor. *J. Fail. Anal. Prev.* **2012**, *12* (6), 697–706. https://doi.org/10.1007/s11668-012-9616-7.

(90) Abdullah, O. I.; Schlattmann, J. Thermal Behavior of Friction Clutch Disc Based on Uniform Pressure and Uniform Wear Assumptions. *Friction* **2016**, *4* (3), 228–237. https://doi.org/10.1007/s40544-016-0120-z.

(91) Faidh-Allah, M. H. The Temperature Distribution in Friction Clutch Disc under Successive Engagements. *Tribol. Ind.* **2018**, *40* (1), 92–99. https://doi.org/10.24874/ti.2018.40.01.08.

(92) CES EduPack, 2009.

(93) Hartsock, D. L.; Fash, J. W. Effect of Pad/Caliper Stiffness, Pad Thickness, and Pad Length on Thermoelastic Instability in Disk Brakes. *J. Tribol.* **2000**, *122* (3), 511–518. https://doi.org/10.1115/1.555394.

(94) Mao, J.-J.; Ke, L.-L.; Yang, J.; Kitipornchai, S.; Wang, Y.-S. Thermoelastic Instability of Functionally Graded Materials with Interaction of Frictional Heat and Contact Resistance. *Mech. Based Des. Struct. Mach.* **2018**, *46* (2), 139–156. https://doi.org/10.1080/15397734.2017.1319283.

(95) Qiu, J. Computational Modeling of Percolation Conduction and Diffusion of Heterogeneous Materials. 131.

(96) Tawerghi, E.; Yi, Y.-B. A Computational Study on the Effective Properties of Heterogeneous Random Media Containing Particulate Inclusions. *J. Phys. Appl. Phys.* **2009**, *42* (17), 175409. https://doi.org/10.1088/0022-3727/42/17/175409.

(97) Zhao, D. Computational Study of the Effect of Interparticle Contact in Conductive Properties of Random Particulate Systems. 94.

(98) Yi, Y. B. The Role of Interparticle Contact in Conductive Properties of Random Particulate Materials. *Acta Mater.* **2008**, *56* (12), 2810–2818. https://doi.org/10.1016/j.actamat.2008.02.018.

(99) Markworth, A. J.; Saunders, J. H. A Model of Structure Optimization for a Functionally Graded Material. *Mater. Lett.* **1995**, *22* (1–2), 103–107. https://doi.org/10.1016/0167-577X(94)00238-X.

(100) Ootao, Y.; Kawamura, R.; Tanigawa, Y.; Imamura, R. Optimization of Material Composition of Nonhomogeneous Hollow Sphere for Thermal Stress Relaxation Making Use of Neural Network. *Comput. Methods Appl. Mech. Eng.* **1999**, *180* (1), 185–201. https://doi.org/10.1016/S0045-7825(99)00055-9.

(101) Na, K.-S.; Kim, J.-H. Volume Fraction Optimization of Functionally Graded Composite Panels for Stress Reduction and Critical Temperature. *Finite Elem. Anal. Des.* **2009**, *45* (11), 845–851. https://doi.org/10.1016/j.finel.2009.06.023.
(102) Kevlar® Aramid Fiber Technical Guide. 24.
(103) Walker, S. 1996 GENERAL INSURANCE CONVENTION 2 · 5 OCTOBER 1996. 9.